
UNIVERSITY OF BIRMINGHAM

# CHARACTERISATION OF CORONARY ARTERIES:

# MECHANICAL TESTING AND THREE-DIMENSIONAL IMAGING

by

**HANNA ELISABETH BURTON**

A thesis submitted to the

University of Birmingham for the degree of

DOCTOR OF PHILOSOPHY

Department of Mechanical Engineering

School of Engineering

University of Birmingham

September 2017

# ABSTRACT

Coronary artery disease is the leading cause of death in the UK. The studies in this thesis aim to influence the design of new biomaterials and medical devices used to treat coronary artery disease through the characterisation of left anterior descending (LAD) coronary arteries.

The mechanical properties of arteries were quantified using dynamic mechanical analysis, at physiological relevant frequencies. The surface roughness of porcine LAD coronary arteries was quantitatively measured using optical, scanning electron (SEM) and atomic force microscopy at various magnifications to assess its multi-scale characteristics. Further, the effect of damage to surface roughness of biological tissue was investigated due to mechanical overloading and chemical processing, with a correction factor presented for the changes to surface roughness due to processing techniques associated with SEM.

This thesis found LAD arteries to be viscoelastic, with a frequency-dependent storage moduli that does not vary along the length of the artery. Processing of tissue caused a significant increase in surface roughness, which must be considered for different microscopy techniques. The dehydration process had a greater effect on surface roughness than mechanical damage. The mechanical and surface roughness properties presented in this thesis can be specified for biomaterials to replicate natural, healthy coronary arteries.

Dedicated to my Grandparents

# ACKNOWLEDGMENTS

To Dr Daniel Espino, thank you for your supervision. Without your support, this work would not have been possible. I am extremely grateful for your patience and guidance.

To Dr Sophie Cox and Professor Liam Grover, thank you for the opportunities you gave me that have helped me to pursue a career in my research.

To the mechanical engineering technical staff, whose knowledge and hard work keeps the Department of Mechanical Engineering running: Carl Hingley (BEM), Peter Thornton, Lee Gauntlett, Jack Garrod, Adam Sheward and Becky Charles.

To the Biomedical Engineering Group, especially Dr Dave and the Irish one for equal amounts of support and coffee. And to the TRAILab for welcoming me.

To the Engineering and Physical Sciences Research Council scholarship for funding this work [M114612B], and to the Institution of Mechanical Engineers for my travel grant to the 22nd Congress of the European Society of Biomechanics in Lyon.

To my family. Mum and Dad, thank you for your unconditional love and support. Ashley, only you can ever understand our mad family – thank you for being the normal one I get to call my brother. My grandparents, thank you for being my biggest fans.

To my husband, Christian Burton, thank you for showing me how to dream big.

# CONTENTS

# LIST OF FIGURES

# LIST OF TABLES

# ACRONYMS

2D – two-dimensional

3D – three-dimensional

AFM – atomic force microscopy

ANOVA – analysis of variance

BMS – bare metal stent

BSE – back scatter electron

CABG – coronary artery bypass grafting

CFD – computational fluid dynamics

CHD – coronary heart disease

CVD – cardiovascular disease

DES – drug eluting stent

DMA – dynamic mechanical analysis

ESEM – environmental scanning electron microscopy

HMDS – hexamethyldisilasane

LAD – left anterior descending

LCX – left circumflex

MANOVA – multivariance analysis of variance

NHS – national health service

PBS – phosphate buffer saline

PCI – percutaneous coronary intervention

SEM – scanning electron microscopy

SD – standard deviation

# 1 INTRODUCTION

Cardiovascular disease (CVD) is the leading cause of mortality worldwide (World Health Organisation, 2017). CVD healthcare costs in the UK were £11.3 billion in 2014 (Centre for Economic and Business Research, 2014). In the UK, coronary heart disease (CHD) was the biggest single cause of death, resulting in over 69,000 deaths in 2015 (British Heart Foundation, 2017). In the USA, CHD was the underlying cause of death in 1 out of every 7 deaths in 2011, with direct and indirect costs associated with heart disease estimated at $204.4 billion in 2010 (Mozaffarian et al., 2015). Treatment of CHD is not always successful, and complications such as restenosis or thrombosis can occur.

The aim of this thesis was to characterise properties of coronary arteries that would aid in the development of medical treatments for coronary artery disease. This would be achieved by:

- Quantifying the surface roughness of coronary arteries
- Acquiring the mechanical properties of coronary arteries
- Assessing the effect of damage on surface roughness of coronary arteries

This thesis investigates the mechanical and surface roughness properties of coronary arteries, specifically along the left anterior descending (LAD) artery. The LAD artery supplies the left hand side of the heart, responsible for pumping blood around the body. The LAD artery is commonly referred to as the 'widow maker', as an occlusion at the beginning of the LAD artery will often result in death (Ahmed, 2015).

Characterisation and quantification of these mechanical and surface roughness properties can be combined to model disease of coronary arteries through computational simulation. The measurements can provide a standard for bio-inspired materials to adhere to, ensuring physiological similarity to native tissue. These properties are important for the development of clinical treatments through novel designs of vascular implants (e.g. stents and grafts) and tissue engineered replacements (Holzapfel et al., 2005). In the design of blood pumps, for example, surface roughness affects the coagulation properties of blood, which can increase the possibility for blood clot formation (Linneweber et al., 2007). Currently, there are no studies that provide quantitative data of surface roughness for coronary arteries, and the dynamic viscoelastic mechanical properties of coronary arteries have not been investigated.

A porcine model is used in this thesis due to the physiological similarity to the human heart anatomy (Ozolanta et al., 1998; Van Andel, Pistecky, and Borst, 2003). No animals were specifically sacrificed for this study; all hearts were supplied by Fresh Tissue Supplies (Horsham, UK). Ethical approval was granted for this study by the University of Birmingham *Research Support Group*, [ERN_15-0032].

Chapter 2 presents background research pertinent to this thesis, including an introduction to the cardiovascular system and CHD. Surgical interventions are discussed, including percutaneous coronary intervention and coronary artery bypass grafting. Further, mechanical properties of materials are discussed, and surface roughness characterisation.

Chapter 3 discusses the process of imaging LAD coronary arteries to enable quantification of surface roughness. To enable imaging, specimens are dehydrated using a

chemical processing protocol, for which a correction factor is calculated. General methods relevant to further chapters within this thesis are also presented, including dissection, tissue processing and optical imaging. The work presented in this chapter is published as two papers. The surface roughness measurement technique of LAD coronary artery was accompanied by mechanical testing presented in chapter 7 as one paper, which was published in the journal *Cardiovascular Engineering and Technology*, entitled 'Dynamic viscoelasticity and surface properties of porcine left anterior descending coronary arteries'; 2017, volume 8, issue 1, pages 41-56. This work was also presented at the 22nd Congress of the European Society of Biomechanics – Lyon, 2016, thanks to a travel grant provided by the Institution of Mechanical Engineers. The effect of chemical processing on LAD coronary artery was published as a separate paper in the journal *Micron*, entitled 'Effects of freezing, fixation and dehydration on surface roughness properties of porcine left anterior descending coronary arteries'; 2017, volume 101, pages 78-86.

Chapter 4 presents a multiscale analysis of the surface roughness of LAD coronary arteries, using optical, scanning electron and atomic force microscopy. Surface roughness is analysed at a micro- and nano-scale, and a comparison of both microscopy technique and magnification is considered.

Chapter 5 studies the dynamic viscoelasticity of LAD coronary arteries. This work complemented the surface roughness results in chapter 3 in characterisation of coronary arteries, and was published alongside these results in the 'Dynamic viscoelasticity and surface properties of porcine left anterior descending coronary arteries' paper. Additionally,

to replicate disease in coronary arteries and understand its effect the characteristics of arteries, mechanical damage was inflicted on specimens and surface roughness measured.

Chapter 6 provides a general discussion and conclusion to this thesis, and discusses how the findings presented could be applied to future work.

# 2 BACKGROUND

## 2.1 OVERVIEW

This chapter describes the background areas surrounding this thesis. The main topics discussed include the cardiovascular system (section 2.2), surface roughness (section 2.3) and mechanical properties (section 2.4). The aim of this chapter is to guide the reader through the research themes, and to help understand how the findings of this thesis cumulate. Briefly, disease within the cardiovascular system is explained in section 2.2.5, with medical interventions to cure these diseases highlighted (section 2.2.6).

## 2.2 CARDIOVASCULAR SYSTEM

### 2.2.1 Blood

The role of the cardiovascular system is to transport blood around the body. An adult male human body, on average, contains 5 litres of blood (Starr and Taggart, 1989). Blood is made up of red blood cells, white blood cells and platelets (figure 2. 1). Red blood cells (erythrocytes) deliver oxygen to tissues within the body (Turgeon, 2005), whereas the principal role of white blood cells (leukocytes) is to fight disease in the body (Maton et al., 1997). Platelets (thrombocytes) contribute to the coagulation properties of blood, clotting blood vessels when there is injury (Laki, 1972). The blood plasma, which suspends these cells, transports nutrients to tissue in the body, and transports waste away (University of Rochester Medical Center, 2017).

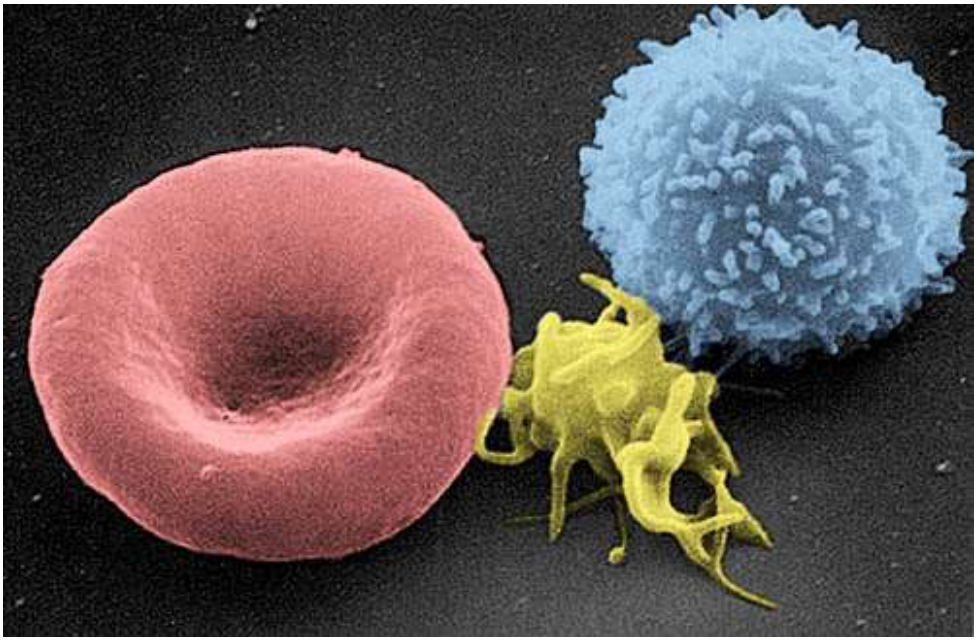

*Figure 2. 1 – Scanning electron microscopy image of (from left to right) red blood cell, platelet and white blood cell. Image by Electron Microscopy Facility at The National Cancer Institute at Frederick, freely available in the public domain (EDinformatics, 1999).*

### 2.2.2 Heart

Blood is pumped around the cardiovascular system by the heart. The heart is a muscular organ, with its walls comprising of an endocardium, myocardium and epicardium (figure 2. 2) (Betts et al., 2013). The myocardium is the thickest layer of the heart wall, and is comprised mainly of muscle cells built on collagenous fibres. The myocardium is also the layer of heart tissue that contains the coronary circulatory system, which supplies blood to the heart tissue (section 2.2.4). The endocardium layer of the heart is in contact with the blood, and is comprised of endothelial cells. The heart muscle is in diastole when it relaxes, allowing blood to flow into the heart and ventricles. Systole occurs when the heart contracts, squeezing the blood out of the ventricles (figure 2. 3).

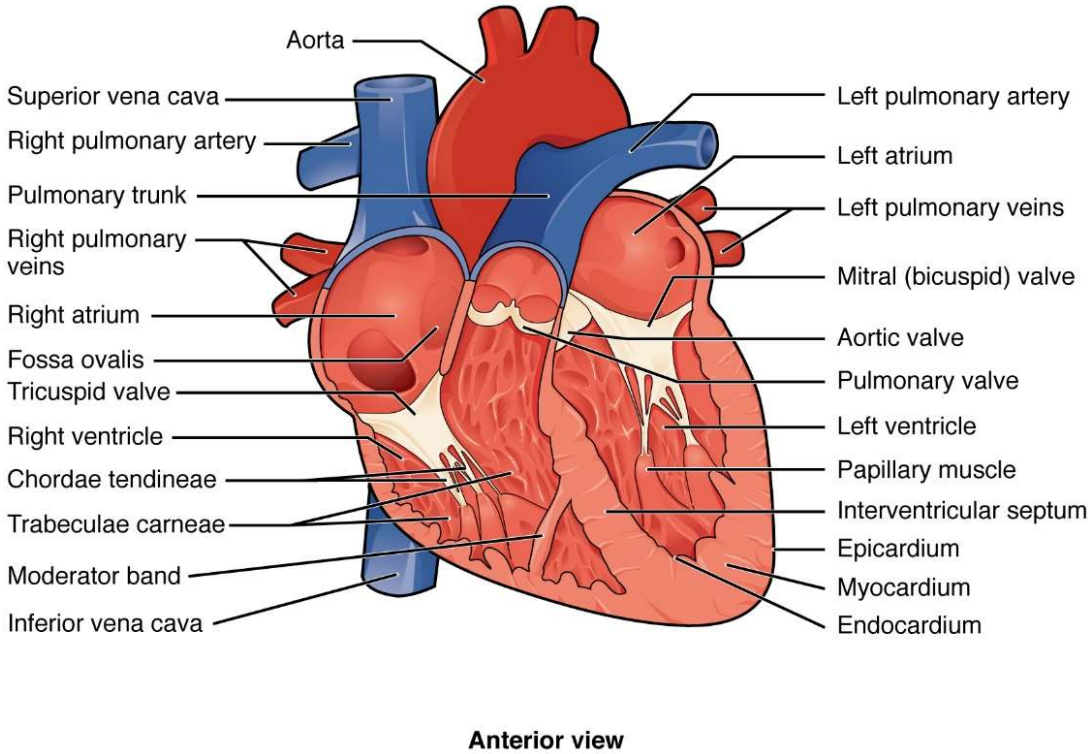


*Figure 2. 2 – Internal structure of heart. Image by OpenStax College, available under Create Commons Attribution 3.0. (Betts et al., 2013).*

The right side of the heart pumps deoxygenated blood to the lungs, and the left side of the heart pumps oxygenated blood around the body (figure 2. 5). Thus, the evolution of the heart has created much thicker muscle tissue on the left side of the heart due to the increased forces needed to pump blood around the body. During diastole, blood fills the right and left ventricles by passing through the tricuspid and mitral valves, respectively. As the ventricle contracts during systole, the tricuspid and mitral valves close with the back pressure of blood, thus ensuring blood flows in the correct direction. The blood exits the ventricles through the pulmonary and aortic valves. Pressure within the heart is shown in figure 2. 4, with the recognisable “lub” and “dub” sounds associated with a healthy heart beat (Betts et al., 2013).

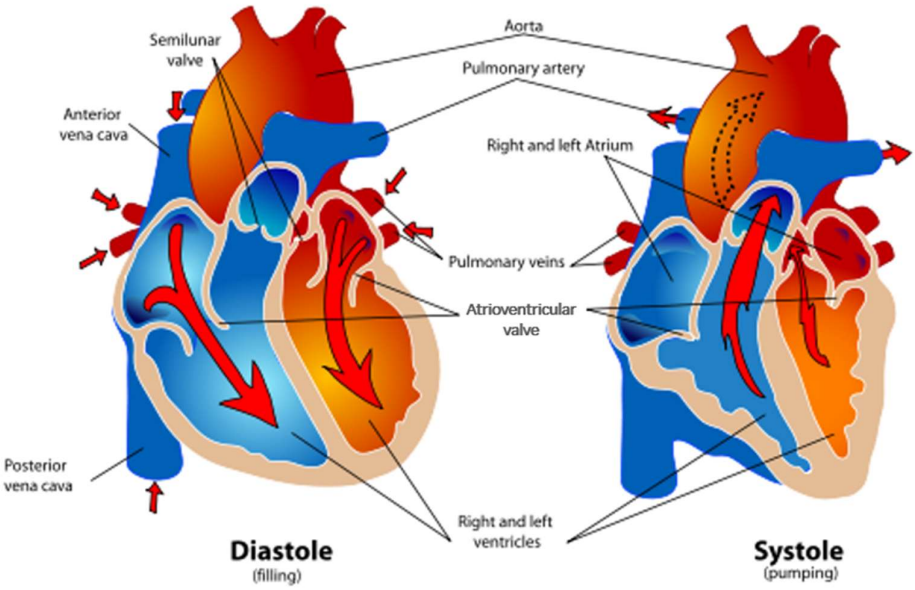


*Figure 2. 3 – Diastole and systole of heart. Image by Mariana Ruiz Villarreal, freely available in the public domain (BiologyGuide, 2012).*

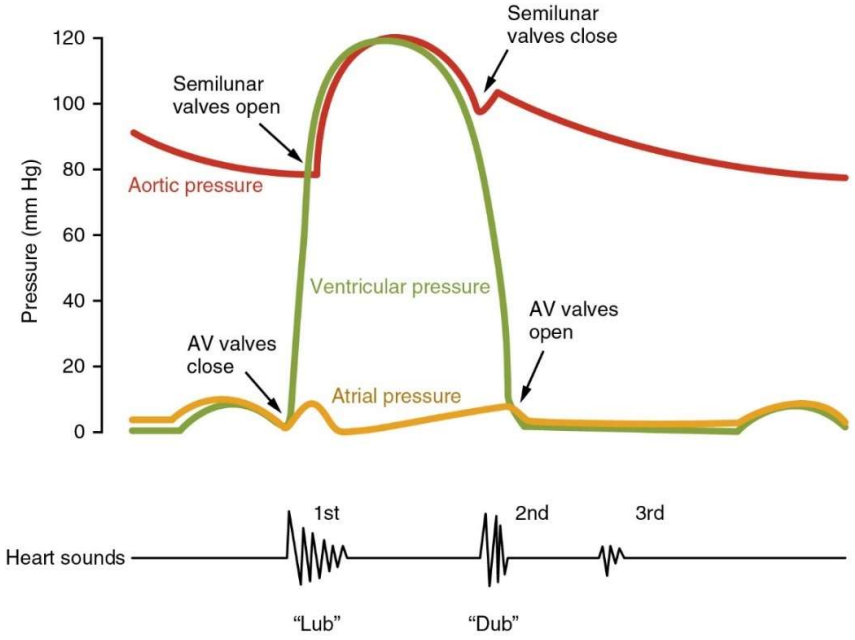


*Figure 2. 4 – Wiggers diagram - cardiovascular cycle of pressure over time in the left ventricle. AV (atrioventricular) valves - tricuspid and mitral. Semilunar valves – aortic and pulmonary. Image by OpenStax College, available under Create Commons Attribution 3.0. (Betts et al., 2013).*

### 2.2.3 Bloods vessels

Blood travels away from the heart in arteries and returns in veins (figure 2. 5). The system within the body that contains the heart, arteries and veins is called the cardiovascular, or circulatory, system. Arteries and veins are comprised of three layers, the tunica adventitia (also known as tunica externa), tunica media and tunica intima (figure 2. 6) (Betts et al., 2013). The tunica adventitia is primarily made of collagen fibres, with some elastic fibres, to form the connective tissue. The tunica media layer comprises of smooth muscle cells, supported by elastic fibres aligned circumferentially in sheets. However, towards the outer layer of the tunica media the muscle tends to be aligned more longitudinally. The tunica intima is in contact with the blood, and is comprised of endothelial cells. Veins have the same three structural layers, however the media layer is much thinner. Connecting the arteries and veins are capillary networks (figure 2. 5).

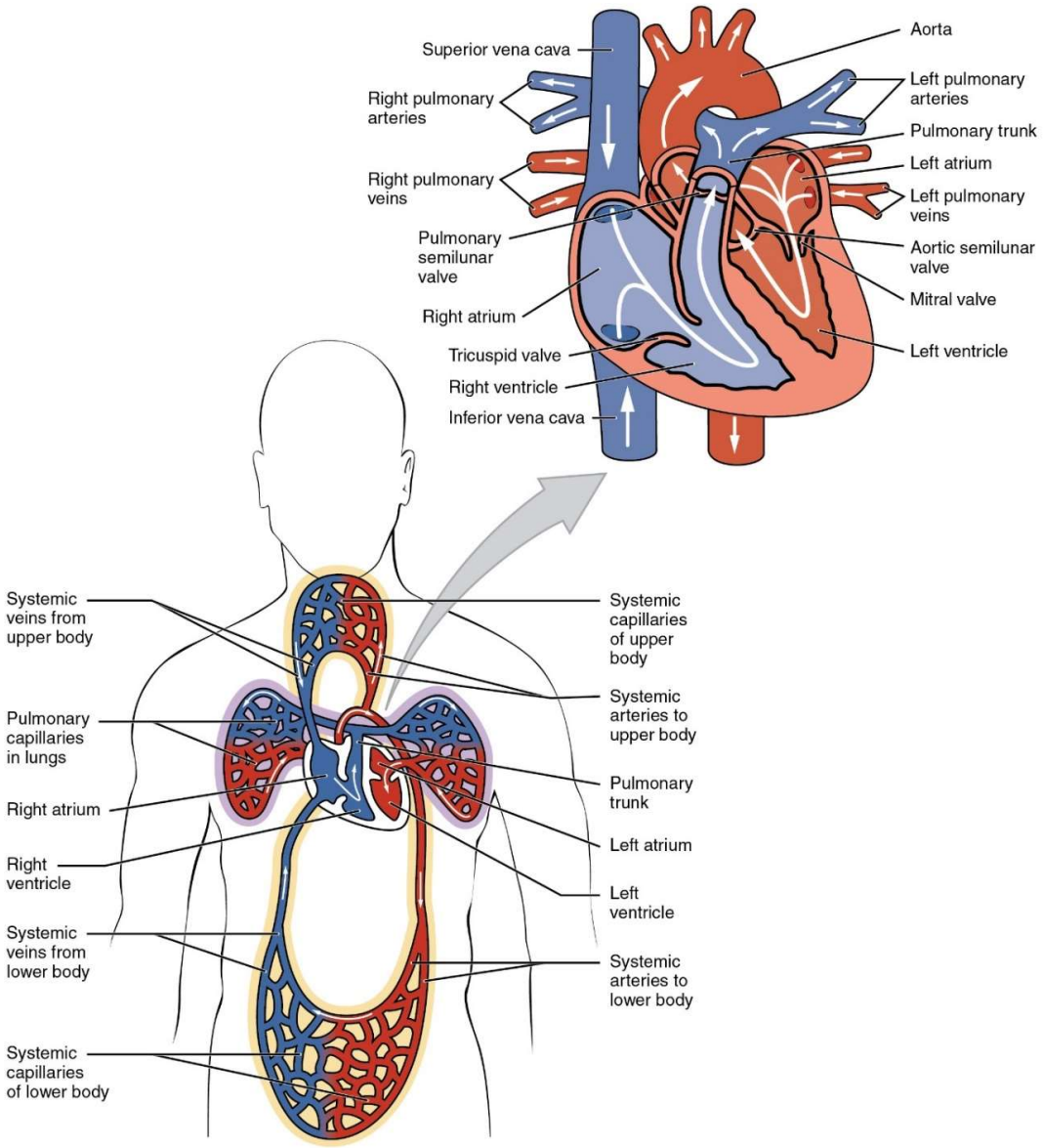


*Figure 2. 5 – The cardiovascular system supplying oxygenated blood from the heart to the body, and delivering deoxygenated blood back to the heart. Breakout of heart showing blood flow within the heart, the right side (blue) receiving deoxygenated blood and pumping to the lungs and the left side (red) pumping oxygenated blood around the body. Image by OpenStax College, available under Create Commons Attribution 3.0. (Betts et al., 2013).*

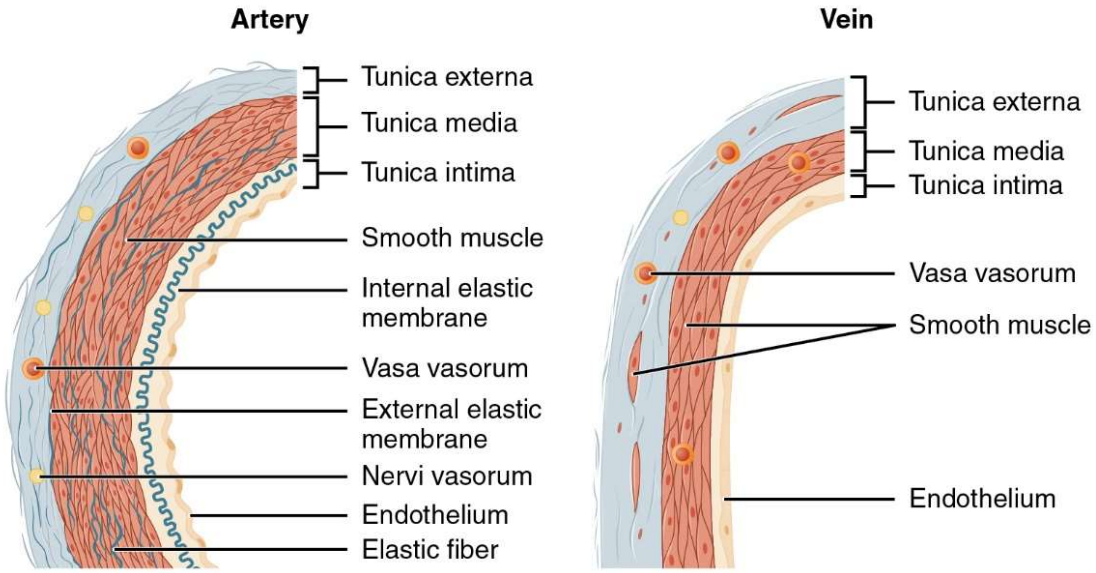


*Figure 2. 6 – Cross sectional view of an artery and vein. Image by OpenStax College, available under Create Commons Attribution 3.0. (Betts et al., 2013).*

### 2.2.4 Coronary circulatory system

The heart muscle has its own vessels to supply blood to the myocardium, called the coronary circulation system (figure 2. 7). The coronary arteries supply oxygenated blood to the heart muscle, and therefore these arteries are required to cover a large surface area of the heart. The arteries are split into two trees, the left and right coronary arteries. The arteries begin at the start of the aorta, receiving a supply of the highest oxygenated blood from the heart (figure 2. 7). The right coronary artery supplies both ventricles, the right atrium, and the sinoatrial node. The left coronary artery supplies both ventricles and the left atrium (Betts et al., 2013). However, due to natural variation the exact supply to certain areas of the heart can vary from patient to patient (Mazur et al., 2013). After supplying blood to the myocardium, the coronary circulatory systems returns blood to the heart via the coronary veins. After circulating the body, deoxygenated blood enters the heart through

the superior and inferior venae cavae, whereas oxygenated blood returns from the lungs through the pulmonary veins (figure 2. 5).

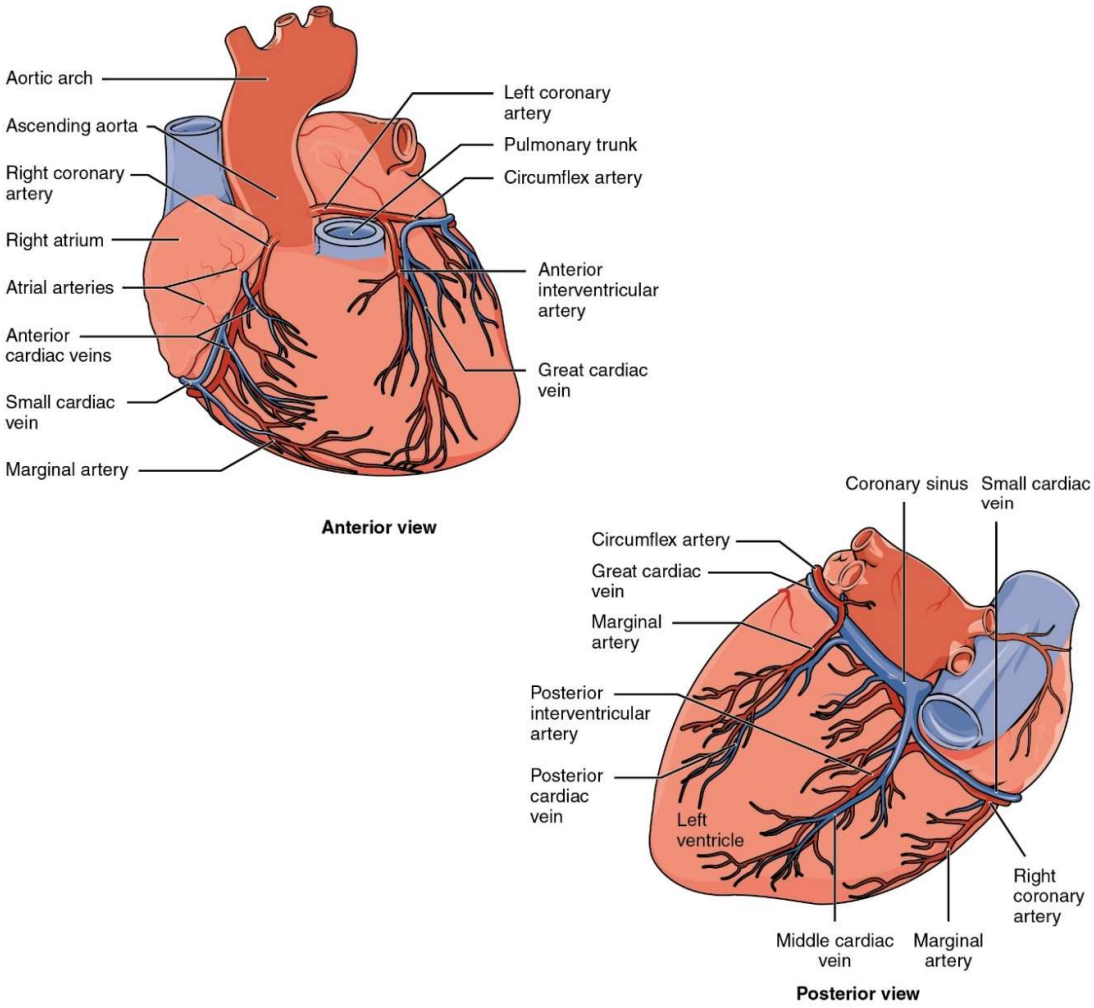


*Figure 2. 7 - Coronary circulation system. Image by OpenStax College, available under Creative Commons Attribute 3.0 (Betts et al., 2013).*

### 2.2.5 Coronary heart disease

Coronary heart disease (CHD) is the leading cause of mortality worldwide (Townsend et al., 2015). In 2015, over 69,000 deaths and over half a million inpatient episodes were due to CHD in the UK (British Heart Foundation, 2017). CHD is caused by a restriction in coronary

artery blood flow due to narrowing of the arteries (stenosis) associated with atherosclerosis (figure 2. 8). Ischaemia is when the blood supply is restricted to tissue, through tissue disease, arteriosclerosis (thickening/hardening of the arterial walls, including atherosclerosis) and embolisms, which can result in a myocardial infarction (heart attack) and potentially death. Irreversible cell death (necrosis) can occur in the heart muscle if inadequate oxygen is delivered to the cells (National Heart, 2016), preventing the heart from pumping blood effectively around the body.

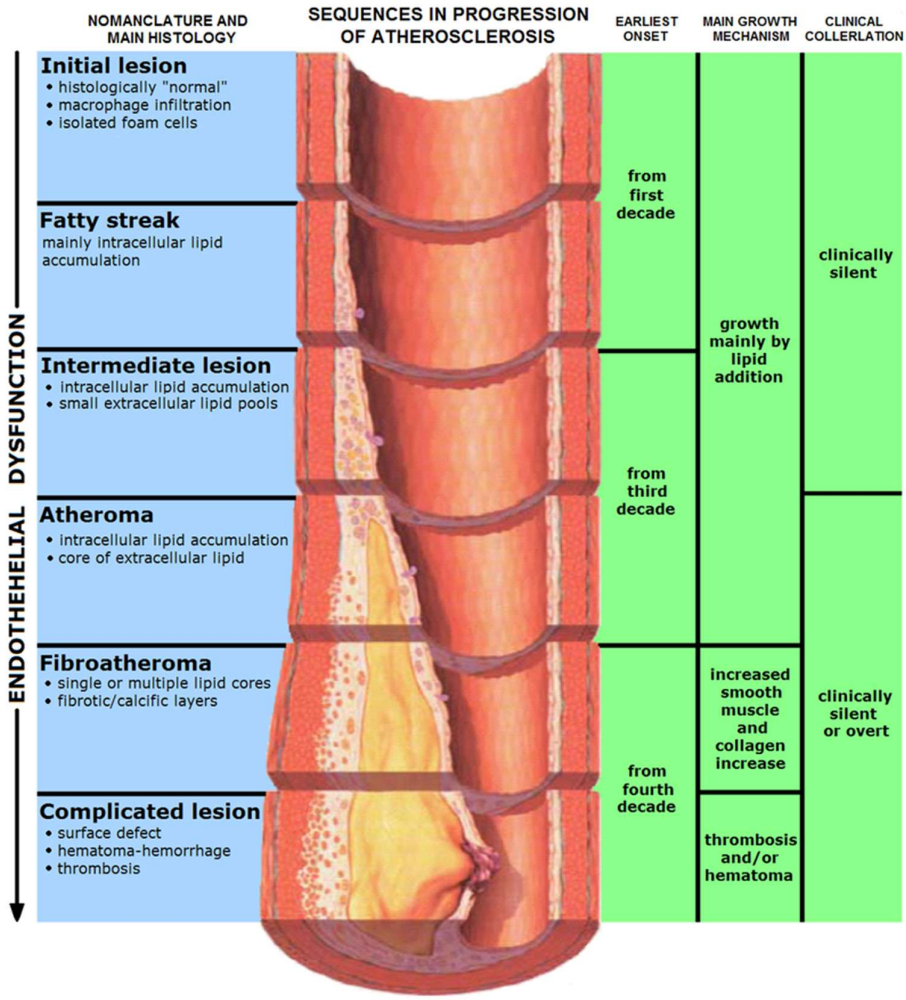


*Figure 2. 8 – Atherosclerosis progression. Image by Graham Childs, available under Creative Commons Attribute 3.0 (Pescador, 2014).*

All arteries within the body can suffer from atherosclerosis, but it is more prevalent in those that supply blood to the heart, brain and legs, known as the coronary, carotid and peripheral respectively. The build-up of atheroma begins from a young age, with studies noticing the fatty material in patients as young as teenagers in their second decade of life (Ylä-Herttuala et al., 1986).

Atherosclerosis is the build-up of plaque on artery walls, causing narrowing of vessels (Ross, 1999). A type I lesion (initial lesion - figure 2. 8) is identifiable by an increase in the number of intimal macrophages (a type of white blood cell) (Stary et al., 1994). The macrophages 'eat' the low-density lipoproteins ('bad' cholesterol), a process known as phagocytosis. They can become overloaded by the lipoprotein and form foam cells, and an accumulation of lipids (Stary et al., 1994). A type II lesion (fatty streak - figure 2. 8) contains layers of macrophage foam cells and lipid droplets (Ayyappan, Paul, and Goo, 2016). Type III lesions (intermediate lesion - figure 2. 8) contain pools of lipid, in addition to the foam cells and lipid droplets. At this point, atheroma (type IV lesions) can form (figure 2. 8), which contain a lipid core. The atheroma is recognised as a foreign body by the immune system and so inflammation occurs. In an attempt to repair itself the artery seals the atheroma by a fibrous cap (type V lesion; fibroatheroma - figure 2. 8), which over time forms plaque. A snowballing effect occurs where the plaque within the artery encourages more atheroma to build-up, causing more inflammation to the area. The core becomes necrotic if the foam cells die, creating further inflammation in the area and attracting more white blood cells. As the atherosclerosis increases and plaques harden, the artery becomes more occluded (National Heart, 2016).

A vulnerable plaque may rupture eventually, removing the barrier between blood and the fatty core. The thrombogenic core is released and thrombus formation occurs at the rupture site. The blood clots further occlude the artery. Occasionally clots can become dislodged and travel along the blood stream, in severe cases resulting in myocardial infarction or a stroke (Bentzon et al., 2014).

### 2.2.6 Medical intervention

Coronary artery disease is normally treated through either percutaneous coronary intervention (PCI) or coronary artery bypass grafting (CABG) surgery. These may require the use of a stent or an appropriate blood vessel respectively. Medical intervention can reduce the likelihood of a myocardial infarction with procedures such as angioplasty or stent insertion to reopen the artery, or creating a bypass for blood flow to avoid blockages. More than 92,000 PCI procedures are carried out annually in the UK, and just under 17,000 CABG procedures are performed (Townsend et al., 2015). In total, £6.8 billion was spent by the National Health Service (NHS) in the UK in 2012/13 on treating CVD, for both primary and secondary care (Townsend et al., 2014). CVD includes CHD, strokes, peripheral artery disease and aortic disease. Although only £1.6 billion of this expenditure is designated as treatment for CHD, the actual cost of CHD is expected to be significantly greater. This is due to the error in the collection of data by the NHS, where different geographical areas use different categories for documenting CVD treatment. Therefore, in some regions CHD care falls under the category of 'other CVD', which in total has an expenditure of £4.4 billion. Additionally, the cost to the UK is significantly greater if the loss of production due to morbidity and mortality is considered, and also the cost of additional care provided by individuals. Loss of

production alone costs the UK a further £6 billion, and £3.8 billion in informal care (Townsend et al., 2014).

#### *2.2.6.1 Coronary artery bypass grafting*

CABG uses an alternative blood vessel to circumvent a blocked coronary artery (figure 2. 9). Natural tissue grafts have the most successful results compared to artificial alternatives, as they most closely match the mechanical and physical properties of the area (Endo, 2000). This is especially the case if the graft has come from an alternate vein of the same patient, being less likely to be rejected by the body. However, it is not always possible to find a healthy donor graft, and sometimes the patient's vein is not suitable, therefore a synthetic alternate may be chosen (Desai, Seifalian, and Hamilton, 2011).

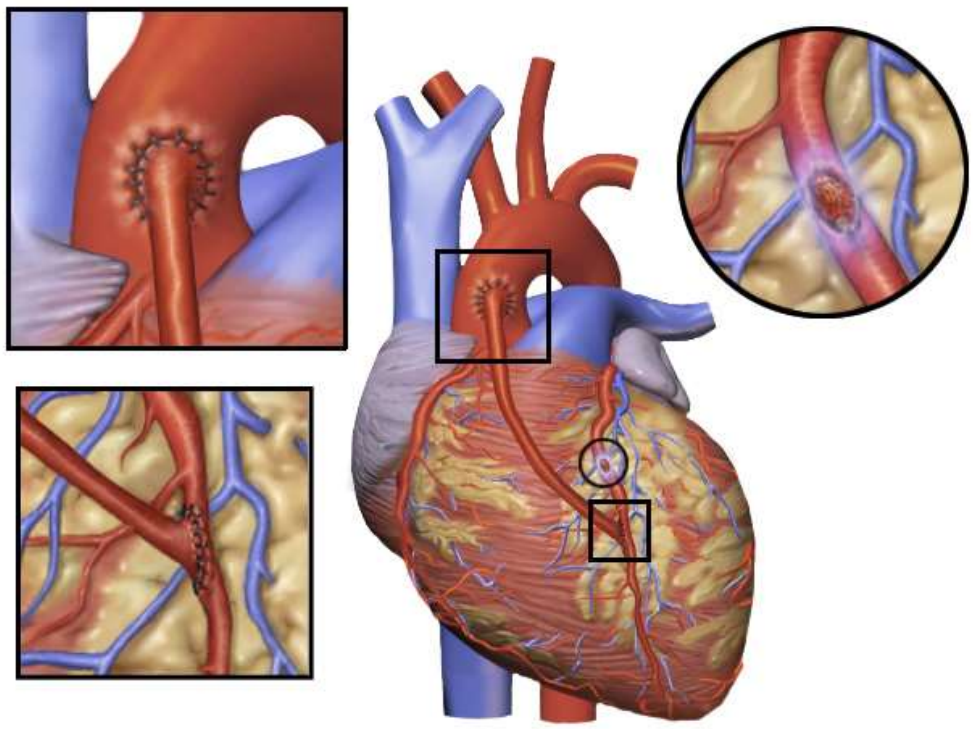

*Figure 2. 9 – CABG. Image by Bruce Blaus, available under Creative Commons Attribute 4.0 (Howlett, 2016).*

Although CABG was popularised in the mid-1960s by René Favaloro (Head et al., 2013), the first CABG procedure was performed in 1962 by David C. Sabiston with a human autogenous saphenous vein graft, although the patient died 3 days after surgery (Cheng, 2012). Vasilii Kolesov used an internal mammary artery for CABG in 1964, and he is cited as performing the first successful CABG procedure (Head et al., 2013).

Internal mammary artery or radial artery most commonly chosen for CABG (Mohr et al., 2011), as venous grafts have demonstrated early failure (Fitzgibbon, Burton, and Leach, 1978). Various synthetic grafts have been explored, including Gore-Tex grafts that were investigated in 1978, but they were associated with high thrombogenicity and poor patency rates (Molina, Carr, and Yarnoz, 1978). More successfully, expanded polytetrafluoroethylene and woven polyethylene terephthalate are used for synthetic coronary artery grafts currently (Desai, Seifalian, and Hamilton, 2011). There is also interest in the use of biopolymers for creating grafts, such as chitosan or cellulose. Altering the ratio of biopolymer can create a material with compliance similar to that of coronary artery (Azevedo et al., 2013). The range of Young's modulus in Azevedo's study varied from 0.65 to 1.35 MPa, which is within the range measured for human arteries in other studies (table 2. 3).

#### *2.2.6.2 Percutaneous coronary intervention*

PCI involves a blocked artery being reopened to allow blood to flow naturally, usually by inflating a device similar to a balloon within the artery, known as an angioplasty (figure 2. 10). This compresses the plaque to the walls of the artery, and once the inflating device has been removed the artery remains open (Newsome, Kutcher, and Royster, 2008). The first

coronary angioplasty was performed by Grüentzig and Myler in 1977 (Mueller and Sanborn, 1995). Angioplasty is prone to restenosis (the reoccurrence of stenosis), due to damage caused by the procedure. Inflation of the vessel can cause elastic recoil in 25-30% of patients, resulting in narrowing of vessels at around 6 months. In more extreme cases, restenosis can occur within 24 hours of surgery due to vessel dissection or thrombus formation (Hamid and Coltart, 2007). Therefore, angioplasty is normally coupled with the insertion of a stent to reduce the likelihood of restenosis (Fowkes and Gillespie, 1998).

A stent is inserted into an artery as part of a PCI to maintain the lumen diameter (figure 2. 10). Original designs of stents by Alex Carrel in 1912 included paraffin covered glass and metal tubes (Newsome, Kutcher, and Royster, 2008). The first stent, reported by Wright, was a stainless steel implant with a zig zag shape, which was implanted into dogs (Wright et al., 1985). In 1986, Jacques Puel implanted the first self-expanding stent into humans (Sigwart et al., 1987). This design of stent is known as a bare metal stent (BMS) and is similar to modern stents. A BMS is a mesh tube that is usually expanded by inflating a balloon once it has been positioned at the desired site. The balloon is then removed leaving the stent in an expanded position, which opens the artery and allows blood to flow freely (Song, Kim, and Yoon, 2013). Both the expanded and compressed states of a stent are displayed in figure 2. 11. Stenting reduces the rate of restenosis by 10% compared to angioplasty alone (Hamid and Coltart, 2007).

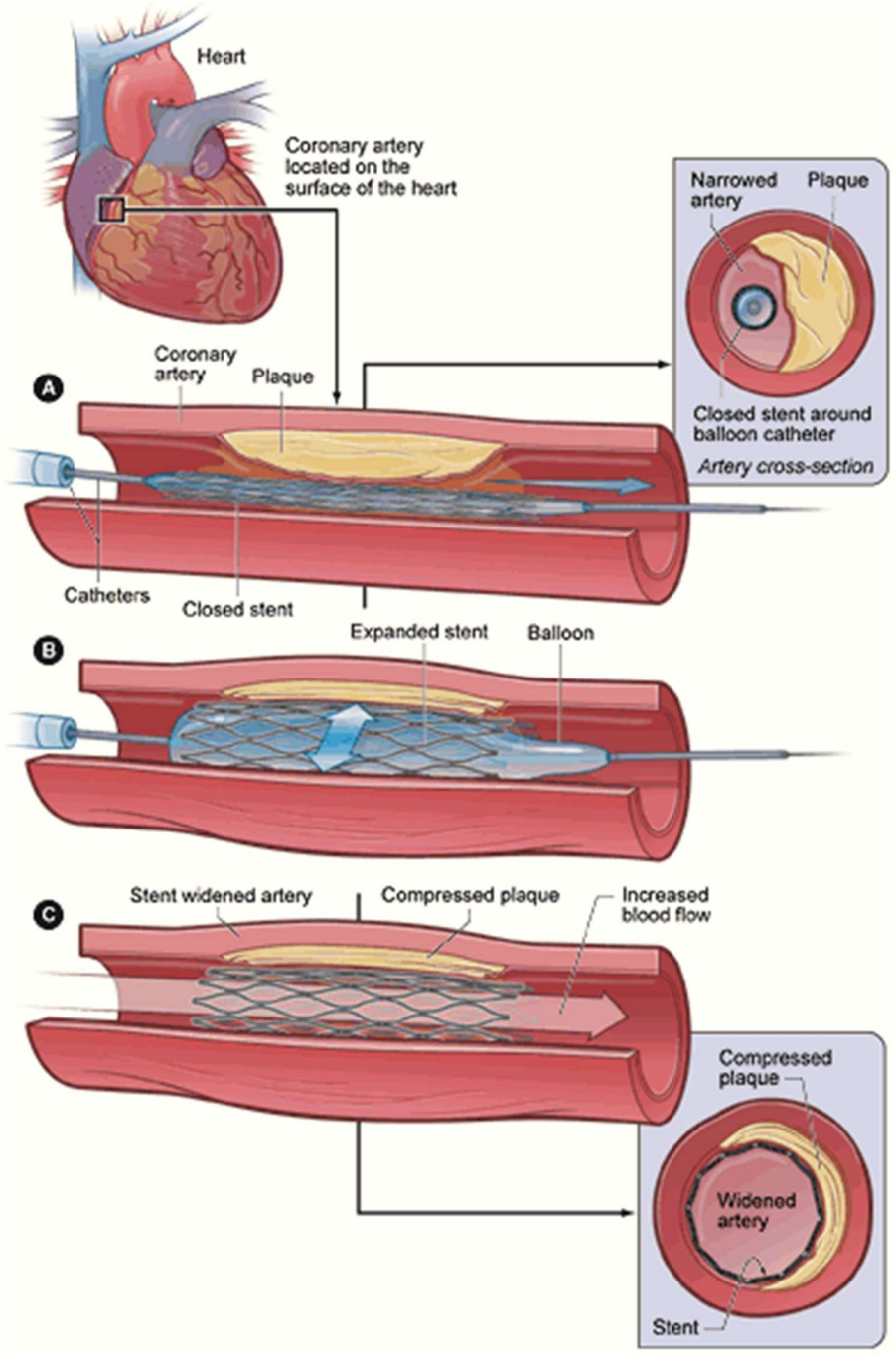


*Figure 2. 10 – Coronary angioplasty and stent placement. Image by National Institutes of Health, freely available in the public domain (Schmidler, 2017).*

Damage to an artery associated with angioplasty was reported by the NHS to occur in less than one in every 100 cases due to sheath insertion, and in one in every 350 cases

damage was caused to an artery in the heart (HealthUnlocked, 2015). In addition to damage caused by angioplasty, inserting a stent can inflict damage to the surface of arteries due to the struts in stent design (figure 2. 11). This damage can cause an inflammatory response, with early thrombosis seen within the first few hours, and neointimal hyperplasia occurring a few months, following surgery.

Thrombosis is a complication associated with stents that is manageable with antiplatelet therapy (Coolong and Mauri, 2006). Thus, the primary complication now associated with BMS is re-occlusion due to neointimal hyperplasia (cell proliferation over stent), an inflammatory response to damage of the wall during stent placement. This has led to the development of drug eluting stents (DES), where the BMS is coated with an antiproliferative or anti-inflammatory drug, which shows the potential to reduce the rate of restenosis. DES are either formed through the addition of a biodegradable coating that releases a drug whilst in situ, or through the use of texturing to attach the drug directly to the surface (O'Brien et al., 2016). Microporous surfaces allow for drug attachment (Tada et al., 2010), as do specially created reservoirs on the surface (Krucoff et al., 2008). There is also a large interest in biodegradable materials, which would eventually leave the coronary artery with no foreign body within the lumen (Boland, Grogan, and McHugh, 2017; Zhu et al., 2017), thus decreasing complications associated with restenosis further. Neointimal hyperplasia is still a major concern for PCI, as despite progressions in stent design, DES have only reduced rates of restenosis to less than 5% (Hamid and Coltart, 2007).

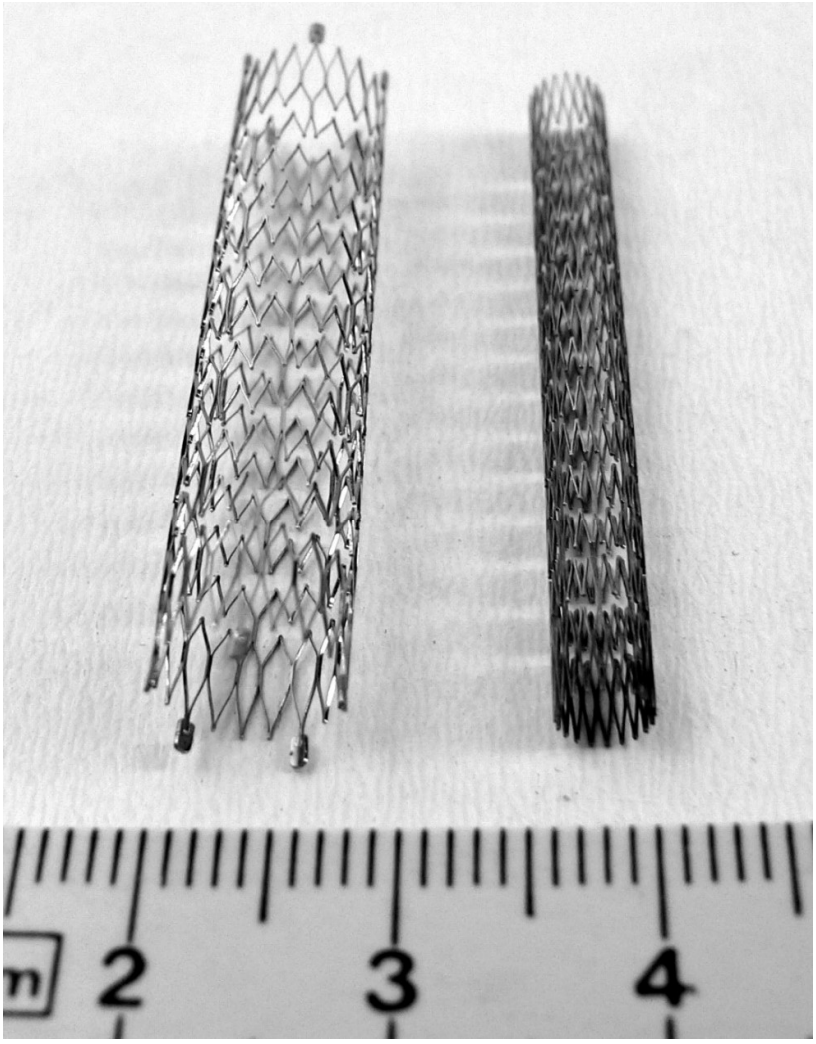


*Figure 2. 11 – Stent in expanded (left) and compressed (right) state. Image by Frank C. Müller, available under Creative Commons Attribute 2.5 (Müller, 2008).*

### 2.2.7 Endothelium

The endothelium of blood vessels is in contact with blood flowing through the cardiovascular system. The endothelial cells align and elongate in the direction of fluid flow (Eskin et al., 1984). In addition to providing a barrier function allowing nutrients and waste products to permeate, the vascular endothelial cells that line the vessels are non-thrombogenic. The design of medical devices, such as blood pumps, have evaluated the

effect of surface roughness on coagulation properties, and found that an increase in surface roughness increased platelet adhesion, associated with blood clot formation (Linneweber et al., 2007). This emphasises the importance in characterising the surface of coronary arteries to enable to development of novel biomaterials that replicate natural arteries.

## 2.3 Surface Roughness

### 2.3.1 Measuring surface roughness

Tribology is the study of surfaces in relative motion. It enables friction, lubrication and wear properties of materials to be characterised. Surface roughness can influence these properties, as it is a measure of the fluctuations in height of a surface (figure 2. 12). Surface roughness can be measured by contact methods, for example tactile profilometer or atomic force microscopy (AFM), or non-contact methods such as optical microscopy or scanning electron microscopy (SEM).

To evaluate the roughness of a surface, there are a variety of options to consider. Primarily, there is the option to measure the roughness along a profile or over an area (denoted by the letters *R* and *S* respectively, followed by subscript letters accordingly). Additionally, there are numerous parameters of surface roughness. The profile values are described in table 2. 1. Traditional methods, such as tactile profilometer and AFM, measure surface roughness over a profile. However, some profilometry methods collect surface data at varying optical focus or angle position. This enables the three-dimensional (3D) reconstruction of a surface. The G4 Infinite Focus (G4 Infinite Focus, Alicona UK, Kent, UK)

microscope uses optical focal variation to image a 3D surface (chapter 3.2.3). The Quad Back Scatter Electron detector of the Hitachi TM3030 (Hitachi Ltd., Tokyo, Japan) SEM uses angle variation and image stitching to create a 3D surface from two-dimensional (2D) images (chapter 4.2.4).

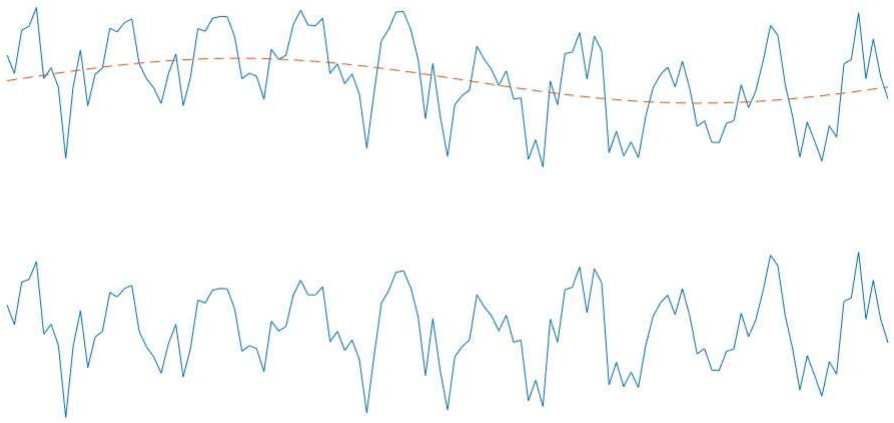

*Figure 2. 12 – Surface with waviness and roughness (top), and with waviness removed (bottom).*

*Table 2. 1 - Surface roughness parameters (ISO 4287, 2009).*

| Description | Profile | Profile equation |
|---|---|---|
| Arithmetic mean deviation of assessed profile | $R_a$ | $R_a = \frac{1}{l}\int_o^l \lvert Z(x)\rvert \, dx$ |
| Root mean squared of assessed profile | $R_{rms}$ | $R_{rms} = \sqrt{\frac{1}{l}\int_o^l Z^2(x)\, dx}$ |
| Maximum profile valley depth of assessed profile | $R_v$ | $R_v = \lvert \min(Z(x)) \rvert$ |
| Maximum profile peak height of assessed profile | $R_p$ | $R_p = \max(Z(x))$ |
| Total height of assessed profile | $R_t$ | $R_t = R_p + R_v$ |
| Skewness of assessed profile | $R_{sk}$ | $R_{sk} = \frac{1}{R_{rms}^3}\left[\frac{1}{l}\int_o^l Z^3(x)\, dx\right]$ |

In table 2. 1, *l* is the sampling length, *Z* is the profile height, and *x* is the position along the sampling profile. $R_{sk}$ assesses the skewness over the profile length, and describes the symmetry about the centre line of peaks and valleys. $R_p$ is commonly used to evaluate the frictional force of a surface, and $R_V$ can be associated with the strength of a surface, for example by corrosion resistance. $R_{rms}$ is commonly used in USA, and presents a similar analysis of surface roughness as $R_a$. However, $R_a$ uses an average value over the sampling length, thus the results are statistically stable and not influenced by damage along the profile line as significantly as $R_{rms}$ (Oliveira et al., 2012). Table 2. 2 presents the equivalent surface roughness parameters calculated over an area rather than a profile (displayed with a prefix of *S* rather than *R*), where *A* is the area assessed, *x* is the position along the *x* axis and *y* the position along the *y* axis of the profile area.

*Table 2. 2 – Surface area roughness parameters (ISO 25178, 2012).*

| Description | Profile | Profile equation |
|---|---|---|
| Arithmetic mean deviation of assessed area | $S_a$ | $S_a = \frac{1}{A} \iint_A \lvert Z(x,y) \rvert \, dxdy$ |
| Root mean squared of assessed area | $S_{rms}$ | $S_{rms} = \sqrt{\frac{1}{A} \iint_A Z^2(x,y) \, dxdy}$ |
| Maximum profile valley depth of assessed area | $S_v$ | $S_v = \lvert \min(Z(x,y)) \rvert$ |
| Maximum profile peak height of assessed area | $S_p$ | $S_p = \max(Z(x,y))$ |
| Total height of assessed area | $S_t$ | $S_t = S_p + S_v$ |
| Skewness of assessed area | $S_{sk}$ | $S_{sk} = \frac{1}{S_{rms}^3} \left[ \frac{1}{A} \iint_A Z^3(x,y) \, dxdy \right]$ |

Fractal dimension can also be used to describe the surface as a ratio describing how fractal pattern changes with scale. Fractal geometry was developed by Benoit Mandelbrot, who described shapes in nature as such: “Clouds are not spheres, mountains are not cones, coastlines are not circles, and bark is not smooth, nor does lightning travel in a straight line”. Fractal geometry uses iterative calculations to define infinitely complex shapes. For example, figure 2. 13 presents a descriptive representation of fractal dimension. If an object is positioned in dimension *D*, and its linear size is reduced by 1/*r* in each spatial direction, where *r* is scaling factor, then the measurement (*N*) of the object would increase to $N = r^D$ of its original measure. Fractal dimension (*FD*) is calculated using equation 2. 1, and represents how complicated a self-similar object is. The Hausdorff principle of fractal dimension highlights the significance of multi-scale analysis, and that to characterise surface roughness more critically it should be measured and assessed at a range of scales.

Equation 2. 1

$$FD = \frac{\boldsymbol{log_{10}}\ N}{\boldsymbol{log_{10}}\ r}$$

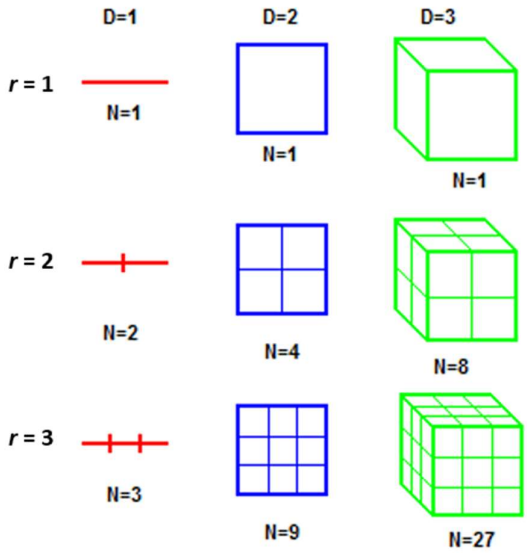


*Figure 2. 13 – Hausdorff principle of fractal dimension in three dimensions. Image by Brendan Ryan, freely available in the public domain (Vanderbilt University, 2007).*

### 2.3.2 Application to cardiovascular biomaterials

The surface roughness of cardiovascular materials can prevent thrombus formation and bacterial infection, and encourage endothelialisation (Ross and Lahann, 2013). Macro scale surface roughness can be created through traditional methods, such as machining and polishing (Alla et al., 2011). However, with the development and availability of new processes and materials, textures can be created at both a micro- ($\times 10^{-6}$) and nano- ($\times 10^{-9}$) scale, through various techniques such as sand blasting, acid etching, laser treatment and nano-particle coatings (Vignesh, Bhuminathan, and Santhosh, 2015).

In orthopaedic scenarios, the use of micro- and nano-scale surface roughness can improve osseointegration of implants due to osteoblast differentiation (Gittens et al., 2011). Roughness has also been shown to reduce bacterial adhesion (Lorenzetti et al., 2015). In cardiovascular applications, surface roughness has been investigated to improve

haemocompatibility (Vladkova, 2013). Superhydrophibic surfaces have been created that reduce platelet adhesion, and multiscale surfaces have been formed through moulded polydimethylsiloxane (Le et al., 2013). Surface roughness has been investigated to enhance endothelial cell proliferation, including through the use of 3D printed resins (Lu et al., 2016). It has been found that at >2 µm, an increase in surface roughness creates a larger area for platelet surface adhesion, forming a more thrombogenic surface; between 2 µm and 50 nm, surface topography can reduce the contact area for platelet adhesion, and at less than 50 nm, the surface is considered smooth for platelets (Chen, Han, and Jiang, 2011).

### 2.3.3 Surface roughness of other biological tissue

The surface roughness of various biological tissue has been measured, for example the $R_a$ of bovine articular cartilage measured 0.24 ± 0.08 µm through stylus profilometry (Forster and Fisher, 1999). The effect of disease on surface roughness of biological tissue has also been studied, with Peng et al. investigating the effect of osteoarthritis on surface roughness of human articular cartilage (Peng and Wang, 2013). Measured with AFM at the nano-scale, healthy cartilage had $S_a$ of 68.9 nm, compared to osteoarthritic cartilage which varied from 110.4 to 119.2 nm. At the micro-scale measured with a 3D laser scanner, $S_a$ only identified a difference in extreme osteoarthritis (58.40 ± 14.56 µm) compared to healthy cartilage (9.56 ± 1.84 µm), however the fractal dimension, $S_{fd}$, identified a significant difference between healthy articular cartilage and all stages of osteoarthritis.

In vascular biology the fractal dimension of blood vessel patterns has been investigated (Sandau and Kurz, 1997), concluding that capillary pattern complexity of chick vessels increased with growth factors. Ultrasound scans were performed on murine carotid

arteries to assess the fractal dimension of atherosclerotic arteries texture, although no significant difference was noted between healthy and diseased arteries (Niu et al., 2013). These studies have not investigated the endothelial surface of coronary arteries, rather the fractal dimensions of vessel patterns and cross sections within the vascular system. However, the results demonstrate the significance and potential of multi-scale analysis in cardiovascular applications.

## 2.4 MECHANICAL PROPERTIES

### 2.4.1 Stress and strain

Stress (σ) is the measurement of an applied force over an area (equation 2. 2), typically measured in N/mm$^2$ (i.e. MPa) for biological tissues. Strain (ε) is the measurement of the change in displacement over the original length (equation 2. 3).

*Equation 2. 2*

$$\sigma = \frac{\mathrm{F}}{\mathrm{A}}$$

*Equation 2. 3*

$$\varepsilon = \frac{\Delta L}{L}$$

*F* is applied force (N), *A* is area (mm$^2$), Δ*L* is the change in length (mm), and *L* is the original length (mm) (figure 2. 14).

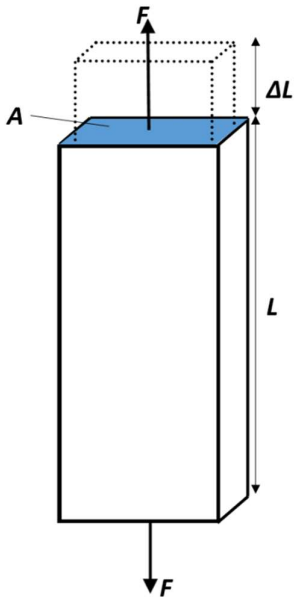


*Figure 2. 14 – Specimen subjected to tensile force (F), with cross sectional area (A), original length (L) and change in length (ΔL).*

The Young's modulus (*E*) of a material is the measurement of elasticity of a material, calculated as stress over strain (equation 2. 4), with units of Pa.

*Equation 2. 4*

$$E = \frac{\sigma}{\varepsilon}$$

### 2.4.2 Mechanical properties of arteries

Mechanical properties of coronary arteries have been characterised for both human (Ozolanta et al., 1998; Van Andel, Pistecky, and Borst, 2003; Karimi et al., 2013) and porcine (Van Andel, Pistecky, and Borst, 2003; Lally, Reid, and Prendergast, 2004; Wang et al., 2006) arteries. Uniaxial tests have been performed on coronary arteries to calculate tensile strength (Claes et al., 2010) and Young's modulus (Karimi et al., 2013; Grishina, Kirillova, and Glukhova, 2016) of the material. Tensile tests have been performed on separate layers of the

coronary artery (intima, media and adventitia) (Holzapfel et al., 2005). Material properties, though, are dependent on direction (Yang et al., 2009), with stress in the circumferential 'direction' (i.e. aligned with the circumference of the artery) being greater than that longitudinally (i.e. along the length of the artery). Thus, biaxial testing has been of interest with stress-strain characterisation of, for example, diseased coronary arteries (Kural et al., 2012). To further maintain the physiological state, pressurised tests have been used to measure deformation of vessels that allow characterisation of the stress-strain relationship. Such tests have been used to calculate the elasticity of coronary arteries (Veress et al., 2000). A typical assumption for most tests is that coronary arteries are incompressible, with Karimi *et al.* recently measuring the Poisson's ratio of both healthy and atherosclerotic human coronary arteries to justify this assumption (Karimi et al., 2016). These studies have quantitatively measured mechanical properties (table 2. 3) but they ignore the intrinsic viscoelasticity of the coronary artery.

*Table 2. 3 – Mechanical properties of coronary arteries from literature.*

| Testing method | Model | Mechanical Properties | Study |
|---|---|---|---|
| Pressurised test | Human | Tangential elastic modulus (Young's)<br><br>Left artery: 0.90 ± 0.48 to 4.11 ± 0.89 MPa<br>Right artery: 1.06 ± 0.24 to 2.85 ± 0.76 MPa | *(Ozolanta et al., 1998)* |
| Pressurised test<br><br>Data presented in stress-strain graph format as 'envelopes' | Human and porcine | Stress - strain in circumferential direction<br><br>Circumferential: <100 kPa up to 30% (human) and <180 kPa up to 75% (porcine)<br>Axial: <180 kPa up to 30% (human) and 240 kPa up to 80% (porcine)<br><br>Demonstrates non-linear relationship for stress-strain curve | *(Van Andel, Pistecky, and Borst, 2003)* |
| Tensile test | Human | Elastic modulus<br><br>Healthy: 1.48 ± 0.24 to a maximum of 1.55 ± 0.26 MPa<br>Atherosclerotic: 3.77 ± 0.38 to a maximum of 4.53 ± 0.43 MPa | *(Karimi et al., 2013)* |
| Uniaxial and equibiaxial tensile test | Porcine | Young's modulus<br><br>Uniaxial: 10 ± 7 MPa<br>Equibiaxial: 26 ± 9.5 MPa | *(Lally, Reid, and Prendergast, 2004)* |
| Inflation and axial extension (biaxial)<br><br>Data presented in stress-strain graph or as constants | Porcine | Stress – strain in circumferential direction<br><br>Left artery: 60 ± 10 kPa (media); 40-50 kPa (intact)<br>Right artery: 100 ± 25 kPa (media); 40- 60 kPa (intact) | *(Wang et al., 2006)* |
| Tensile test | Human | Tensile strength<br><br>Circumferential: 0.39 ± 0.07 MPa; decreases with age | *(Claes et al., 2010)* |
| Numerical simulation | 3D human heart model | Maximum stress<br><br>Right artery: 0.43 MPa<br>Left artery: 1 MPa | *(Grishina, Kirillova, and Glukhova, 2016)* |

| | | | |
|---|---|---|---|
| Tensile test | Human | Ultimate tensile strength<br><br>Circumferential: 1430 ± 604 kPa (adventitia); 446 ± 194 kPa (media); 394 ± 144 kPa (intima)<br>Longitudinal: 1399 ± 692 kPa (adventitia); 419 ± 188 kPa (media); 391 ± 144 kPa (intima) | *(Holzapfel et al., 2005)* |
| Equibiaxial tensile test | Human | Modulus<br><br>Longitudinal: 7.87 ± 3.39 kPa (low stress) and 97.3 ± 30.9 kPa (high stress)<br>Circumferential: 16.7 ± 19.3 kPa (low stress) and 89.9 ± 39.3 kPa (high stress) | *(Kural et al., 2012)* |
| Pressurised test | Porcine | Creep-strain: 0.05 ± 0.038 (mm/mm) | *(Veress et al., 2000)* |

### 2.4.3 Viscoelasticity

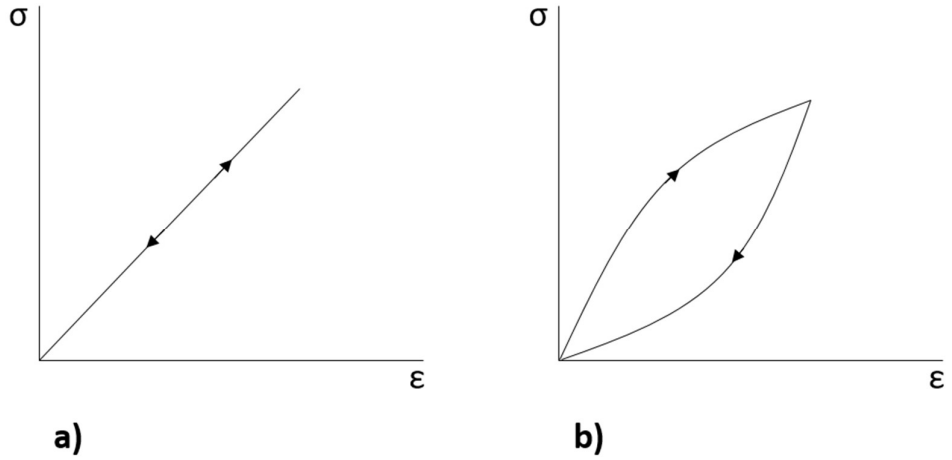


*Figure 2. 15 – Stress-strain curve showing loading and unloading of a (a) purely elastic material and (b) viscoelastic material. For the purely elastic material, loading and unloading the material results in no energy loss. For the viscoelastic material, the area inside the curve represents the energy lost.*

Most soft connective tissues are viscoelastic, including the coronary arterial walls (Gow and Taylor, 1968; Holzapfel, Gasser, and Stadler, 2002; Craiem and Armentano, 2006), exhibiting both elastic and viscous behaviour (figure 2. 15). Hence, the stress-strain

relationship is a function of the loading rate (Zhang, 2005). The elastic and viscous properties of a material can be characterised by storage and loss moduli (*E'* and *E"*, respectively), with the dynamic modulus (*E**) calculated as the complex number (figure 2. 16).

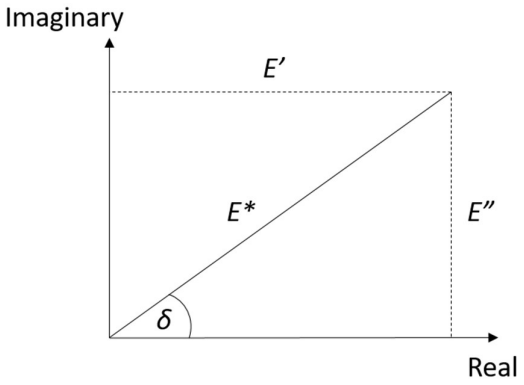


*Figure 2. 16 – Argand diagram of storage (E'), loss (E") and dynamic (E*) moduli, with phase lag (δ).*

In viscoelastic materials, stress relaxation measures the decrease in stress when the material is held at a given strain for a period of time (figure 2. 17), whereas creep measures the increase in strain when stress is held constant in the material (figure 2. 18). These methods provide an equilibrium modulus, allowing characterisation of the longer term effects on viscoelastic materials (Menard, 2008).

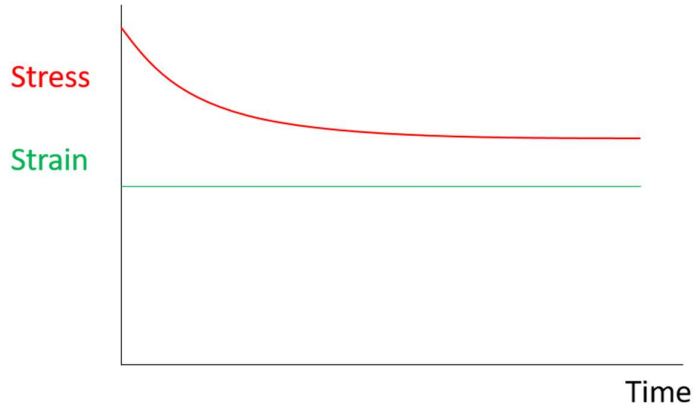


*Figure 2. 17 – Stress relaxation testing, with stress (red) and strain (green) against time.*

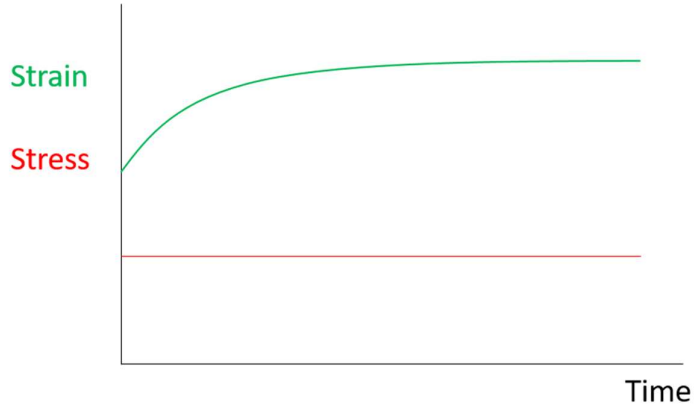


*Figure 2. 18 – Creep testing, with stress (red) and strain (green) against time.*

### 2.4.4 Viscoelastic properties of arteries

Changes in the viscoelastic properties of arteries are apparent in patients with vascular disease (Taniguchi et al., 2015). The viscoelastic properties of arteries which have been studied include hysteresis loops of a cross-sectional area as a function of pressure for large ovine arteries (Valdez-Jasso et al., 2009), creep and stress relaxation of porcine carotid arteries (Berglund, Nerem, and Sambanis, 2005), creep of human coronary arteries (Ozolanta

et al., 1998), and stress relaxation in the longitudinal and circumferential direction of porcine carotid arteries (García, Martínez, and Peña, 2012).

### 2.4.5 Dynamic mechanical analysis

At low rates of loading biological tissue can display different dynamic viscoelastic properties than when tested at physiological rates (Sadeghi, Espino, and Shepherd, 2015). The effect of dynamic viscoelastic properties can be measured using dynamic mechanical analysis (DMA), allowing characterisation of the short-term loading effects on viscoelastic materials at physiological relevant frequencies. This has not been previously quantified for coronary arteries. Replicating the physiological loading conditions is essential to understanding the mechanical behaviour of biological tissues subjected to dynamic environments, such as coronary arteries.

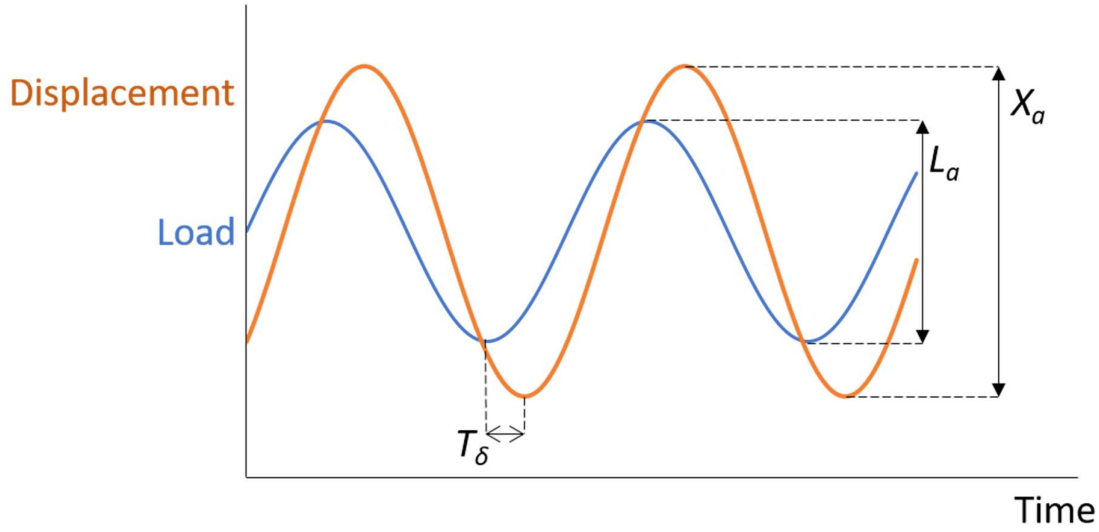


*Figure 2. 19 – Sinusoidal load input (blue) with displacement (orange) response, where $X_a$ is the displacement amplitude, $L_a$ the load amplitude, and $T_\delta$ the time lag between the two waveforms.*

Figure 2. 19 shows the displacement response of a viscoelastic material to a sinusoidal load input. The dynamic stiffness ($k^*$) is calculated from the load ($L_a$) and displacement ($X_a$) amplitudes (equation 2. 5). The phase lag (δ) is calculated using equation 2. 6, where ω is the angular frequency and $T_\delta$ the time lag between two waveforms. Using a shape factor, $E'$ and $E''$ can be calculated from $k^*$ and δ, which is described further in chapter 5.2.5.

*Equation 2. 5*

$$k^* = \frac{L_a}{X_a}$$

*Equation 2. 6*

$$\delta = \omega T_\delta$$

## 2.5 CONCLUSION

This chapter summarises the cardiovascular system and its associated disease, which is the leading cause of death worldwide. The most common medical interventions to treat cardiovascular disease, PCI and CABG, are presented. Characterisation of materials aids in the development of new biomaterials. Surface roughness measurements would provide quantitative data to analyse the surface of materials, and DMA would allow the dynamic viscoelasticity of a material to be measured.

# 3 SURFACE ROUGHNESS CHARACTERISATION OF LEFT ANTERIOR DESCENDING CORONARY ARTERIES

## 3.1 OUTLINE

Changes to blood vessels such as stenosis (narrowing of arteries), calcification or damage of the endothelial surface can be disruptive to the blood flow and lead to further clinical complications such as atherosclerosis, myocardial infarction and even death (Nabel and Braunwald, 2012; Bertazzo et al., 2013). The changes seen can indicate signs of disease of the arteries, such as atherosclerosis (Hansson, Libby, and Tabas, 2015). However, assessment of changes to the surfaces of vessels have been qualitative (Bertazzo et al., 2013). If stents or biomaterials are to be designed to mimic natural surfaces, for example, by nano-texturing through laser etching (Li et al., 2013) or electropolishing (Nazneen et al., 2012), or grafts designed to encourage endothelialisation (Buys et al., 2013; Yeh et al., 2006; Kakisis et al., 2005; Schmidt et al., 2012), then it is necessary to quantify the properties of the surface of healthy coronary arteries.

Surface roughness can be quantified using *Ra* (the arithmetic average of absolute values of sampling length), described in chapter 2.3.1. Although the application of *Ra* is mainly in tribology and wear (Eckold, Dearn, and Shepherd, 2015; Karpuschewski et al., 2015), it has recently been used to study biological tissues such as articular cartilage to assess its surface roughness (Ghosh et al., 2013; Peng and Wang, 2013). It has also been trialled for cardiovascular applications, not involving tribology. For example, red blood cells have been studied at a nano-scale using atomic force microscopy (AFM) (Antonio et al.,

2012), and average roughness values compared after treatment of cells through fixation and staining (Girasole et al., 2007). Further, the roughness of blood cells can be used as an indication of the health of cells, where red blood cells of diabetics appear smoother than cells from non-diabetics (Buys et al., 2013).

A common procedure when imaging biological tissue is to fix and dehydrate samples. This processing has the advantage of preventing degradation of tissue. A further benefit of the removal of water is preventing distortion of light due to water on the surface of samples during optical microscopy. Specifically, for scanning electron microscopy (SEM), a procedure employed in chapter 4 to enable multiscale analysis, an additional advantage of dehydration is that the specimen can be imaged under vacuum. Commonly, glutaraldehyde precedes the dehydration step to fix and prevent distortion of the specimen. The preparation of biological tissues for optical imaging typically requires various procedures, including freezing, fixation and dehydration. The effect of these procedures on certain physical characteristics of tissues are known, and can be accounted for, including changes in dimensions of the heart (Hołda et al., 2016) and biological tissue (Bucher et al., 2000), cancer volumes (Schned et al., 1996), and correcting cell density of endothelium (Doughty, 1995). Currently, however, it is unknown whether *Ra* might be altered by preparatory procedures used for soft connective tissues (such as coronary arteries).

The aim of this study was to characterise the surface roughness by the arithmetic mean deviation of roughness profile (*Ra*), for porcine left anterior descending (LAD) coronary arteries through optical microscopy. The variation of surface roughness was assessed along the length of the LAD artery. Furthermore, this study aimed to determine

whether freezing, fixation and dehydration, common procedures for preparing biological specimens for SEM, alter the measured *Ra.* Thus, *Ra* was measured before and after a freeze-thaw cycle, after fixation and after dehydration, and a suitable correction factor determined. For the work presented in this chapter, eight porcine hearts were used to initially characterise the surface roughness, and a further six hearts have been used for analysing the effects of processing.

## 3.2 METHOD

### 3.2.1 Porcine model

Porcine hearts were supplied by Fresh Tissue Supplies (Horsham, UK). Hearts were frozen on excision. No animals were sacrificed specifically for this study. Ethical approval was granted for this study by the University of Birmingham *Research Support Group* [ERN_15-0032]. After delivery to the laboratory, the hearts were wrapped individually in tissue paper soaked in Ringer's solution (Oxoid Ltd, Bassingstoke, UK). They were then stored in heat sealed bags at -40 °C, a protocol employed by other studies in the storage of porcine heart tissue (Espino et al., 2006; Millard et al., 2011; Espino et al., 2005; Espino, Shepherd, and Buchan, 2007).

### 3.2.2 Dissection

Hearts were defrosted at approximately 4 °C overnight before dissection. The LAD coronary artery was identified and dissected (figure 3. 1) from the most distal point visible to the bifurcation of the LAD and the left circumflex coronary artery (LCX) (figure 3.2). A

longitudinal incision (along the length of the artery) was made along the LAD sample to expose its internal surface (figure 3. 3). Excess cardiac muscle tissue was removed from samples leaving coronary artery tissue only (figure 3. 3). This was important for future experiments where the viscoelastic properties of the arteries were measured, when myocardium attached to the arteries would affect the values calculated (chapter 5). Additionally, specimens were imaged after processing, involving fixation, where for effective fixation of biological tissue the thickness of tissue samples should be less than 2-3 mm (Beck, 1998). Finally, the sample was sectioned into three specimens of 20 mm each. These tissue samples were categorised as proximal, middle and distal where in this case proximal refers to a position nearer the base of the heart and distal near to the apex of the heart, along a longitudinal axis of the LAD (figure 3. 3). Dimensions of the specimens were measured along its length ($L$), width at top and bottom ($W_1$ and $W_2$), and thickness ($t$) using a Vernier caliper, taking the mean of 3 values for each dimension (figure 3. 4).

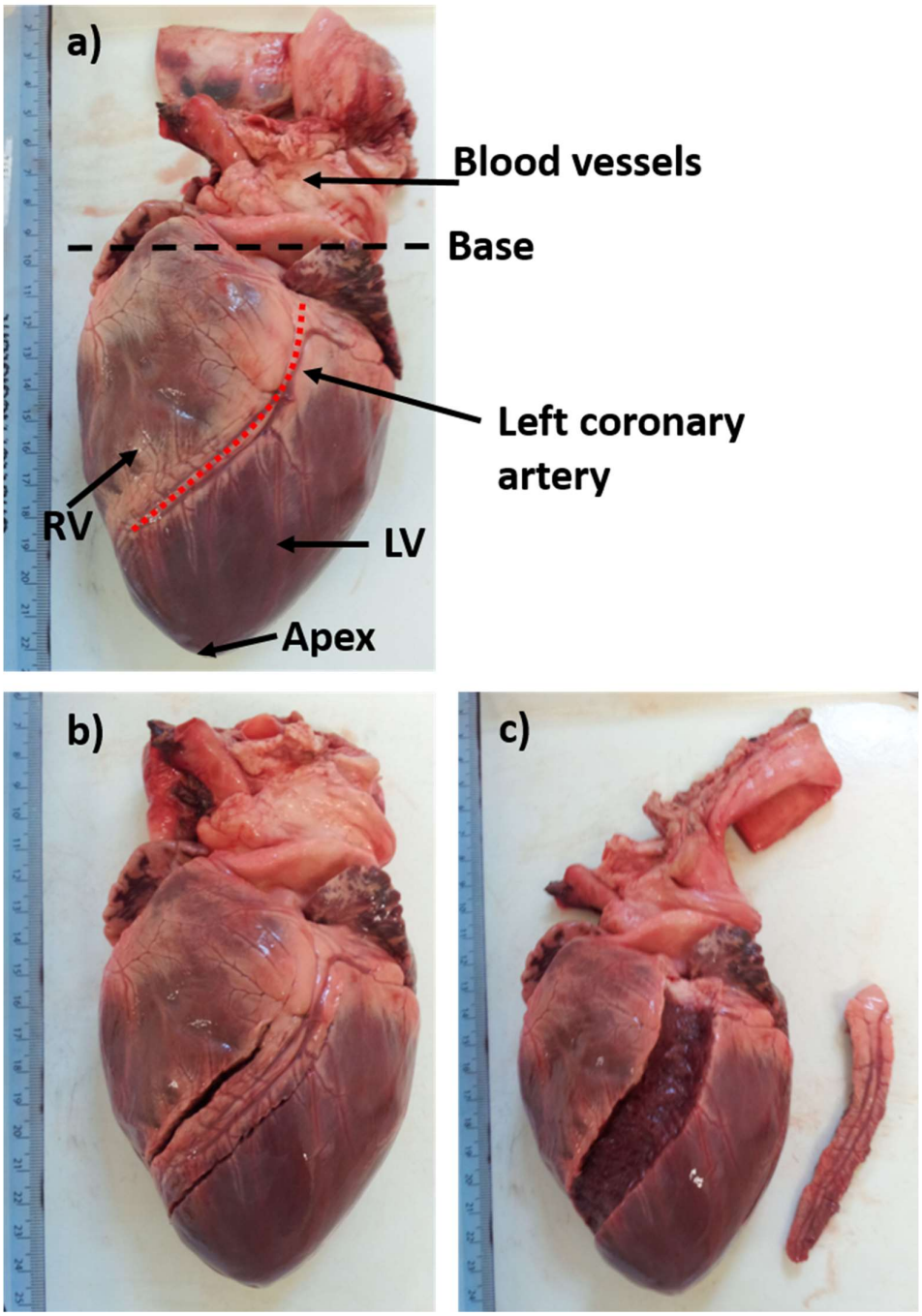


*Figure 3. 1 – Stages of coronary artery dissection, with: (a) defrosted heart pre- dissection, with apex, base, blood vessels, RV (right ventricle), LV (left ventricle) and left coronary artery identified; (b) LAD coronary artery identified and dissection commenced from most distal point visible of LAD, and (c) LAD removed to the bifurcation with LCX, still attached to myocardium.*

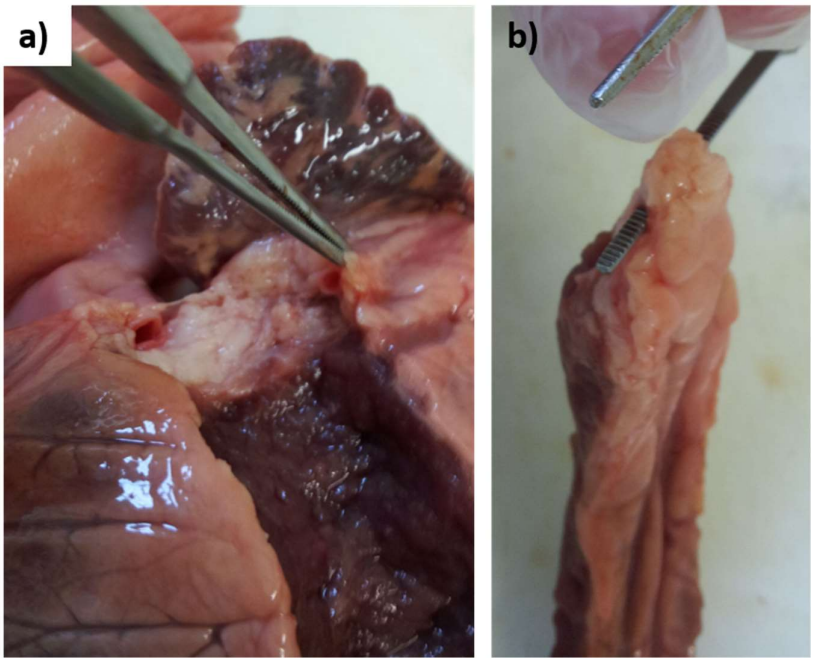


*Figure 3. 2 – Dissection procedure identifying defined top of LAD, a) tweezer point identifying the LCX, b) tweezers positioned through LCX and emerging at the defined top of LAD.*

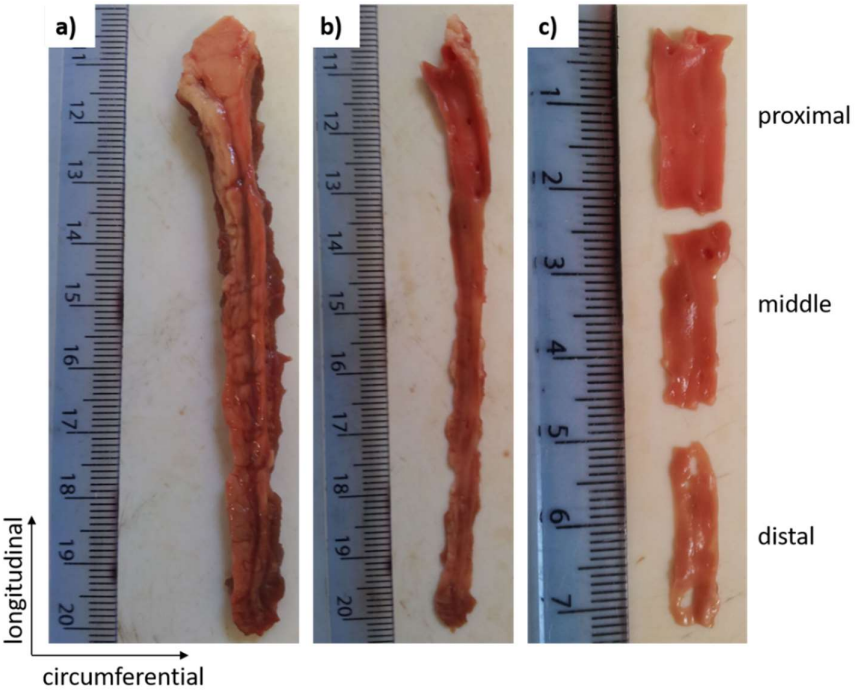


*Figure 3. 3 – LAD dissected tissue with longitudinal and circumferential axes labelled; a) LAD connected to myocardium; b) myocardium removed and LAD opened longitudinally; c) LAD specimens prepared as 20 mm sections starting at the defined top point at the bifurcation of LCX, with proximal, middle and distal sections identified.*

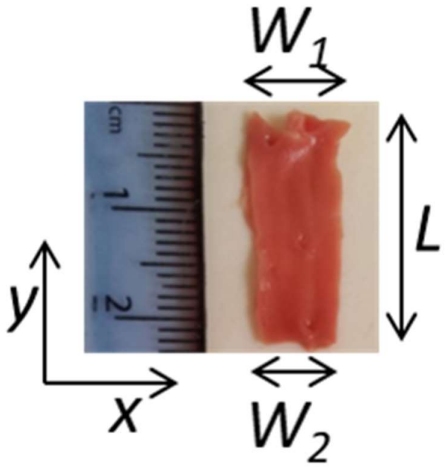


*Figure 3. 4* - Length (*L*) and sample width ($W_1$ and $W_2$) of medial LAD coronary artery specimens used in this study. Note, thickness (*t*) was measured perpendicular to the *x*-*y* plane, in the *z* plane.

Tissue samples were wrapped in tissue paper soaked in Ringer's solution (Oxoid Ltd, Bassingstoke, UK) and stored in heat sealed bags at -40 °C until required for microscopy. Before further testing, tissue samples were defrosted at 4 °C for an hour, following protocols from previous studies of porcine heart tissue (Millard et al., 2011; Espino, Shepherd, and Buchan, 2007; Espino et al., 2006; Espino et al., 2005).

### 3.2.3 Optical microscopy

An optical focus variation microscope (G4 Infinite Focus, Alicona UK, Kent, UK), as seen in figure 3. 5, was used to image the surface of the specimens at 10× magnification (10× Nikon CFI 60 TU Plan Epi Infinity Corrected Obj lens, Alicona UK, Kent, UK). This was chosen as an appropriate magnification as the minimum measurable *Ra* of the 10× magnification for the microscope was optimum for the range of measured *Ra* data during preliminary testing (Alicona, 2014). Scanning was performed between the maximum and minimum focussing positions of the height of each sample in the *z* plane (figure 3. 4) through focussing of the

lens. Similarly, the area of the scan was controlled by selecting the maximum and minimum *x* and *y* positions of the sample. Note, the *x* and *y* axes are parallel to the circumferential and longitudinal directions, respectively (figure 3. 3), and the *z* axis is perpendicular to the *x*-*y* plane (i.e. aligned parallel to the direction of the thickness of the sample). The Alicona Infinite Focus microscope is a non-contact, optical, three-dimensional (3D) measurement system. Lighting was controlled via white light emitting diode coaxial illumination. Illumination intensity, and lateral (*x* and *y* axis) and vertical (*z* axis) resolution were adjusted using automated ideal settings, as defined using the instruments' software, Alicona IF-Measure Suite (version 5.1, Alicona UK, Kent, UK), consistent with previous studies (Hiersemenzel et al., 2012). The Alicona software was used to obtain and analyse all images. Imaging was performed at four stages in this study (figure 3. 7): before and after a freeze-thaw cycle; following fixation; and following dehydration.


*Figure 3. 5 – G5 Alicona Infinite Focus optical microscope.*

A 3D reconstruction of the image was performed using the Alicona IF-Laboratory Measurement Module (version 6.1, Alicona UK, Kent, UK), from which the Ra was measured. The Alicona IF-Laboratory Measurement Module (version 6.1, Alicona UK, Kent, UK) generates a 3D point cloud by using contrast based focus detection and focus stacking to calculate the depth of microscopy images. This method has been shown to be comparable to traditional methods, such as scanning electron microscopy, for measuring surface roughness (Schroettner, Schmied, and Scherer, 2006). The 3D point cloud represented as a

reconstructed surface is shown in figure 3. 11. The entire surface of each sample was imaged and reconstructed. Subsequently, five profile lengths with a mean of 2.63 ± 0.67 mm were measured along two directions aligned with circumferential and longitudinal sample orientations. The *Ra* was assessed both longitudinally and circumferentially. When measuring *Ra* profiles, bifurcations where smaller vessels connected to the LAD were avoided during profile selection, highlighted in figure 3. 6. They were avoided because they formed part of the blood vessel structure rather than being an intrinsic property of the surface. Also, profiles were not measured near the edges of the sample where distortion may have occurred during dissection (figure 3. 6). Equations 3. 1 and 3. 2 (ISO 4287, 2009) were used to calculate surface roughness in the circumferential direction, $Ra_C$, and the longitudinal direction, $Ra_L$, respectively. Where $Z(x)$ is the profile height function along $x$ (equation 3. 1), $Z(y)$ is profile height function along $y$ (equation 3. 2), and $l$ is the sampled length. The mean surface roughness for each individual specimen was determined from five repeat measurements taken in each direction.

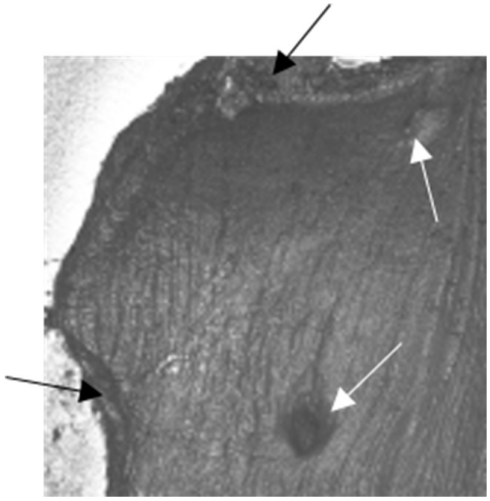

*Figure 3. 6 – Preliminary sample at 5× magnification, highlighting areas that were avoided for profile selection. White arrows – bifurcations. Black arrows – edge of sample where damage is visible due to dissection. Image is 3.246 × 3.246 mm.*

*Equation 3. 1*

$$Ra_C = \frac{1}{l}\int_0^l |Z(x)|\,dx$$

*Equation 3. 2*

$$Ra_L = \frac{1}{l}\int_0^l |Z(y)|\,dy$$

### 3.2.4 Tissue processing

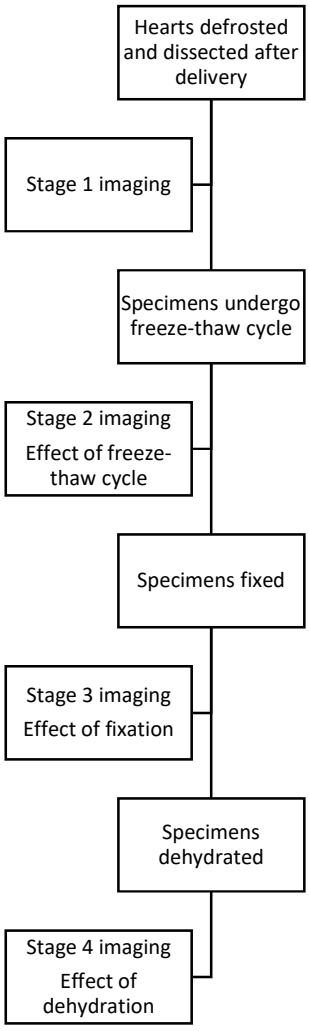


*Figure 3. 7 – Flow chart for processing and imaging stages of LAD coronary artery specimens of porcine hearts, frozen immediately after excision. For general Ra results, 8 porcine hearts were dissected resulting in 24 specimens (8 proximal, 8 middle and 8 distal). When investigating the effects of processing, 6 porcine hearts were dissected and 6 specimens investigated (6 middle).*

Tissue samples underwent fixation and dehydration, following a standard protocol for soft mammalian tissues (Beck, 1998) (table 3. 1). Specimens were immersed in a 3% glutaraldehyde solution (Fluka Analytical, Sigma Aldrich, St Louis, MO, USA) with 0.2 M sodium phosphate buffer for 1 hour, at an average pH value for animal tissue of pH 7.4 (Hayat, 1981) (table 3. 2). Subsequently, specimens were rinsed in three 10 minute washes of phosphate buffer saline (PBS) solution to remove any remaining glutaraldehyde. To ensure that the samples remained hydrated they were stored in PBS solution at 4 °C until dehydration.

*Table 3. 1 – Protocol for processing tissue, including fixation and dehydration.*

| **Process** | **Solution** | **Time** |
|---|---|---|
| Fixation | 3% glutaraldehyde solution | 1 hour |
| 3 × wash | PBS | 3 × 15 minutes |
| 6 × stages of dehydration sequence | 30%, 50%, 70%, 95% and 2 × 100% ethanol | 6 × 10 minutes |
| Complete dehydration | Hexamethyldisilasane | 15 minutes, then leave overnight |

*Table 3. 1 – Buffer and fixative preparation protocols.*

| Buffer/fixative | Total volume | Solutes/Solutions | Supplier | Amount | Preparation |
|---|---|---|---|---|---|
| $NaH_2PO_4 \bullet H_2O$ aq. | 1000 ml | $NaH_2PO_4 \bullet H_2O$ | Sigma Aldrich, St Louis, MO, USA | 27.6 g | Dissolve in distilled water and adjust to 1000 ml |
| $Na_2HPO_4 \bullet 2H_2O$ aq. | 1000 ml | $Na_2HPO_4 \bullet 2H_2O$ | Sigma Aldrich, St Louis, MO, USA | 35.61 g | Dissolve in distilled water and adjust to 1000 ml |
| Sodium phosphate buffer solution (0.2 M) | 100 ml | $NaH_2PO_4 \bullet H_2O$ aq. | | 23 ml | Add solutions and adjust to pH 7.3 |
| | | $Na_2HPO_4 \bullet 2H_2O$ aq. | | 77 ml | |
| 3% glutaraldehyde | 100 ml | Glutaraldehyde (50%) | Fluka Analytical, Sigma Aldrich, St Louis, MO, USA | 6 ml | Add solutions |
| | | Sodium phosphate buffer solution (0.2 M) | | 94 ml | |

Dehydration was performed in washes of 10 minutes with increasing concentrations of ethanol (Fisher Chemical, Fisher Scientific UK Ltd, Loughborough, UK) at 30%, 50%, 70%, 95% and two washes at 100%. The concentration series ensures that dehydration occurs in a controlled manner, minimising distortion of the specimen (Bucher et al., 2000). Finally, hexamethyldisilasane (HMDS; Aldrich Chemistry, St Louis, MO, USA) was used to complete dehydration (Moran and Coats, 2012), removing any remaining ethanol from the specimen by displacement. The specimen underwent a wash of HMDS for 15 minutes before replenishing with fresh HMDS to be left overnight to evaporate.

### 3.2.5 Correction Factor

A linear correction factor was calculated for *Ra* when a significant difference was identified following processing. *α* was calculated as the change in *Ra* due to processing over the original *Ra* value before processing using equation 3. 3, where $Ra_{\text{pre}}$ and $Ra_{post}$ were the mean values of *Ra* before and after processing respectively.

*Equation 3. 3*

$$\alpha = \frac{Ra_{pre} - Ra_{post}}{Ra_{pre}}$$

*Equation 3. 4*

$$Ra_{pre} = \frac{Ra_{post}}{(1 - \alpha)}$$

By rearranging equation 3. 3 (through equation 3. 4), an equation for corrected surface roughness ($Ra_{\theta}$) is presented in equation 3. 5. Here, *Ra* is the uncorrected, dehydrated surface roughness ($Ra_{post}$). This uses a linear relationship between change in

surface roughness and original surface roughness during processing (section 3.3.4), thus when rearranging equation 3. 3, $Ra_{\beta}$ is assumed as $Ra_{pre}$.

*Equation 3. 5*

$$Ra_{\beta} = \frac{Ra}{1 - \alpha}$$

An additional method to normalise *Ra* was considered from the relationship between change in tissue dimension and *Ra* (equation 3. 7), where $D_{pre}$ and $D_{post}$ are the mean dimension values pre- (stage 1) and post- (stage 4) processing.

*Equation 3. 6*

$$Ra_{\beta} = Ra \frac{D_{pre}}{D_{post}}$$

### 3.2.6 Data analysis

When presenting results, *N* refers to the number of hearts, and where appropriate the number used for calculating confidence intervals. Whereas *n* indicates the number of specimens measured.

All statistical analysis was performed using Minitab Statistical Software (Minitab 17.0, Minitab Inc, State College, PA, USA). Data sets were assessed for normal distribution using a Shapiro-Wilk normality test, and homogeneity of variance ensured using Levene's test. If data sets were normally distributed (i.e. $p > 0.05$) and variance was equal across groups ($p > 0.05$), significance was assessed ($p < 0.05$) using a paired *t-test*. If data was not normally distributed, a Wilcoxon Signed Rank test was used (i.e. a paired non-parametric test; $p < 0.05$

for significance) [57, 58]. For these results, 8 individual hearts were dissected ($N$ = 8), giving a total of $n$ = 24 specimens (8 of each for proximal, middle and distal sections).

For the remainder of results assessing a freeze-thaw cycle, effect of processing, and calculation of a correction factor, a total of 6 hearts were dissected ($N$ = 6), of which the middle specimens were investigated only ($n$ = 6). To assess the effect of a freeze cycle (figure 3. 7; stages 1 and 2) on surface roughness and physical dimensions on coronary arteries, a student paired *t-test* ($p < 0.05$) was performed for each dependent variable ($Ra_C$, $Ra_L$, $L$, $W_1$ and $W_2$) (Bland, 2000).

A one-way repeated measures multivariance analysis of variance (MANOVA) test was performed to analyse processing of coronary arteries, and to assess whether there was a significant difference in surface roughness and physical dimensions of the tissue (Bland, 2000; Reilly, 2015). Multiple dependent variables ($Ra_C$, $Ra_L$, $L$, $W_1$ and $W_2$) were compared during three independent stages (figure 3. 7; stages 1, 3 and 4), with the risk of type 1 errors reduced due to the choice of MANOVA (Bock, 1975). If a statistical significance was identified ($p < 0.05$) using a MANOVA test, analysis of variance (ANOVA) was then performed on each dependent variable using Tukey's method ($p < 0.05$) to determine which stage of the independent variable resulted in this change.

When a correction factor (equation 3. 5) was applied to results, a student paired *t-test* was performed between the calculated and actual results to determine if there was a significant difference ($p < 0.05$).

## 3.3 RESULTS

### 3.3.1 Circumferential vs longitudinal

LAD arteries were significantly rougher along their circumference than along their longitudinal alignment ($Ra_C > Ra_L$; $p < 0.05$, table 3. 3). This was the case for proximal, medial and distal samples along the LAD artery (table 3. 3). $Ra_C$ ranged from 0.73 to 2.83 µm, and $Ra_L$ ranged from 0.35 to 0.92 µm, with individual results presented in figure 3. 9. Ridges were observed along the circumferential direction of the LAD artery, but not longitudinally (figure 3. 10), consistent with the higher $Ra_C$ values compared to $Ra_L$. Sample *Ra* profiles aligned circumferentially and longitudinally along the LAD coronary artery are provided in figure 3. 8.

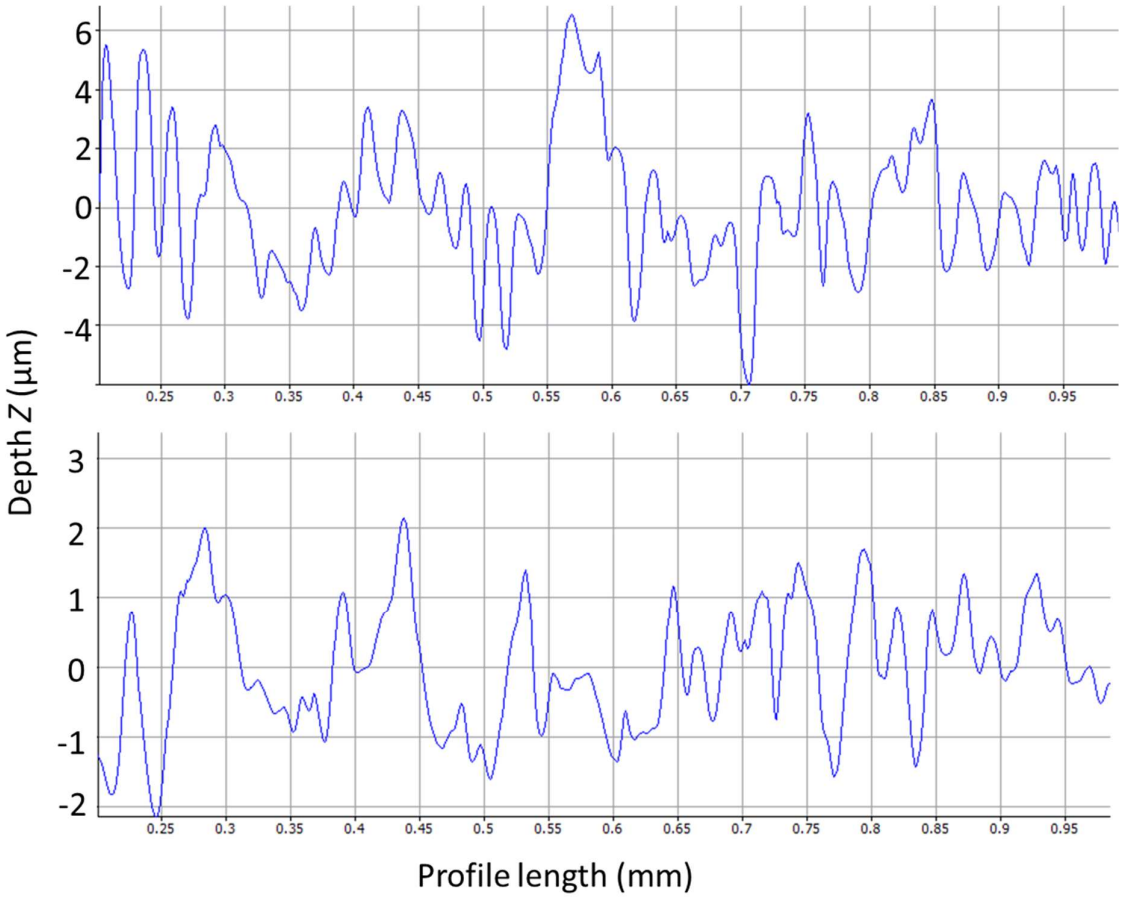


*Figure 3. 8 - Sample surface roughness measurements for (top) $Ra_C$ and (bottom) $Ra_L$.*

### 3.3.2 Variation along LAD artery

No statistical difference was found in the variation of circumferential roughness of $Ra_C$ along the length of the artery (proximal vs distal, $p > 0.05$; figure 3. 10). This was also the case for $Ra_L$ (figure 3. 10). Although $Ra_C$ of the proximal samples had a higher mean value compared to that of the middle and distal samples (table 3. 3), the spread of results was greater, resulting in a larger standard deviation ($Ra_C$ mean ± standard deviation: proximal = 2.07 ± 0.92 µm; middle = 1.53 ± 0.50 µm, distal = 1.48 ± 0.77 µm). This supports the finding of no statistical difference between the results.

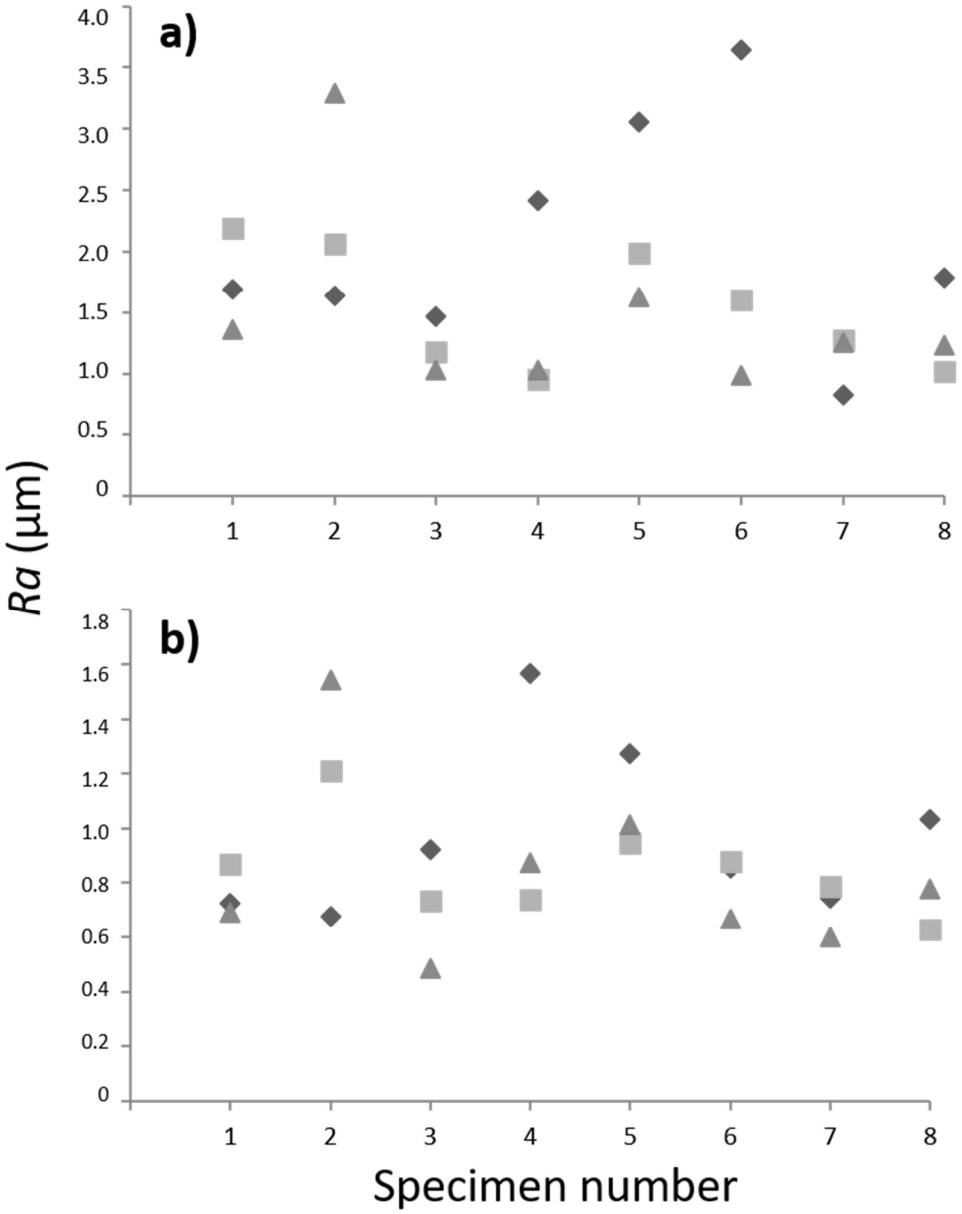


*Figure 3. 9 – Individual specimen mean results for (a) $Ra_C$ and (b) $Ra_L$, at proximal (diamond), middle (square) and distal (triangle) positions.*

*Table 3. 3 – Descriptive statistics of surface roughness for $Ra_C$ and $Ra_L$. N = 8, n = 24 (proximal n = 8; middle n = 8; distal n = 8).*

| Position | Normally distributed? | Mean (µm) $Ra_C$ | Median (µm) $Ra_C$ | SD (µm) $Ra_C$ | Mean (µm) $Ra_L$ | Median (µm) $Ra_L$ | SD (µm) $Ra_L$ |
|---|---|---|---|---|---|---|---|
| Proximal | Yes | 2.07 | 1.74 | 0.92 | 0.97 | 0.89 | 0.31 |
| Middle | Yes | 1.53 | 1.44 | 0.50 | 0.85 | 0.83 | 0.18 |
| Distal | No | 1.48 | 1.24 | 0.77 | 0.83 | 0.73 | 0.33 |

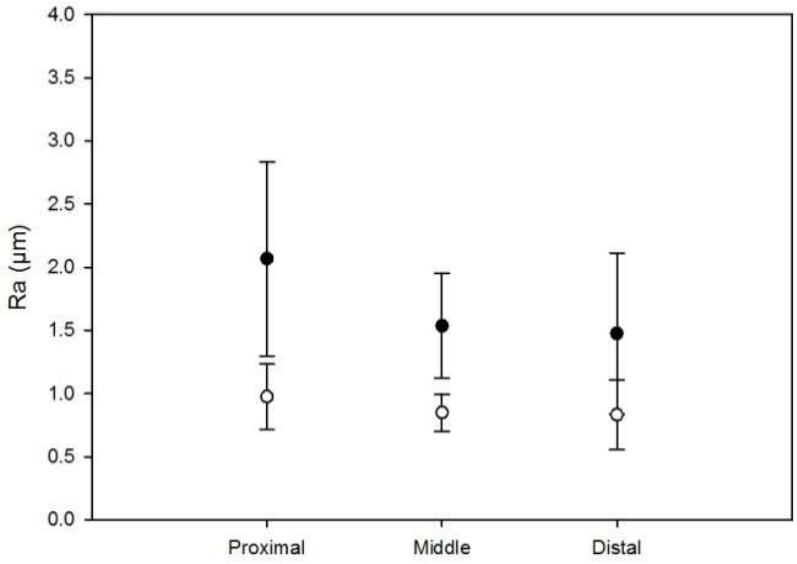


*Figure 3. 10 – Mean surface roughness (Ra) of the proximal, middle and distal LAD coronary artery. White dots for $Ra_L$ and black dots for $Ra_C$. Error bars represent 95% confidence intervals where N = 8.*

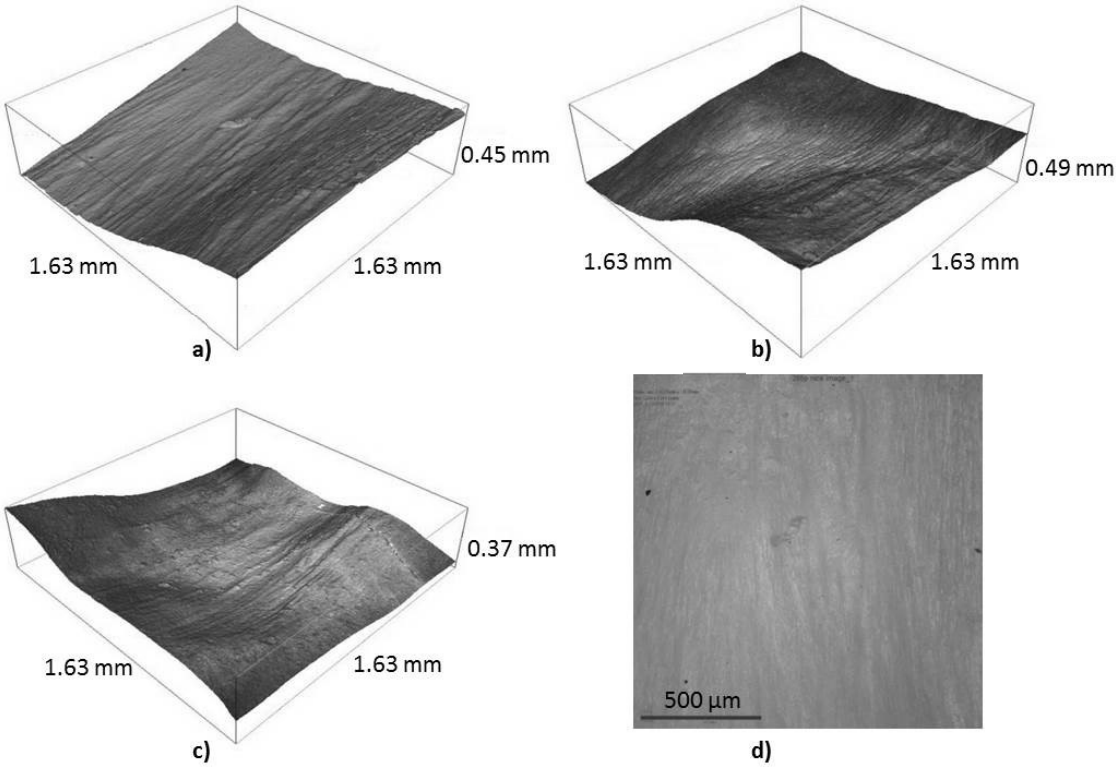


*Figure 3. 11 – 3D reconstruction of the endothelial surface of the LAD (10×). Ridges are observable across the circumferential direction (grooves appearing in longitudinal direction). Reconstructed surfaces at a) proximal, b) middle and c) distal positions, and d) optical two-dimensional (2D) image of a proximal specimen.*

### 3.3.3 Effect of preparing LAD artery

Figure 3. 12 shows the 3D reconstructed surface at each stage of processing, with the respective optical images shown in figure 3. 13. These figures highlight the increased surface roughness in the circumferential rather than longitudinal direction, with ridges visible. Individual specimen results for each stage are shown in figure 3. 14 for both $Ra_C$ and $Ra_L$.

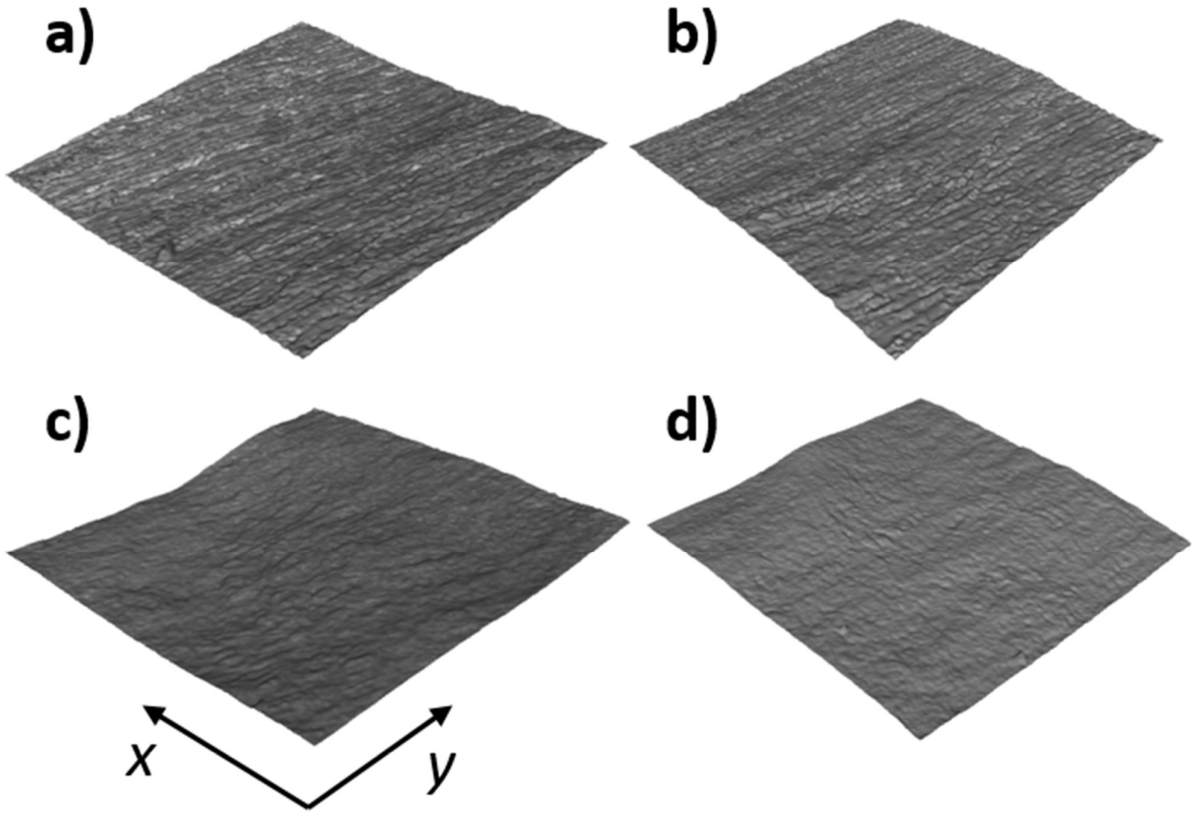


*Figure 3. 12 – 3D reconstruction of imaged samples (a) in their initial state (stage 1), and following (b) a subsequent freeze-thaw cycle (stage 2), (c) glutaraldehyde fixation (stage 3), and (d) a final dehydration stage (stage 4). Dimensions of all specimens in the x and y axes are 1.6 mm × 1.6 mm.*

$Ra_C$ values ranged from 0.82 to 2.26 µm. Figure 3. 12 shows the surface at each stage of processing, where ridges can be seen along the longitudinal direction (*y* axis). Freezing (1.28 ± 0.34 µm), fixation (1.49 ± 0.49 µm) and dehydration (1.98 ± 0.26 µm), independently, did not significantly alter $Ra_C$ ($p > 0.05$; table 3. 4) from one stage of tissue preparation to the next. However, the cumulative effect of fixation and dehydration during the preparation stages led to a significant increase in $Ra_C$ from 1.36 ± 0.27 µm (the initial surface roughness) to 1.98 ± 0.26 µm ($p < 0.05$; table 3. 4) following all tissue preparation (figure 3. 15).

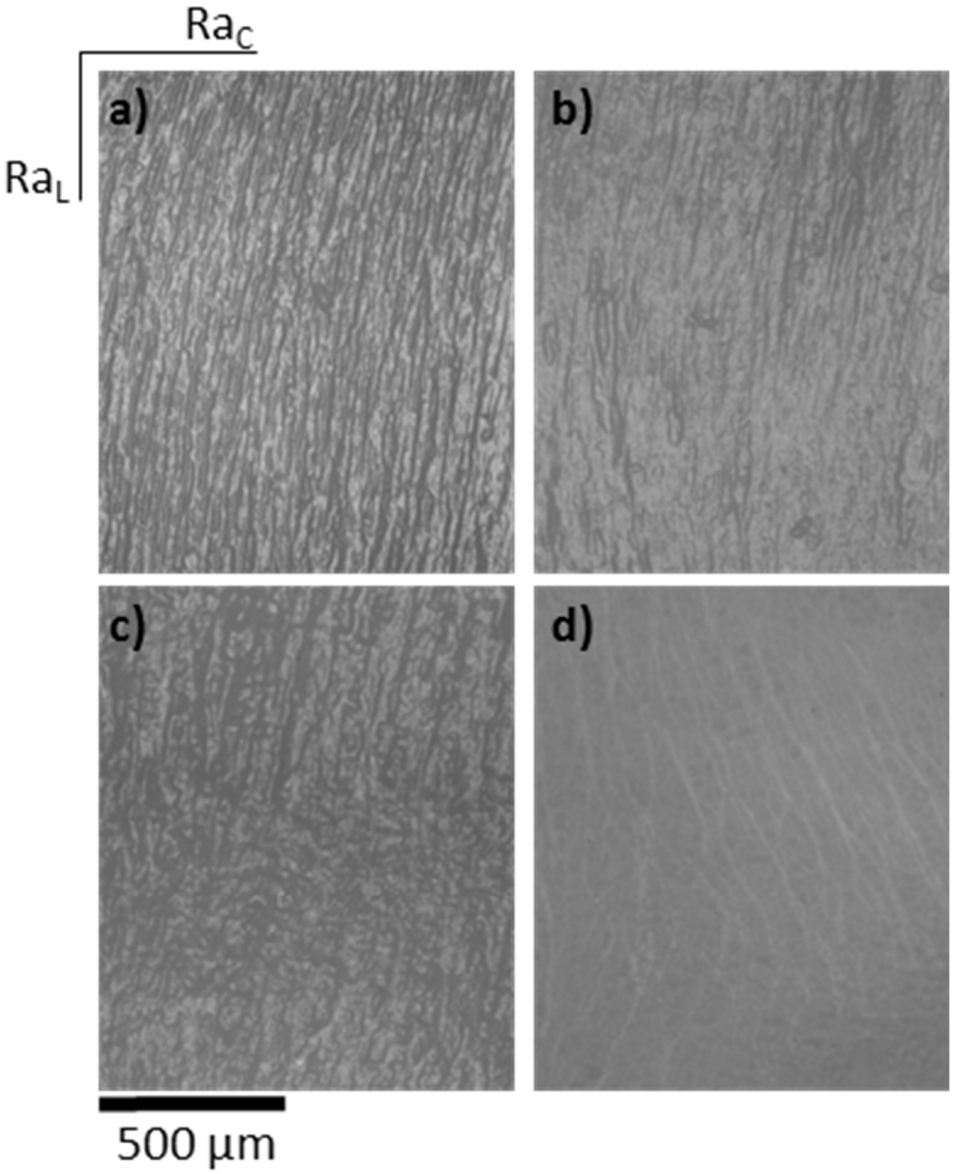


*Figure 3. 13 - Optical image of the LAD coronary artery surface (a) at their original state (stage 1), and following a subsequent (b) freeze-thaw cycle (stage 2), (c) glutaraldehyde fixation (stage 3), and (d) a final dehydration stage (stage 4). Axes along which $Ra_C$ and $Ra_L$ measurements were taken are shown.*

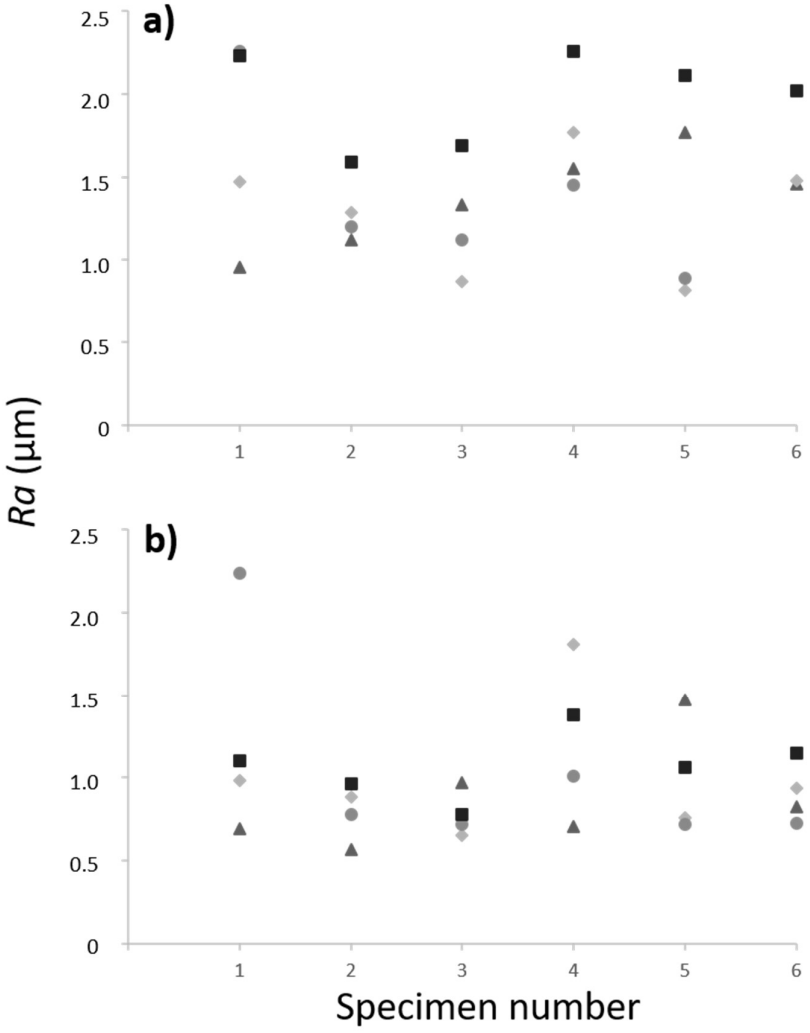


*Figure 3. 14 – Individual specimen mean values for (a) $Ra_C$ and (b) $Ra_L$, at stage 1 (triangle), stage 2 (diamond), stage 3 (circle) and stage 4 (square).*

*Table 3. 4 – Surface roughness and dimensions (mean, median and standard deviation, SD) of samples at their original state (stage 1), and following a subsequent freeze-thaw cycle (stage 2), glutaraldehyde based fixation (stage 3) and a final dehydration stage (stage 4). Measurements were obtained from six independent specimens (N = 6). Where † indicates a significant difference for stage 4 as compared to stages 1 and 2, and ‡ indicates a significant difference at stage 4 as compared to stage 3 ($p < 0.05$) Note, $Ra_{c\theta}$ is the correction following the cumulative processes up to stage 4, for $Ra_c$.*

| | --- Stage 1 --- | | | --- Stage 2 --- | | | --- Stage 3 --- | | | --- Stage 4 --- | | |
|---|---|---|---|---|---|---|---|---|---|---|---|---|
| | **Mean** | **Median** | **SD** | **Mean** | **Median** | **SD** | **Mean** | **Median** | **SD** | **Mean** | **Median** | **SD** |
| $Ra_C$ (µm) | 1.36 | 1.40 | 0.27 | 1.28 | 1.38 | 0.34 | 1.49 | 1.33 | 0.49 | 1.98† | 2.07 | 0.26 |
| $Ra_L$ (µm) | 0.87 | 0.76 | 0.30 | 1.00 | 0.91 | 0.38 | 1.03 | 0.75 | 0.55 | 1.07 | 1.08 | 0.18 |
| $L$ (cm) | 1.98 | 1.98 | 0.11 | 1.91 | 1.95 | 0.16 | 1.83 | 1.82 | 0.13 | 1.56†‡ | 1.56 | 0.14 |
| $W_1$ (cm) | 0.71 | 0.69 | 0.07 | 0.67 | 0.67 | 0.02 | 0.62 | 0.62 | 0.05 | 0.55† | 0.52 | 0.08 |
| $W_2$ (cm) | 0.58 | 0.57 | 0.08 | 0.57 | 0.58 | 0.06 | 0.53 | 0.55 | 0.06 | 0.43† | 0.45 | 0.06 |
| $t$ (cm) | 0.04 | 0.04 | 0.01 | 0.03 | 0.03 | 0.01 | 0.04 | 0.04 | 0.01 | 0.04 | 0.04 | 0.01 |
| $Ra_{c\theta}$ (µm) | 1.31 | 1.42 | 0.21 | | | | | | | | | |

$Ra_L$ measurements ranged from 0.57 to 2.24 µm. Freezing (1.00 ± 0.38 µm), fixation (1.03 ± 0.55 µm) and dehydration (1.07 ± 0.18 µm), independently, did not significantly alter $Ra_L$ ($p > 0.05$; table 3. 4; figure 3. 15). There was no significant difference in the initial $Ra_L$ (0.87 ± 0.30 µm) and that measured following the cumulative effect of freezing, fixation and dehydration (1.07 ± 0.18 µm; $p > 0.05$; table 3. 4; figure 3. 15).

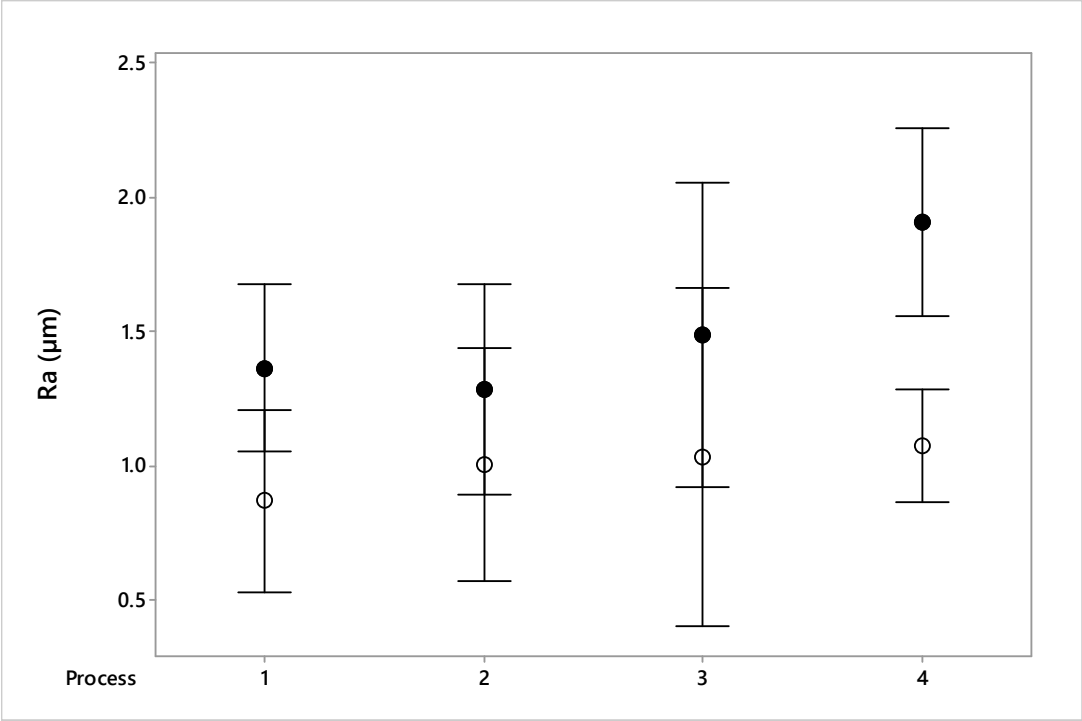


*Figure 3. 15 – Surface roughness mean with 95% confidence intervals (N = 6) at various processing stages ($Ra_C$ – black; $Ra_L$ – white), where process 1 = original, 2 = post-freeze; 3 = post-fixation; 4 = post-dehydration (see figure 3. 7).*

### 3.3.4 Correction Factor

$Ra_C$ significantly increased following processing, thus a correction factor was applied. A linear relationship was assumed, as ultimately the goal of the correction factor was to provide a standard number that could be used to predict the surface roughness values before processing. The correction factor, $\alpha$, calculated using equation 3. 3 as -0.46, was inserted into equation 3. 5 to calculate $Ra_{C\beta}$, the corrected surface roughness in the circumferential direction, as shown in equation 3. 7.

*Equation 3. 7*

$$Ra_{C\beta} = \frac{Ra_C}{1.46}$$

The mean $Ra_{C\beta}$ was 1.31 ± 0.21 µm. No significant difference was found between the original $Ra_C$ values and the calculated $Ra_{C\beta}$ values ($p > 0.05$; table 3. 4). Figure 3. 16 shows the individual mean specimen results for $Ra_{C\beta}$ compared to its corresponding stage 1 $Ra_C$, in addition to the stage 4 results that each point was calculated from.

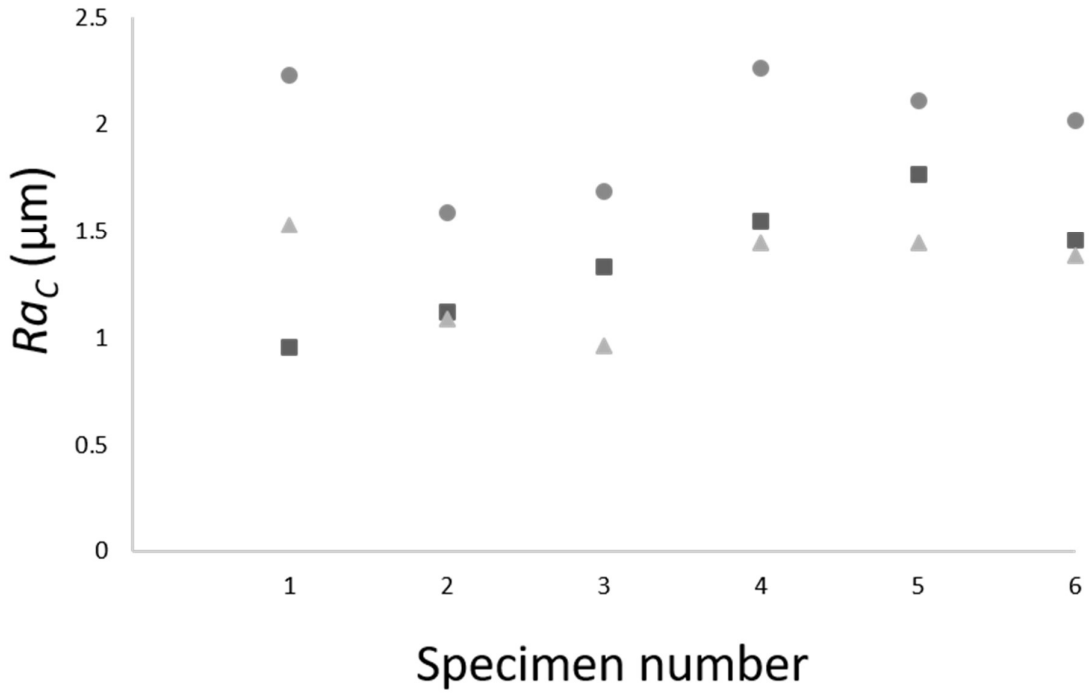


*Figure 3. 16 – Individual specimen mean values for $Ra_C$, with stage 4 (circle), stage 1 (square) and corrected $Ra_{C\beta}$ (triangle).*

### 3.3.5 Tissue Dimensions

Freezing did not significantly alter any of the physical dimensions ($p > 0.05$; table 3. 4); the physical dimensions of tissue, though, were significantly altered due to the cumulative effect of processing ($p < 0.01$; table 3. 4). The initial length of specimens (1.98 ± 0.11 cm) was not significantly different to the fixed specimen lengths (1.83 ± 0.13 cm, $p >$ 0.05), but they were significantly greater than the dehydrated specimen lengths (1.56 ± 0.44

cm, $p$ = 0.001; table 3. 4). The fixed lengths were also significantly greater than the dehydrated lengths ($p < 0.05$; table 3. 4).

The initial width at $W_1$ and $W_2$ (0.71 ± 0.07 and 0.58 ± 0.08 cm, respectively) were significantly greater than the widths after processing (0.55 ± 0.08 and 0.43 ± 0.06 cm, $W_1$ and $W_2$ respectively, $p < 0.05$; table 3. 4). However, the individual stages of fixation (0.62 ± 0.05 and 0.53 ± 0.06 cm, $W_1$ and $W_2$ respectively) and dehydration caused no significant differences to the width measurements ($p > 0.05$; table 3. 4). The thickness of specimens ranged from 0.02 to 0.05 cm. No significant difference was seen in thickness due to the processing stages ($p > 0.05$; table 3. 4).

An additional relationship was evaluated between the decrease in width due to processing and the increase in $Ra_C$, as a significant difference was noted in $Ra_C$ but not $Ra_L$ due to processing. The value of $W_1$ and $W_2$ were averaged for before (stage 1) and after (stage 4) processing, with $W$ post-processing found to be 75% of the pre-processing value. This is an inverse relationship to $Ra$ due to processing. Using equation 3. 7, $Ra_{C\theta}$ was calculated, however the percentage error when compared to $Ra_c$ pre-processing varied from -21 to 76%.

## 3.4 Discussion

### 3.4.1 Key findings

For the first time, surface roughness was quantitatively measured for LAD coronary arteries. Surface roughness was characterised circumferentially and longitudinally, and was

significantly greater in the circumferential direction. Surface roughness did not vary along the length of the sample. Processing of tissue through fixation and dehydration increased the circumferential surface roughness but did not alter surface roughness longitudinally. Thus, the effect of processing was evaluated with a correction factor in the circumferential direction to calculate surface roughness before processing from dehydrated specimens. The technique proposed in this chapter could be used to evaluate the surface roughness of other biological tissue, and a similar correction factor could be calculated to understand the effect of different fixatives and dehydration protocols.

### 3.4.2 Surface roughness

Surface roughness of coronary arteries has not previously been quantified, however, *Ra* has been measured for other biological specimens, such as articular cartilage (Ghosh et al., 2013). Both the cartilage and endothelium have low frictional requirements. Cartilage values measured by Ghosh et al. (2013), varying from 165 nm to 174 nm using scanning electron microscopy, and 82.6 nm to 114.4 nm using AFM, are lower than the values measured in this study. However, surface roughness measurements can vary between techniques used, as noted by Ghosh et al. (2013). For example, other studies of articular cartilage found its surface roughness to range from 800 nm using laser profilometry, up to 1600 nm using stylus profilometry (Forster and Fisher, 1999). Therefore, it would be of value to assess the surface roughness of coronary arteries with a multiscale analysis, using higher magnification techniques such as SEM. Such values are comparable to the average mean of all measurements of 0.89 µm (longitudinal) and 1.04 µm (circumferential) in the first part of this chapter (section 3.3.1). Of course, there is no reason for articular cartilage and blood

vessels to have comparable surface roughness beyond both needing to be fairly smooth. However, no values are available for coronary arteries for comparison. Furthermore, it provides a comparison for another smoothed surface connective tissue, demonstrating a credible range for a biological material.

When measuring $Ra_L$, the line along which the surface roughness was measured does not run perfectly parallel to the direction of the ridges. Muscle and fibrous elements orientate helically along the length of the arteries (Learoyd and Taylor, 1966) and a more helical layout within blood vessels was noted with ridges on the surface of LAD coronary arteries in this study. These could be related to the spiral flow seen in other studies (Stonebridge and Brophy, 1991; Morbiducci et al., 2009). Therefore, $Ra_L$ would have peaks and troughs analogous to surface roughness measured circumferentially. The circumferential roughness was found to be higher than the longitudinal measurement. This could be due to the greater prevalence of the ridges seen on the surface, which have been noted in previous qualitative studies (Fan et al., 2009; Chen, Han, and Jiang, 2011).

### 3.4.3 Application to biomaterials

Surface properties of the endothelial surface can be seen to impact the blood flow and, therefore, a greater understanding of the surface roughness of coronary arteries can improve computational fluid dynamic modelling (Park, Intaglietta, and Tartakovsky, 2012). The surface roughness of novel biomaterials and surgical devices can be altered using surface modification techniques. The surface roughness measured in this study can be used as a standard to replicate natural surfaces (Nazneen et al., 2012) through surface modification methods. Surface modification allows the bulk modulus of the material to

remain unchanged, but with the additional benefit of being able to: increase the biocompatibility of materials (Kurella and Dahotre, 2005; Govindarajan and Shandas, 2014; Zhao et al., 2013; Leszczak and Popat, 2014; Liu, Chu, and Ding, 2004); influence cell growth, alignment, viability and attachment (Ross and Lahann, 2013; Espino et al., 2006; Kiyan et al., 2013; Le et al., 2013; Fioretta et al., 2012; Flemming et al., 1999; Karagkiozaki et al., 2012); and increase patency rates by deterring thrombus formation (Govindarajan and Shandas, 2014; O'Brien and Carroll, 2009; DePalma et al., 1972). Briefly, modifications are created through removal techniques (sandblasting, anodisation, etching, lithography), addition techniques (coating, nano-fibers, biomolecules), or a combination of both (Govindarajan and Shandas, 2014; Bruinink et al., 2014).

New emerging biomaterials require a standard for surface roughness. The surface roughness properties of this study contribute to providing data for such a standard and a methodology for making further measurements. This would enable artificially created surfaces, such as textured materials and stents, and surfaces encouraging endothelialisation coverage (Buys et al., 2013; Yeh et al., 2006; Kakisis et al., 2005; Schmidt et al., 2012), to be compared to healthy coronary arteries. Potentially this information could also be used to analyse disease. For example, similar to changes in the surface roughness of red blood cells with disease (Antonio et al., 2012; Buys et al., 2013; Girasole et al., 2007); or the correlation of stage of osteoarthritis, of human articular cartilage, to a fractal dimension (Peng and Wang, 2013).

### 3.4.4 Processing of tissue

This study has investigated the effects caused by freezing and chemical processing of connective tissues on the surface roughness and physical dimensions of LAD coronary arteries. The procedure of preparing LAD coronary artery samples for microscopy (i.e. freezing, glutaraldehyde-fixation, and dehydration) led to the cumulative effect of tissue shrinkage and increased circumferential surface roughness. The dehydration process caused the most significant change to values, and this was obvious when looking at the cumulative effect of processing, as fixing alone did not cause any changes. $Ra_L$ was not significantly affected by the processing, however, $Ra_C$ was more sensitive to the processing and a correction factor was developed for this (equation 3. 7). Further, equation 3. 3 and 3. 5 provide a generalised description for developing correction factors for *Ra* of soft connective tissues.

When using change in tissue dimension to normalise surface roughness values, percentage error varied from -21% to 76% (section 3.3.5). Although both the length and width of tissue specimens decreased due to processing, only $Ra_C$ was affected by processing, thus the method of using change in tissue dimension to correct surface roughness is caveated. During preliminary testing, a value of -0.63 was presented for α calculated from equation 3. 3 (Burton, Freij, and Espino, 2017). However, in this study the value of α was -0.46 (Burton, Williams, and Espino, 2017). The preliminary findings used nine samples from three specimens ($N$ = 3), whereas in this study six specimens ($N$ = 6) were used when measuring surface roughness during processing. Using an α of -0.63 resulted in an average error of 25% from the original $Ra_C$ (stage 1); whereas using an α of -0.46 resulted in an

average error of 20%. The correction factors have a similar accuracy, highlighting the repeatability of testing methods, however the second correction factor was selected as the value due to the greater specimen variability when calculating α.

Arteries are made up of smooth muscle cells, collagen, and elastin (Glagov, 1979; Fung, 1993). Fixation is used to preserve the structure of the samples and prevent degradation of connective tissues, through the reacting of aldehyde groups (Migneault et al., 2004) in the fixing solution (e.g. glutaraldehyde) with amino acids found in collagen (Damink et al., 1995), forming crosslinks between the collagen fibers (Das Murtey and Ramasamy, 2016; Huang and Yeung, 2015; Hayat, 1981), rendering some proteins non-coaguable (Hayat, 2012). These non-coaguable proteins are therefore not affected by the dehydration coagulants, preserving the structure of samples during the dehydration process (Hayat, 1981, 2012). Conversely, elastin is not fixed by glutaraldehyde or formaldehyde fixatives (Fung and Sobin, 1981).

Glutaraldehyde is often chosen for fixation to attempt to preserve the mechanical properties of tissue (Mukherjee et al., 2012), preventing their degradation during storage for instance. However, the cross-linking process is known to affect the anisotropy of biological materials such as pericardium tissue (Sung et al., 1999), with an increase in mechanical strength seen in pulmonary ligaments (Chen et al., 2016) and increase in elasticity noted elsewhere in pericardial tissue (Radjeman and Lim, 1986). Conversely, heart valve tissue was found to be less stiff following fixation (Vesely, 1996). Regardless, fixation affects the structure and mechanical strength of tissue. The results of this study determined that the surface roughness was not affected by the fixation procedure; however, it is unclear

whether the cross-linking of proteins would be expected to alter the surface roughness of an endothelium lined coronary artery.

The use of osmium tetroxide as a secondary fixative is common for transmission electron microscopy to stain membranes and provide contrast whilst imaging, and for SEM imaging as a heavy metal increases the samples' conductivity. However, secondary fixation has been deemed unnecessary for non-delicate tissue (Moran and Coats, 2012) and can also cause damage to proteins (Kashi et al., 2014). Hence, in this study, a secondary fixative was not investigated. However, the method presented in this study could be used to assess the changes caused by a secondary fixative, or alternative primary chemical fixatives, to the surface roughness and physical dimensions of tissue.

Dehydration prevents the distortion of light when performing microscopy and is necessary to ensure a vacuum for traditional SEM for instance (Hayat, 1981; Reichlin et al., 2005). Biological tissue in the human body is naturally hydrated, and the dehydration of tissue has been shown to affect its viscoelastic properties (Pearson and Espino, 2013; Xu et al., 2011). Hence, an alcohol concentration series, like that chosen within this study, allows dehydration to be completed in a controlled manner, minimising distortion of the specimen (Beck, 1998; Moran and Coats, 2012). A final dehydration step removes the alcohol from within the samples. Critical point drying is a traditional procedure used for preparing biological samples for SEM investigation (Beck, 1998). However, HMDS is a chemical alternative that reduces both time and costs without compromising the quality of image (Moran and Coats, 2012), therefore it was chosen in this study. The dehydration process removes both free water molecules, and those bound to the tissue such as water soluble

proteins. Therefore, the results of this study which show that both the circumferential surface roughness and physical dimensions of coronary arteries are significantly altered due to dehydration appear reasonable. Further, the dependency of tissue dimensions on hydration, and the finding in this study that surface roughness changed significantly only subsequent to dehydration, imply that the need for a correction factor to compensate for the changes due to processing should be considered particularly when tissue processing includes dehydration.

### 3.4.5 Storage of biological tissue

The protocol for storing soft tissue by freezing used in the present study followed standard protocols used by other studies of porcine heart tissue (Millard et al., 2011; Espino, Shepherd, and Buchan, 2007; Espino et al., 2006; Espino et al., 2005). Freezing prevents the degradation of biological tissues which require storage (Goh et al., 2010). Clark, however, noted stiffening of vascular tissue when comparing frozen to fresh human aortic and mitral leaflets and chordae (Clark, 1973). It is noted, though, that there was extensive overlap in results from fresh and frozen specimens in Clark's results. While other studies have noted that any effects of freezing soft connective tissues are outweighed by the standard deviation of the original measurements (Peters et al., 2017). Further, storing other soft tissues at -20 °C have revealed no changes in mechanical properties including porcine liver (Wex et al., 2014), porcine aortic samples (O'Leary, Doyle, and McGloughlin, 2014) and murine tendons (Goh et al., 2010) to name but a few. Moreover, neither repeated freeze-thaw cycles or extended frozen storage have been found to lead to more than minimal changes in biomechanical properties, for bone-patella tendon-bone soft tissue allografts (Jung et al.,

2011) and porcine aortic tissue (O'Leary, Doyle, and McGloughlin, 2014), respectively. This is consistent with our own finding that a freeze-thaw cycle did not alter surface roughness of the tissue at -40 °C. Instead, freezing temperature (Goh et al., 2010) and method of freezing preservation (Aidulis et al., 2002) may be of greater relevance. Increased rate of storage and lower storage temperature are known to reduce of the size ice-crystals (Hukins, Leahy, and Mathias, 1999), with smaller ice-crystals having less effect on the extra-cellular matrix composing soft connective tissues (Hickey and Hukins, 1979).

Previous studies have highlighted the benefits of storing tissue cryogenically with an appropriate cryo-protectant (Müller-Schweinitzer, 1994) to allow indefinite storage of blood vessels. Additionally, without the use of a cryo-protectant when storing at -20 °C stress-strain properties of porcine femoral arteries were altered potentially due to ice crystal growth or damage to the extracellular matrix (Grassl, Barocas, and Bischof, 2004). For this current study, an accepted protocol for storing fresh connective tissues -40 °C was followed (Espino et al., 2005), consistent with the recommendation of using a freezing, rather than refrigeration, protocol to maintain initial stress-strain behaviour of aortic tissue (Chow and Zhang, 2011). Freezing alone did not affect the surface roughness or physical dimensions of samples. The results in this study confirm that soft connective tissues stored at -40 °C are not altered in physical dimensions; further, that this storage procedure does not affect the surface roughness (*Ra*) of coronary arteries. Although no significant difference was seen in surface roughness after a freeze-thaw cycle, some established storage procedures do incorporate cryo-storage and cryo-protectants (Müller-Schweinitzer et al., 1997; Müller-Schweinitzer, 1994; Van Vré et al., 2011). Therefore, it would be of value to assess the effect

of cryo-protectants on the surface roughness of soft connective tissues using the methodology from this current study.

### 3.4.6 Correcting for processing of biological tissue

The correction factor in this study can be used as a standard for preparing coronary artery tissue through fixation and dehydration. This correction factor would provide outer limits of the circumferential surface roughness measurements, analogous to how the tissue fraction effect is corrected for in dynamic imaging (Holman et al., 2015). A correction factor would be beneficial for assessing the effect that processing techniques have on surface roughness measurements of biological tissues. It is accepted that measurements of tissue dimension (Hołda et al., 2016), tumour volume (Schned et al., 1996), and cell density (Doughty, 1995) should be corrected due to the effect of processing, however, this correction has not been quantified previously for surface roughness. The results of this study are beneficial to the development of biomaterials, where replicating the endothelium could be achieved through surface modification techniques, including nano-texturing. This would leave the bulk modulus of the material unchanged, but allow the opportunity to influence cell formation (Ross and Lahann, 2013; He et al., 2005; Espino et al., 2006; Kiyan et al., 2013; Flemming et al., 1999; Karagkiozaki et al., 2012; Fioretta et al., 2012; Vartanian et al., 2008; Vartanian et al., 2009; Le et al., 2013), increase patency rates (Govindarajan and Shandas, 2014; O'Brien and Carroll, 2009; DePalma et al., 1972), and increase biocompatibility (Kurella and Dahotre, 2005; Govindarajan and Shandas, 2014; Liu, Chu, and Ding, 2004; Zhao et al., 2013; Leszczak and Popat, 2014).

This study used glutaraldehyde based fixation, typically associated with the preparation of samples for SEM. This assessment is of value because it is difficult to perform SEM on tissues without any preparation, i.e. to obtain a baseline measurement for comparison. Therefore, the correction factor calculated would be suitable when using the stated protocols when preparing samples for investigation by SEM. This study, however, has used light microscopy which is typically associated with fixatives such as formalin or paraformaldehyde (Angiero et al., 2012; Zhao, Thambyah, and Broom, 2014). Given that such fixatives tend to be milder as compared to glutaraldehyde fixation, they would not be expected to alter surface roughness. Pointedly, though, the methods proposed in this study could be replicated to assess the effect of a range of fixation (e.g. formalin, paraformaldehyde, etc.) and/or dehydration protocols on surface roughness. The methods proposed also enable the need for correction factor to be determined, for a range of soft connective tissues being evaluated for surface roughness. The average mean corrected value of $Ra_{C6}$ for the initial eight porcine hearts was 1.04 ± 0.47 µm, which is comparable to the value of 1.31 ± 0.21 µm found when assessing the chemical processing effect on the six porcine hearts. A change in *Ra* after processing was only noted in the circumferential direction. Collagen is orientated circumferentially within the thicker medial layer, but longitudinally in the thin sub-endothelial layer; hence a change in surface roughness circumferentially may be due to the collagen within the thicker medial layer causing a significant distortion during fixation compared to longitudinally (Timmins et al., 2010).

The uncorrected $Ra_C$ and $Ra_L$ values (1.98 ± 0.27 µm and 0.99 ± 0.39 µm, respectively; $N$ = 8) initially measured to assess the variation of surface roughness along the length of the LAD coronary artery (Burton, Freij, and Espino, 2017) are comparable to those measured to

assess the effect of processing (1.69 ± 0.75 µm and 0.89 ± 0.27 µm, respectively; *N* = 6) (Burton, Williams, and Espino, 2017). This confirms the repeatability of results, and emphasises the importance of using a correction factor for the circumferential surface roughness. Chen et al. categorises surface roughness into three groups: surfaces with *Ra* >2 µm show that an increase in *Ra* creates a more thrombogenic surface due to the increase in surface area for platelet adhesion; surfaces with *Ra* between 2 µm and 50 nm may contain topographical features to reduce the contact area for platelet adhesion; and surfaces with *Ra* of <50 nm are considered smooth to platelets (Chen, Han, and Jiang, 2011). The results from this study specifies the surface roughness of coronary arteries falls within the 2 µm and 50 nm range, suggesting a potential micro-structure provides the antithrombogenic properties associated with healthy coronary arteries. Investigation into the multiscale surface roughness of coronary arteries would allow further investigation into the potential multi-scale surface characteristics of coronary arteries.

### 3.4.7 Multi-scale characterisation

Coronary arteries are anisotropic, where mechanical properties vary from the longitudinal to circumferential direction. The results in this study suggest that their surface roughness is also anisotropic, with *Ra* of LAD coronary arteries being significantly higher in the circumferential than longitudinal direction. This may have implications for recent studies investigating the helical flow in coronary arteries (Chiastra et al., 2017), and potentially multi-scale analysis of such flow (Lee and Smith, 2012). The main factor in the anisotropy of surface roughness appeared to be the presence of ridges along the artery. These ridges may depend on the underlying arrangement of macro-molecules such as collagen (Purslow,

Wess, and Hukins, 1998) and their orientation in arteries (Dahl et al., 2003; Chen, Han, and Jiang, 2011; Fan et al., 2009), and/or may impact on the endothelial cell orientation along the arteries (Chen, Cornwell, et al., 2013). The methods and findings within this chapter, including the correction factor calculated, are applied in chapter 4 to assess the multi-scale characteristics of surface roughness.

## 3.5 CONCLUSION

The following conclusions can be made of porcine LAD arteries:

- the uncorrected surface roughness value measured circumferentially was greater than measured longitudinally (1.69 ± 0.75 µm compared to 0.89 ± 0.27 µm, respectively);
- surface roughness did not vary along the length of the LAD artery;
- a freeze-thaw cycle at -40 °C does not significantly alter the surface roughness measurement or physical dimensions of porcine LAD;
- the cumulative process of glutaraldehyde based fixation followed by dehydration, caused no significant difference to $Ra_L$ of porcine LAD, measuring an average mean of 0.99 ± 0.39 µm;
- the cumulative process of glutaraldehyde based fixation followed by dehydration, caused a significant increase to $Ra_C$, from 1.36 ± 0.40 to 1.98 ± 0.27 µm;

- changes to surface roughness due to processing of tissue, as described by this paper, can be accounted for by applying the following correction factor:

$$Ra_{C\beta} = \frac{Ra_C}{1.46}$$

- corrected $Ra_{C\beta}$ has an average mean of 1.31 ± 0.21 µm.

In conclusion, while individual preparation procedures of tissues for microscopy may not alter the surface roughness of coronary arteries, additive effects may be present (particularly following dehydration) which may require a correction factor. For coronary arteries this is the case circumferentially, but not longitudinally.

# 4 MULTISCALE IMAGING

## 4.1 OVERVIEW

The surface of blood vessels has been qualitatively analysed (Bertazzo et al., 2013) but this provides no quantitative measurement of surface roughness. Previous work described in chapter 3 quantitatively analysed the surface of coronary arteries and discussed the importance of a correction factor when measuring surface roughness of processed tissue (Burton, Williams, and Espino, 2017), and section 2.3.2 discusses how surface roughness can be used to influence the design and development of biomaterials. The surface roughness of other biological tissue, such as articular cartilage (Forster and Fisher, 1999; Ghosh et al., 2013), has been investigated without the use of a correction factor. These studies have noted a multiscale variance when assessing the surface of biological surfaces (Ghosh et al., 2013). It is unknown whether a similar relationship is noted for surface roughness of coronary arteries. Although the surface roughness has been analysed by light microscopy (Burton, Freij, and Espino, 2017), the maximum magnification of the Alicona system used was 100×. For a higher magnification, an alternate system such as scanning electron microscopy (SEM) or atomic force microscopy (AFM) is preferred, as these techniques can capture the surface at a micro- and nano- scale. However, different microscopy techniques can provide dissimilar results (Forster and Fisher, 1999). For a comparison of magnification across a variety of microscopy techniques, a like-for-like magnification should be established to provide an overlap between results. Understanding the multiscale variance in the surface roughness would present a quantifiable boundary condition to enable multi-scale computational fluid dynamic (CFD) modelling of coronary arteries.

A helical blood flow has been noted in coronary arteries (Stonebridge and Brophy, 1991; Morbiducci et al., 2009; Chiastra et al., 2017), which could be caused by the ridges seen along the surface of coronary arteries (discussed in chapter 3). Further, atherosclerotic lesions form in a spiral pattern along coronary arteries and have been shown to affect flow resistance and wall shear stress at micro-scale levels (Wong et al., 2006). Understanding of this helical phenomenon is relatively limited, and it is unknown as to whether the phenomenon reduces or increases the chance of atherosclerotic lesions to form (Kirsanov and Kulikov, 2012). However, the phenomenon is now considered in the design of vascular devices to reduce neointimal hyperplasia (Liu et al., 2014). Assessing the surface of coronary arteries at multi-scale will provide invaluable information to predict the effect of multi-scale roughness, for example through disease of coronary arteries, on blood flow and this helical phenomenon. Additionally, this will aid in the development of new biomaterials that can increase or decrease this phenomenon.

The aim of this chapter is to assess the effect of magnification and microscopy type on the surface roughness of left anterior descending (LAD) coronary arteries. The methods of optical microscopy, SEM and AFM are considered to allow multiscale comparison of surface roughness between 10× to 2000× magnification. Results are presented for individual microscopy techniques, including through optical microscopy as presented in chapter 3.2.3, and trends of surface roughness are investigated between microscopy techniques and magnification. The correction factor calculated in chapter 3 (section 3.3.4, equation 3. 7) was applied to *Ra* results to provide outer limits of circumferential surface roughness.

## 4.2 METHODS

### 4.2.1 Outline

To allow a multiscale analysis of surface roughness, magnification was varied from 10× to 2000× across microscopy techniques, and also included an equivalent magnification of 5500× (table 4. 1). Due to charging damage associated with SEM, it was not possible to reuse samples with AFM (specimens identified in table 4. 1). The maximum magnification lens with optical microscopy was 100×, therefore the minimum magnification investigated via optical microscopy was an order of magnitude smaller, at 10× magnification. This builds on work discussed in chapter 3, where 10× magnification was chosen as the optimum magnification for the surface roughness values measured.

To assess an overlap of scale, SEM was investigated with a minimum magnification of 100× to allow like-for-like comparison with optical microscopy. Again, to assess multiscale effects of surface roughness, surface imaging was performed at an order of magnitude greater (1000×) than the SEM minimum magnification, and also at twice this magnification (2000×). A greater equivalent magnification was possible (5500×) due to AFM, and this was also investigated.

*Table 4. 1 – Specimen selection. †AFM magnification is not a true magnification, but a calculated equivalent magnification (see section 4.3.3 for further detail). In heart identification, the letters a-h identify which specimens were used for which microscopy techniques.*

| **Microscopy type** | **Heart identification** | **Scan area** | **Number of repeat *Ra* (in each orientation)** | **Magnifications** |
|---|---|---|---|---|
| Optical | *N* = 6 (a, b, c, d, e, f) | 1623 × 1623 µm<br>811 × 811 µm<br>323 × 323 µm<br>162 × 162 µm | *n* = 5 | 10<br>20<br>50<br>100 |
| Scanning electron | *N* = 5 (d, e, f, g, h) | 1230 × 1700 µm<br>123 × 170 µm<br>61 × 85 µm | *n* = 5 | 100<br>1000<br>2000 |
| Atomic force | *N* = 3 (a, b, c) | 50 × 32 µm | *n* = 3 | 5500† |

### 4.2.2 Dissection and initial sample preparation

Eight porcine hearts were dissected and prepared as described in chapter 3.2.2 (Burton, Freij, and Espino, 2017; Burton, Williams, and Espino, 2017). For this study, the middle specimens were selected for investigation, as previous work (presented in chapter 3) found no change in surface roughness along the length of the LAD coronary artery (Burton, Freij, and Espino, 2017). To assess the multiscale surface roughness of coronary arteries, specimens were imaged through optical, scanning electron and atomic force microscopy. As previously described, surface roughness was assessed in the circumferential and longitudinal directions, *x* and *y* axis respectively (chapter 3).

For this study, to allow a comparison between magnification and microscopic technique, all specimens were fixed and dehydrated following the protocol in chapter 3.2.4. This was essential when imaging specimens particularly for SEM under vacuum conditions, which requires dehydrated samples to prevent liquid within a sample from vaporising.

### 4.2.3 Optical imaging

Using an optical focus variation microscope (G5 Infinite Focus, Alicona UK, Kent, UK), images were taken at 10×, 20×, 50× and 100× magnifications ($N$ = 6). Lighting conditions, focussing points and resolutions were set as described in chapter 3.2.3. The area of scan was selected as the automatic region at each magnification to reduce scan time and file size (table 4. 1). Areas were selected to avoid bifurcations and damage due to dissection when selecting the 10× magnification zone, as described in chapter 3.2.3. Scan areas were taken at the same central $x$ and $y$ positions as the 10× magnification area, simply increasing the magnification at the centre of each image. Three-dimensional (3D) reconstruction was performed using the Alicona IF-Laboratory Measurement Module (version 6.1, Alicona UK, Kent, UK), from which the mean average of five Ra values was measured across the entire longitudinal and circumferential lengths, calculating both the circumferential ($Ra_C$) and longitudinal ($Ra_L$) surface roughness. This resulted in 30 data values for $Ra_C$ and $Ra_L$ separately, at each magnification, across the six porcine LAD specimens.

### 4.2.4 Scanning electron microscopy

SEM allows higher magnification investigation of a specimen. Under vacuum conditions, an electron beam is fired at the surface of the sample. In addition to preparing specimens through fixation and dehydration (section 4.2.2), for SEM investigation specimens

underwent sputter coating (figure 4. 1). Non-conductive samples, such as biological tissue, require sputter coating before electron imaging to prevent charging. Charged samples can cause artefacts such as warping to the image, where trapped electrons repel the electron beam and distort the resulting image. Sputter coating provides grounding and a thin, conductive coating to specimens (Beck, 1998). Thus, prior to imaging samples using SEM, specimens were mounted on an SEM stub with conductive double-sided tape and were sputter coated with gold at 2.5kV using an Agar automatic sputter coater (figure 4. 1, Agar Scientific, Elektron, Technology UK Ltd, Essex, UK) for 30 s at 20 mA, followed by a further 30 s at 30 mA, to ensure an even covering of 150-200 Å (Beck, 1998).

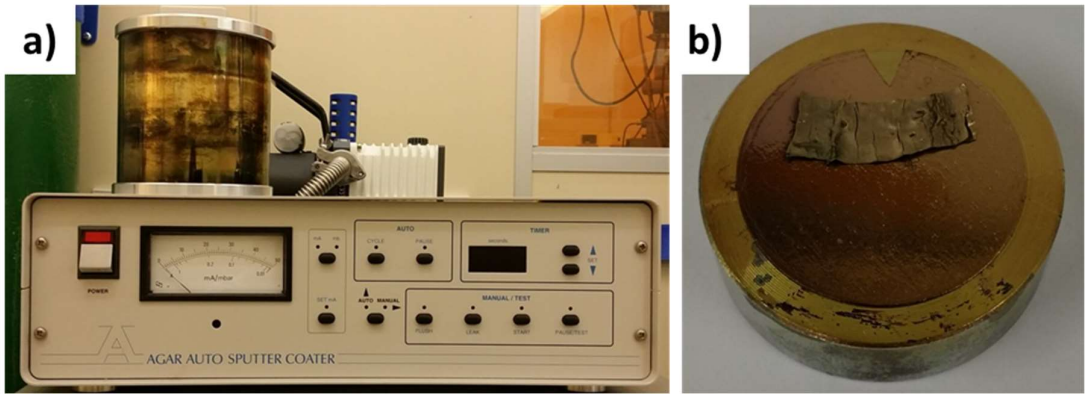


*Figure 4. 1 – (a) Agar automatic sputter coating machine (Agar Scientific, Elektron, Technology UK Ltd, Essex, UK); (b) sputter coated specimen mounted on SEM stub with conductive tape.*

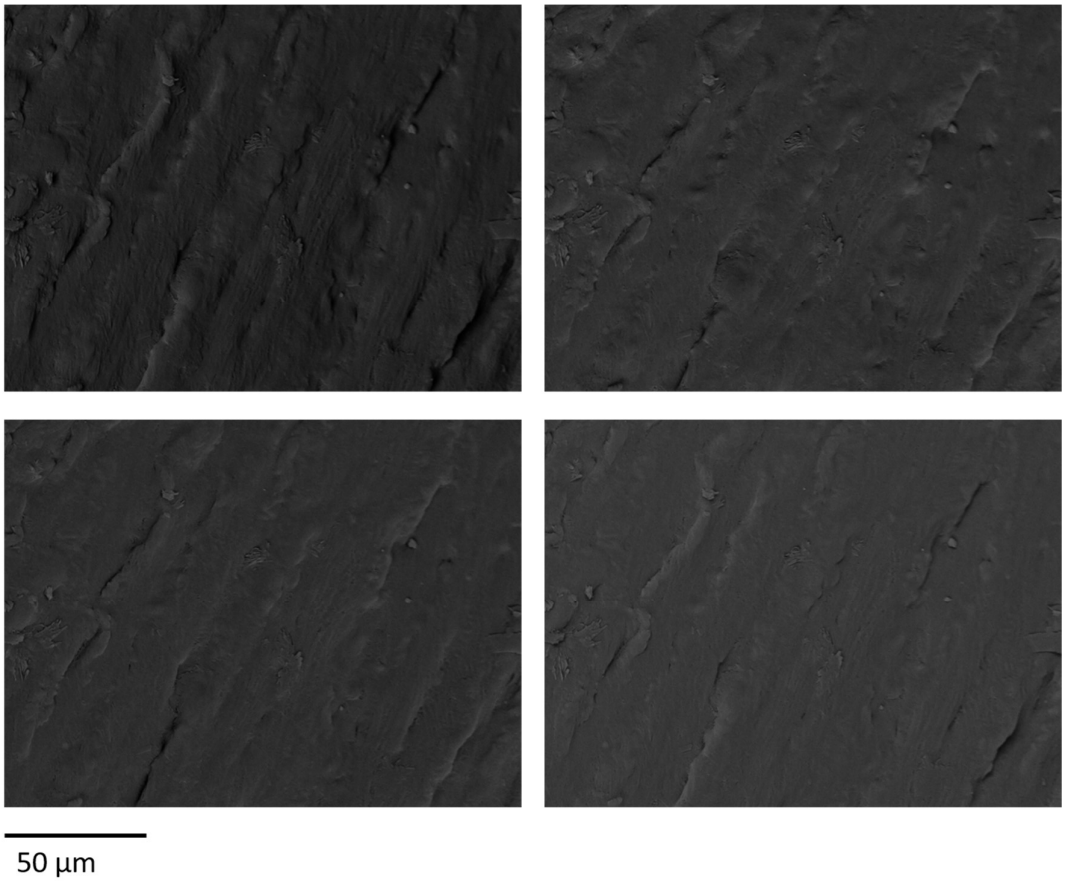


*Figure 4. 2 – 4 surface scans captured by the Quad Back Scatter Electron (BSE) detector of the same surface area, imaged at 1000× magnification by SEM.*

Samples were imaged using a Hitachi TM3030 SEM (figure 4. 4, Hitachi Ltd., Tokyo, Japan) at 15 kV. Surfaces were scanned at 100× magnification, at 1000× magnification, and 2000× magnification ($N$ = 5). After the electron beam strikes the surface, the backscattered primary electrons are released, and these are detected by the Quad Back Scatter Electron (BSE) detector (figure 4. 3) as two-dimensional (2D) surface scans (figure 4. 2). The 4 surface scans are stitched together automatically to create a 3D reconstruction using 3D-VIEW software (Hitachi Ltd., Tokyo, Japan) (Hitachi, 2013). Similar to the method of surface roughness measurement with optical microscopy (chapter 3.2.3), the mean average of five

values was calculated for *Ra* in both the circumferential and longitudinal direction, along the full length of the imaged region, resulting in 25 data values for both $Ra_C$ and $Ra_L$ separately, at each magnification, across the five porcine LAD specimens. Areas such as bifurcations and damage due to dissection were avoided (as described in chapter 3.2.3).

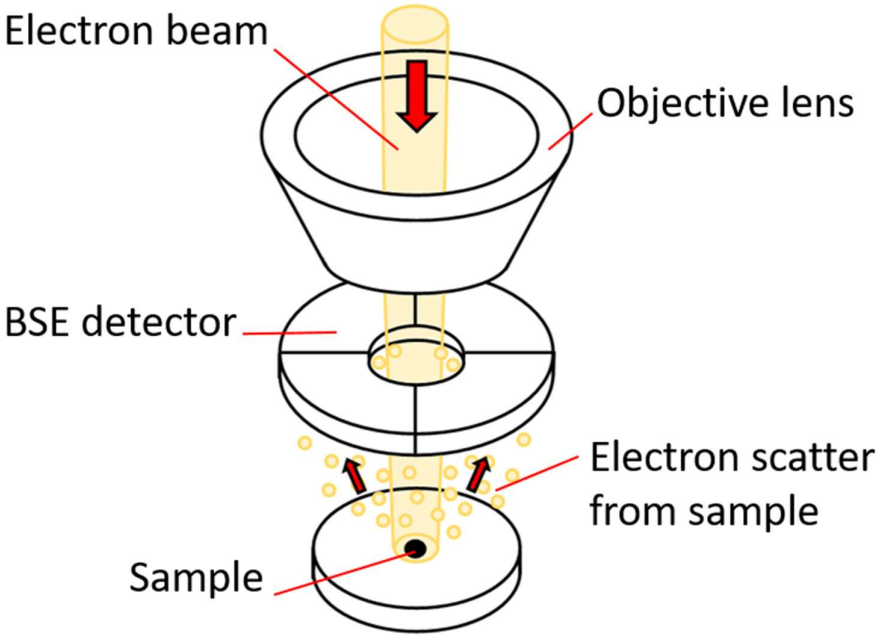


*Figure 4. 3 – BSE detection. Electron beam passes through objection lens and hits sample, causing electron scatter. BSE detector detects the back scattered electrons. The BSE detector is sectioned into four quadrants, resulting in 4 separate surface scans.*


*Figure 4. 4 – TM3030 table top SEM (Hitachi Ltd., Tokyo, Japan).*

### 4.2.5 Atomic force microscopy

The same specimens that had been dissected and processed in section 4.2.3 and 4.2.4 were used for AFM investigation (table 4. 1). AFM measures the surface of a sample in 3D, with a probe scanning the surface in a raster pattern whilst measuring the horizontal (*x* and *y* plane) and vertical (*z* plane) position of the probe (figure 4. 6). Measurements were made using a Nanowizard II AFM (JPK Instruments AG, Berlin, Germany), operating in non-contact tapping mode, using height profile modulation (figure 4. 5). This method has been used by others when studying the surface of arteries (Timashev et al., 2016).

As the tip of the probe scans the surface of the sample, van der Waals forces are detected between the sample and tip through deflection of the probe, which is calculated

from the reflected laser deflection (figure 4. 6). PointProbe Plus non-contact high resonance frequency silicon scanning mode microscopy sensors were employed, with tip radius <10 nm (Nanosensors TM., Switzerland), similar to the 8 nm tip radius used by Timashev *et al*. when studying arteries with AFM (Timashev et al., 2016). The non-contact mode was chosen due to tissue deformation associated with AFM in contact mode (Canale et al., 2011), and also concerns of the tip moving in a jerking motion due to stick-slip phenomenon (Mate et al., 1987).

The tip height was 10-15 µm, with a cantilever force constant of 10-130 N/m. An area of 50 µm × 32 µm was scanned. Scans were processed using JPK Data Processing software (JPK Instruments AG, Berlin, Germany). The mean of three values was calculated for *Ra* in both the circumferential and longitudinal direction for each sample, resulting in 9 data values for both $Ra_C$ and $Ra_L$ separately across the three porcine LAD specimens. This used the same averaging process of assessing *Ra* in three different regions as performed in other studies (Tholt et al., 2006). The *Ra* profiles were taken across the entire length of the *x* and *y* axis of the scanned area ($Ra_C$ and $Ra_L$ respectively), with areas of bifurcation and dissection damage avoided (described in chapter 3.2.3).

As AFM uses a probe to scan the surface, a magnification is not set for this method. However, an equivalent magnification can be calculated from the resultant size of image displayed from the actual size of image scanned (equation 4. 1).

*Equation 4. 1*

$$\text{Magnification} = \frac{\text{Measured distance}}{\text{Actual distance}}$$

*Figure 4. 5 – Nanowizard II AFM (JPK Instruments AG, Berlin, Germany).*

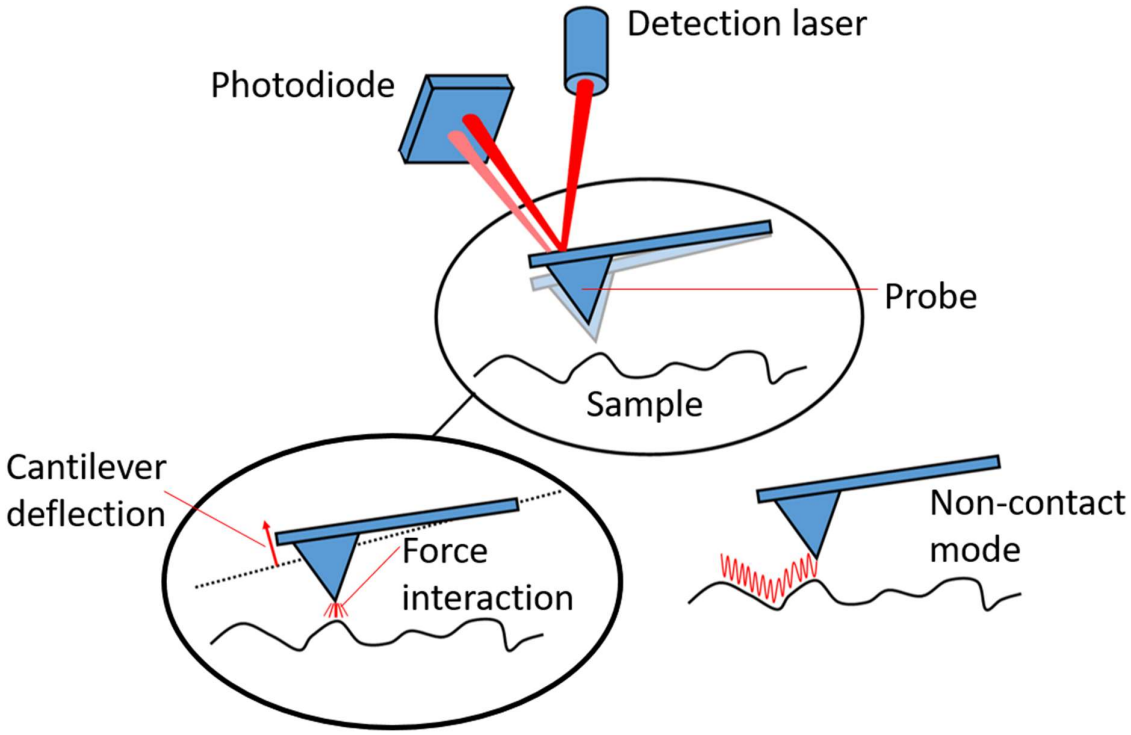


*Figure 4. 6 – Principles of AFM. Deflected probe results in reflected laser detection, identified by the photodiode. Cantilever deflection is caused due to the force interaction between sample and probe tip. In non-contact mode the tip oscillates close to the sample surface.*

### 4.2.6 Correction factor

The correction factor presented in chapter 3 was calculated for specimens where a significant difference was seen in *Ra* before and after processing. Its purpose was to present the outer limits of *Ra* values. Thus, the correction factor (equation 4. 2) was applied to surface roughness in the circumferential direction to give $Ra_{C\beta}$, as a significant difference was seen in $Ra_C$ due to processing (chapter 3).

*Equation 4. 2*

$$Ra_\beta = \frac{Ra}{1.46}$$

### 4.2.7 Surface reconstruction

For microscopy techniques that output a 3D data point cloud in a plain text format, with data presented in a 3 × *n* array of *x*, *y*, and *z* axes co-ordinates, 3D reconstruction can be performed in external numerical computing software. Using a script programmed in MATLAB (MathWorks, Natick, MA, USA), a plain text file was loaded, the 3D point cloud was interpolated to fill in any voids of missing data, and a surface was reconstructed from the scan data. The code used to create these reconstructions is provided in the Appendix.

### 4.2.8 Data analysis

Two separate analyses were performed on data: the first assessed if magnification caused a significant difference to surface roughness; the second assessed if microscopic technique caused a significant difference to surface roughness. For this, the null hypothesis of a one-way analysis of variance (ANOVA) was assessed, with Tukey pairwise post hoc test used to assess a significant difference ($p < 0.05$) in surface roughness due to magnification with both optical microscopy and SEM separately. A two-way ANOVA was deemed inappropriate due to the lack of significant overlap in magnification variables between microscopy techniques. Additionally, significant differences in surface roughness were assessed ($p < 0.05$) in magnification groups across microscopic techniques combined, which also included results measured by AFM (Reilly, 2015; Bland, 2000).

Finally, surface roughness in the circumferential and longitudinal direction was assessed for significant difference ($p < 0.05$), testing the null hypothesis using a student paired *t-test* at all magnifications with each microscopy technique. Data is presented as mean ± standard deviation unless otherwise stated. The correlation of surface roughness

was assessed for the multiscale results of optical microscopy and SEM, with significance assessed for relationship fit ($p < 0.05$).

## 4.3 RESULTS

### 4.3.1 Optical imaging results

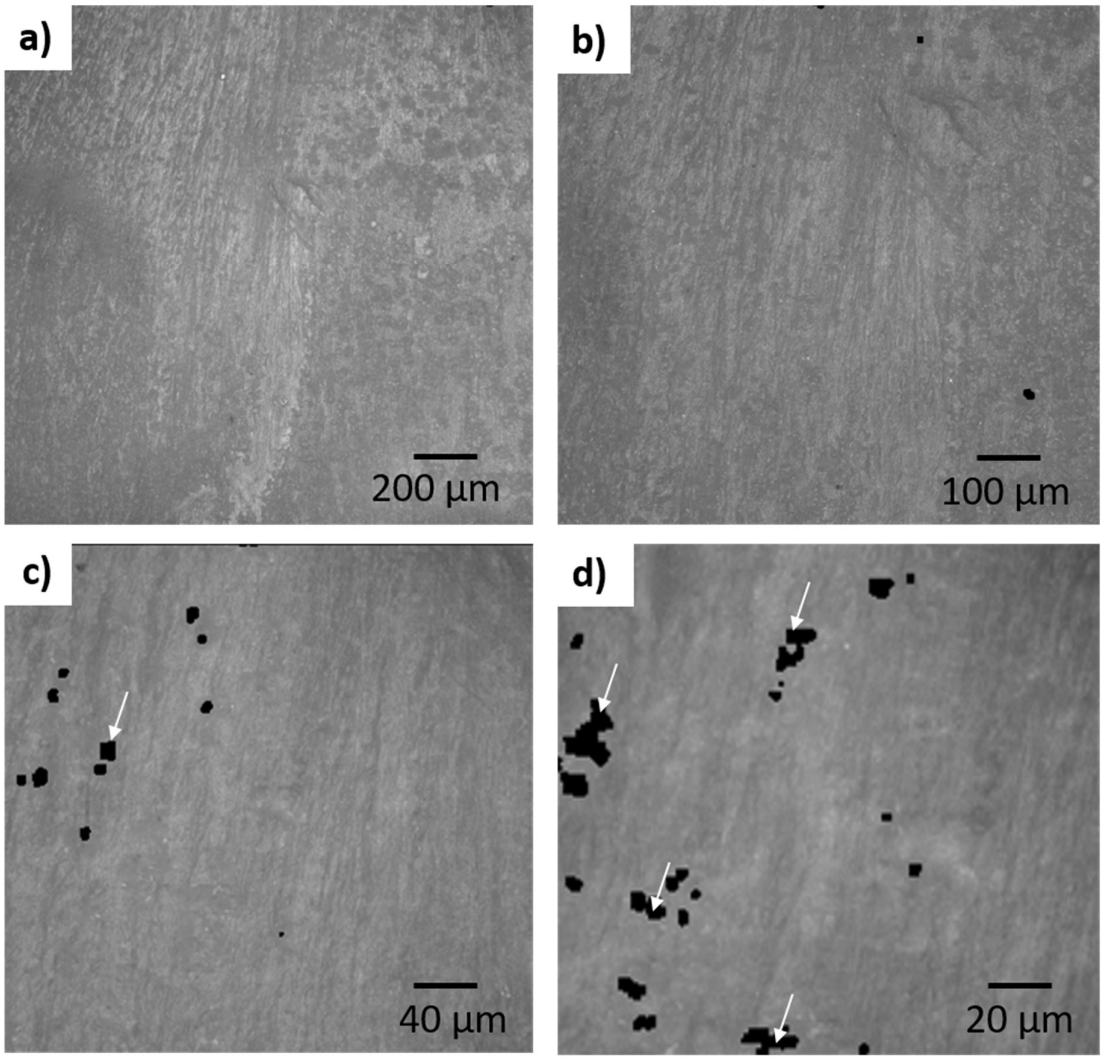


*Figure 4. 7 – 2D optical images using Alicona Infinite Focus microscope at (a) 10×, (b) 20×, (c) 50× and (d) 100× magnification. Missing data points identified by the white arrows.*

Using magnifications between 10× to 100× with the optical microscope method did not significantly alter the measured *Ra* value ($p > 0.05$; table 4. 2). When measuring surface roughness from 3D reconstructed optical images, $Ra_C$ was significantly greater than $Ra_L$ at all magnification levels (0.72 ± 0.31 µm and 0.28 ± 0.10 µm; table 4. 2; $p < 0.05$).

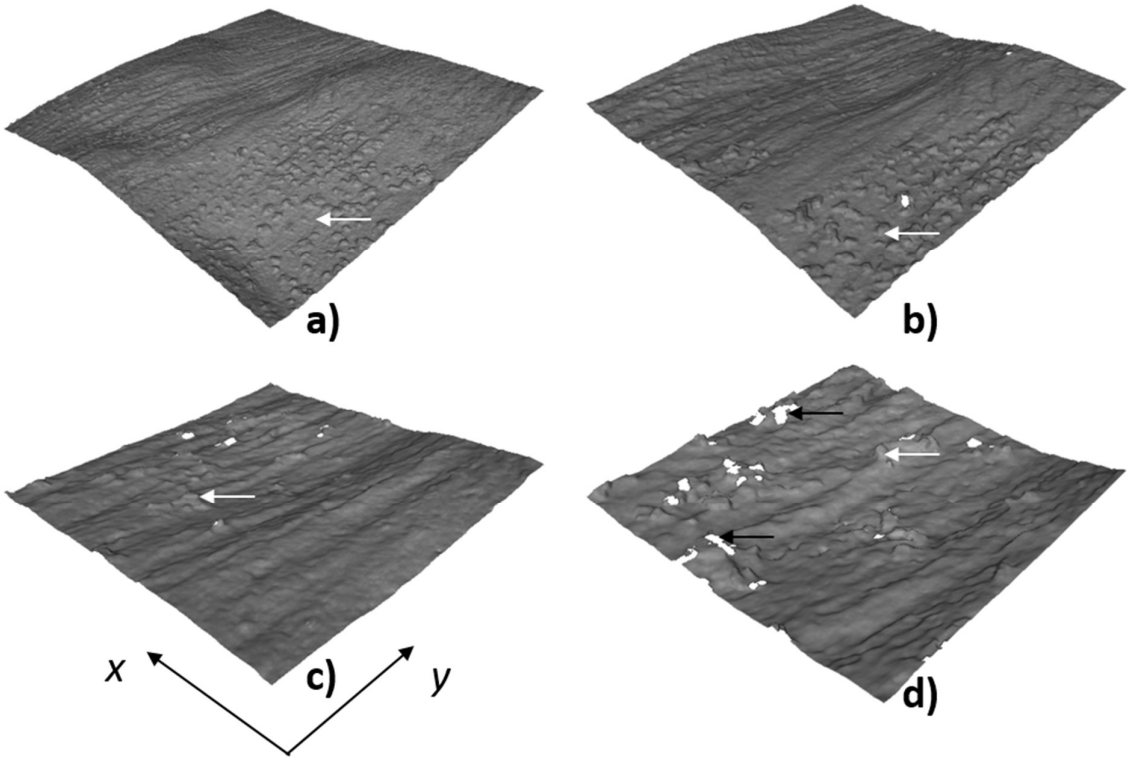


*Figure 4. 8 – 3D reconstruction of optical images at (a) 10×, (b) 20×, (c) 50×, and (d) 100× magnification. Specimen dimensions along the x and y axes are a) 1623 × 1623 µm; b) 811 × 811 µm, (c) 323 × 323 µm, (d) 162 × 162 µm. Minor residue – white arrow. Missing data points – black arrow.*

2D images at each optical magnification, and corresponding 3D reconstruction, are shown in figures 4. 7 and 4. 8 respectively, from which ridges are visible along the longitudinal direction. Artefacts visible on the surface include gaps in the data set, due to distortion of light causing incorrect collection of data points by the microscopy system. There are also minor residues from the processing of tissue visible as small bumps on the surface.

### 4.3.2 SEM results

Using magnifications between 100× to 2000× with the SEM method did not affect *Ra* values ($p > 0.05$; table 4. 2). However, unlike optical microscopy, when using SEM methods to measure surface roughness there was no significant difference between $Ra_C$ and $Ra_L$ (0.21 ± 0.09 µm and 0.19 ± 0.08 µm; table 4. 2; $p > 0.05$) for each magnification. 3D reconstructed and 2D SEM images are shown in figure 4. 10 respectively, where ridges are seen in the longitudinal direction at all magnifications. Again, minor residue due to processing is present on the surface of specimens causing artefacts. Additionally, in the 2D reconstruction slight charging is apparent (figure 4. 10), and cracks can be seen on the surface of the specimen due to processing then flattening specimen for SEM.

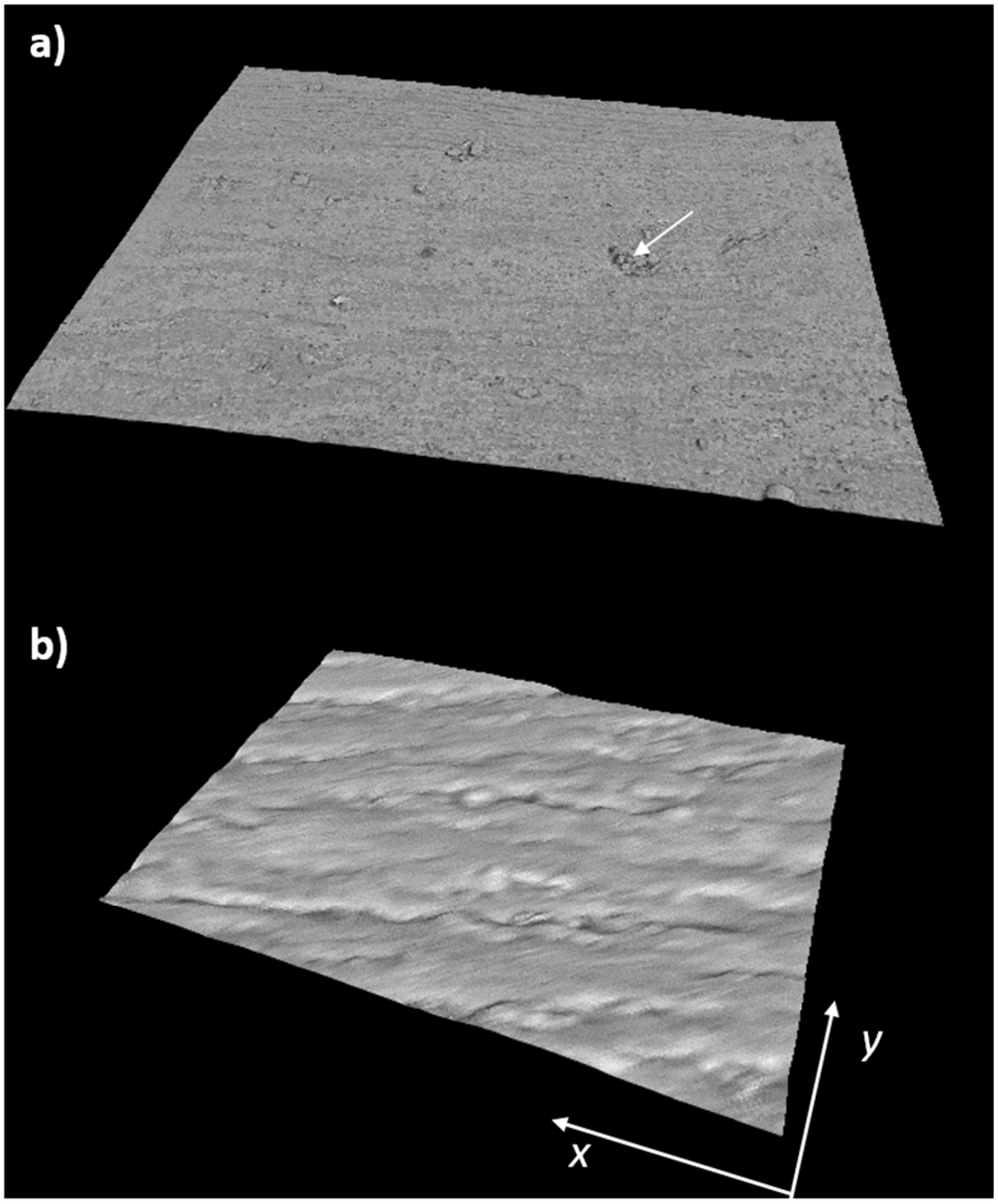


*Figure 4. 9 – 3D reconstruction of SEM images at (a) 100× and (b) 1000× magnification. Specimen dimensions in x and y axis are (a) 1700 × 1230 µm and (b) 170 × 123 µm. Minor residue – white arrow.*

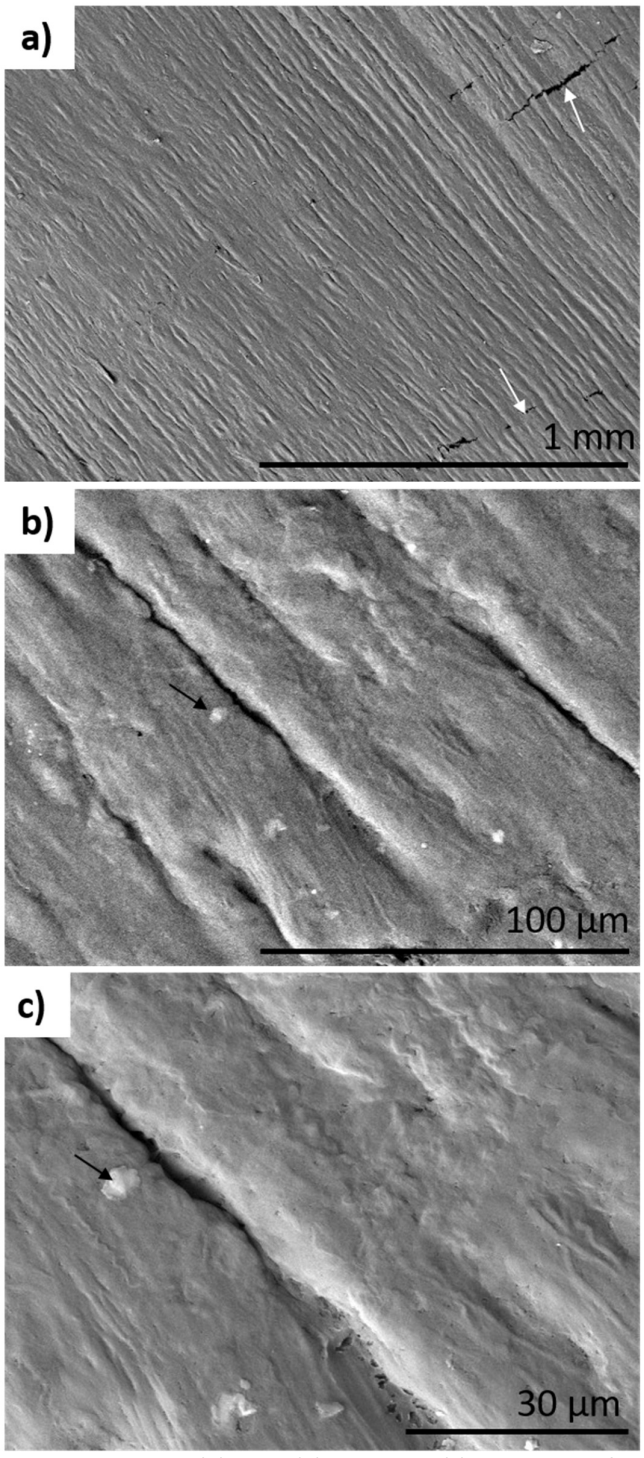


*Figure 4. 10 – 2D SEM images at (a) 100×, (b) 1000× and (c) 2000× magnification. Minor residue – white arrow. Charging of specimen – black arrows. Cracks in specimen – white arrows.*

### 4.3.3 AFM results

An equivalent magnification was calculated for AFM, using equation 4. 1. When displayed on a 24-inch computer monitor, an AFM image had a width of 275 mm, where the scanned width is 50 µm. Therefore, an equivalent magnification would be 5500×.

Figures 4. 11 and 4. 12 show a 2D surface image and it corresponding 3D reconstructed image, with the longitudinal direction (ridge alignment) identified in figure 4. 11. The scale bar displayed in figure 4. 11 would indicate that the AFM surface was imaged equivalent to the 5500× magnification (equation 4. 1), which displays comparable surface characteristics at a similar scale. Minor residue from the processing of tissue is apparent on the surface of the specimen (figure 4. 11) creating an artefact on the surface.

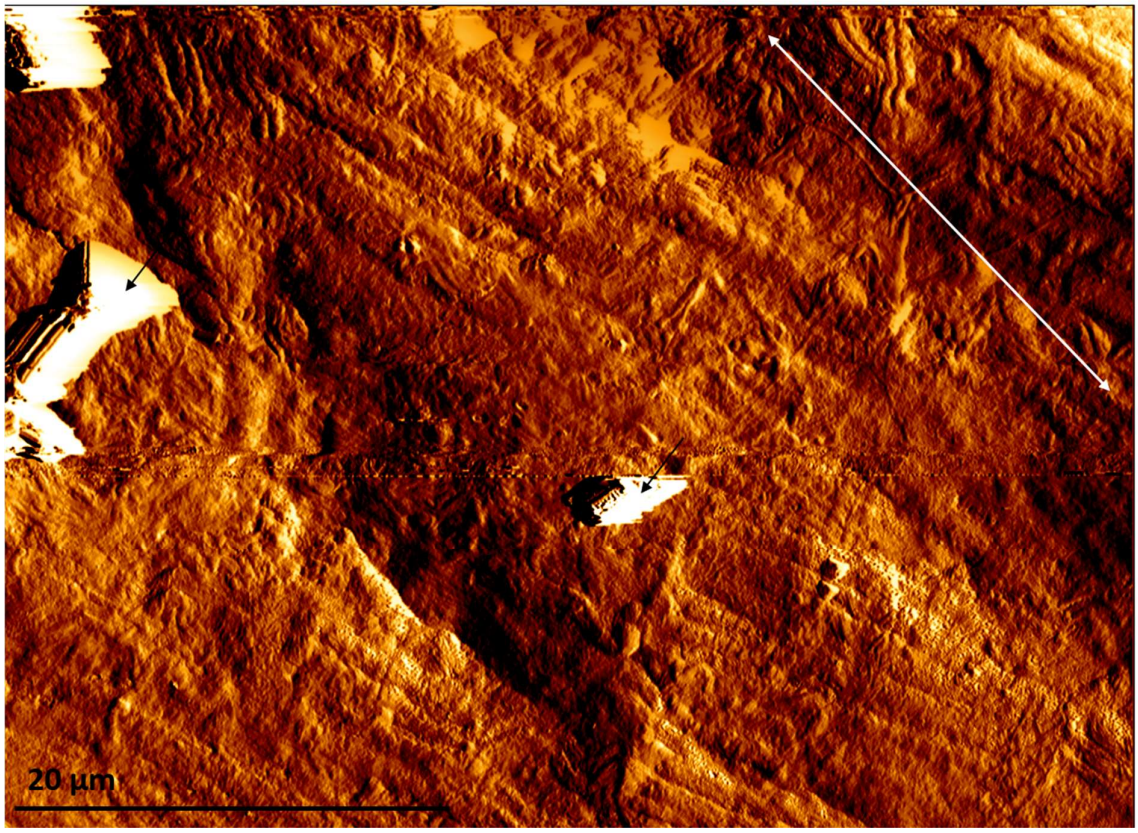


*Figure 4. 11 – 2D AFM image. Black arrows – minor residue. White arrow – longitudinal direction.*

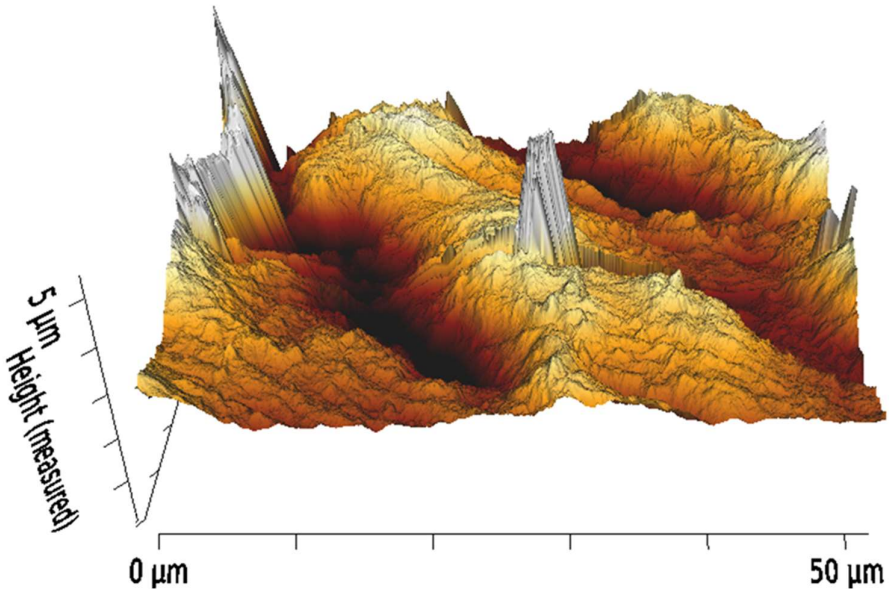

*Figure 4. 12 – 3D reconstruction of AFM image.*

Similar to SEM measurements, when using AFM methods to measure surface roughness there was no significant difference between $Ra_C$ and $Ra_L$ (0.50 ± 0.04 µm and 0.34 ± 0.02 µm; table 4. 2; $p > 0.05$) for each magnification.

### 4.3.4 Reconstructed surfaces

Figures 4. 13 and 4. 14 show reconstructed surfaces using MATLAB (MathWorks, Natick, MA, USA) of the LAD coronary artery from 3D data point clouds outputted by optical microscopy (10× and 100× magnification).

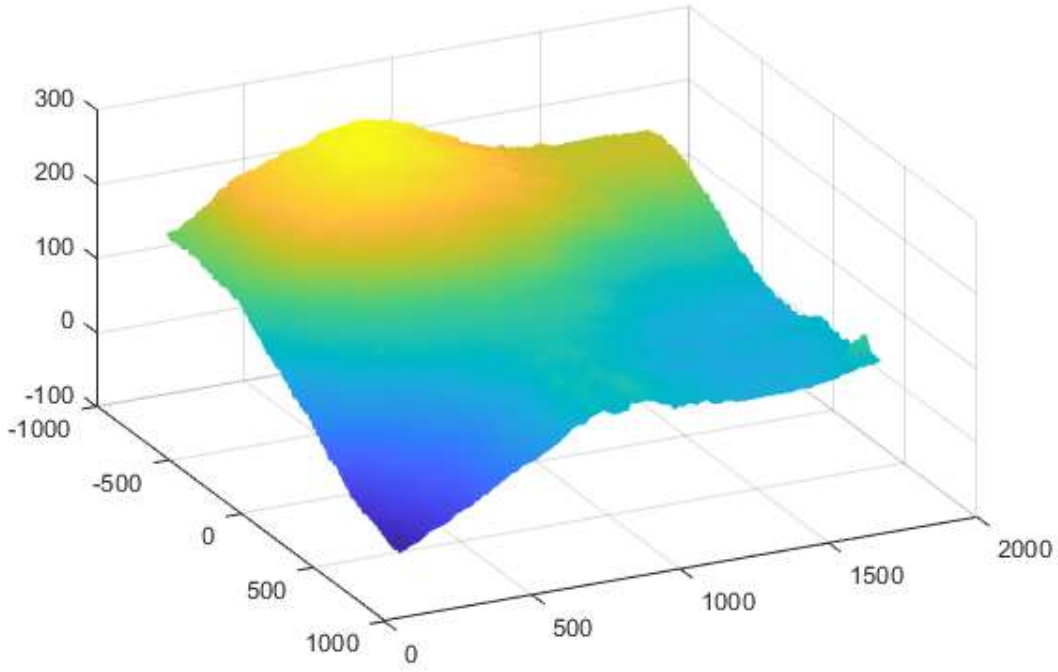


*Figure 4. 13 – Reconstructed mesh of surface from data point cloud collected by optical microscopy, scale in µm (10× magnification).*

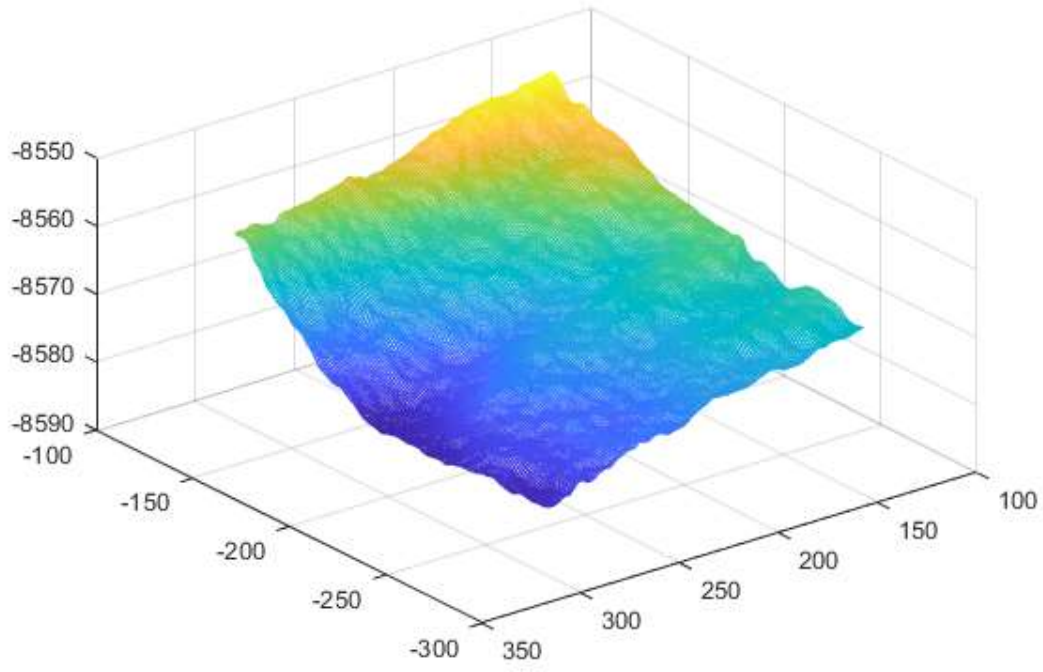


*Figure 4. 14 – Reconstructed mesh of surface from data point cloud collected by optical microscopy, scale in µm (100× magnification).*

### 4.3.5 Multi-scale assessment

In the circumferential direction, when imaged by optical microscopy at low magnification (10×), $Ra_C$ was significantly greater than measurements taken at all magnifications of SEM ($p < 0.05$; figure 4. 16). However, at higher magnifications of optical microscopy (100×), no significant difference was seen in $Ra_C$ compared to when imaging at all magnifications with SEM ($p < 0.05$; figure 4. 16).

Using the AFM imaging method, no significant difference was found between *Ra* measurements for either the optical or SEM imaging method ($p > 0.05$; figure 4. 16 and 4. 18), in both the circumferential and longitudinal directions. At 100× magnification, there was no significant difference in *Ra* between optical microscopy and SEM results ($p > 0.05$; table 4. 2).

In the longitudinal direction, the extreme magnification limits of the non-contact microscopy techniques in this study (10× optical and 2000× SEM), saw a significant difference in $Ra_L$ ($p < 0.05$; figure 4. 18), although between all other magnifications of optical and SEM imaging there was no significant difference in $Ra_L$ ($p > 0.05$).

*Table 4. 2 – Surface roughness values at each magnification and microscopy type. Results are shown as mean ± SD. For: optical microscopy n = 6; SEM n = 5; and AFM n = 3. † Equivalent magnification for AFM, see section 4.3.3.*

| | $Ra_C$ (µm) | $Ra_L$ (µm) | $Ra_{CB}$ (µm) |
|---|---|---|---|
| 10× optical | 0.91 ± 0.27 | 0.35 ± 0.08 | 0.62 ± 0.17 |
| 20× optical | 0.73 ± 0.32 | 0.25 ± 0.07 | 0.50 ± 0.20 |
| 50× optical | 0.69 ± 0.36 | 0.26 ± 0.09 | 0.47 ± 0.22 |
| 100× optical | 0.55 ± 0.27 | 0.26 ± 0.13 | 0.38 ± 0.17 |
| 100× SEM | 0.19 ± 0.08 | 0.19 ± 0.05 | 0.13 ± 0.05 |
| 1000× SEM | 0.27 ± 0.10 | 0.25 ± 0.11 | 0.18 ± 0.06 |
| 2000× SEM | 0.17 ± 0.09 | 0.15 ± 0.05 | 0.12 ± 0.06 |
| 5500× AFM† | 0.50 ± 0.07 | 0.34 ± 0.03 | 0.34 ± 0.04 |

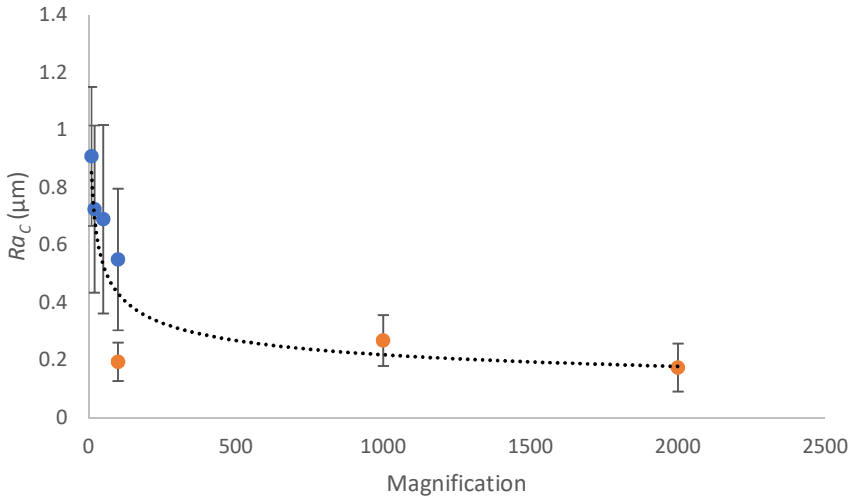


*Figure 4. 15 - Multiscale analysis of circumferential surface roughness for optical (blue) and SEM (orange) at various magnifications (10×, 20×, 50×, 100×, 1000× and 2000×). Error bars are standard deviation. Logarithmic relationship shown.*

$Ra_C$ tended to decrease with magnification, with a strong correlation to a logarithmic relationship noted (figure 4. 15; equation 4. 3; $R^2$ of 0.75; $p < 0.05$). When considering the optical results alone a significant logarithmic relationship with $R^2$ of 0.91 was noted (figure 4. 16; equation 4. 4; $p < 0.05$), with $Ra_C$ decreasing with increase of magnification. Similarly, when assessing $Ra_{C\beta}$ from optical microscopy measurements, a logarithmic relationship was noted with $R^2$ of 0.91 (figure 4. 17; equation 4. 5; $p < 0.05$).

*Equation 4. 3*

$$y = -0.30 \log_{10}(\text{ɱ}) + 1.12$$

*Equation 4. 4*

$$y = -0.32\, log_{10}(\text{ɱ}) + 1.20$$

*Equation 4. 5*

$$y = -0.22\, log_{10}(\text{ɱ}) + 0.82$$

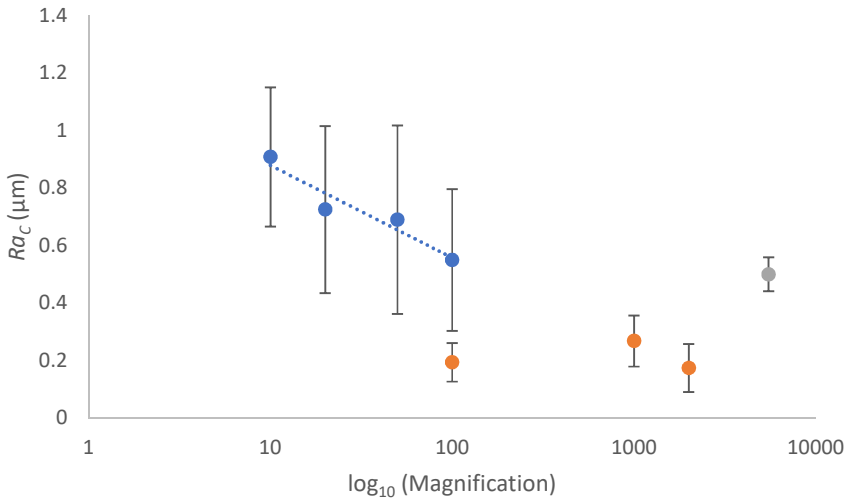


*Figure 4. 16 – Logarithm of magnification levels to base 10 for mean data of $Ra_C$, where error bars are standard deviation (blue = optical, orange = SEM, grey = AFM). Logarithmic relationship shown for optical microscopy.*

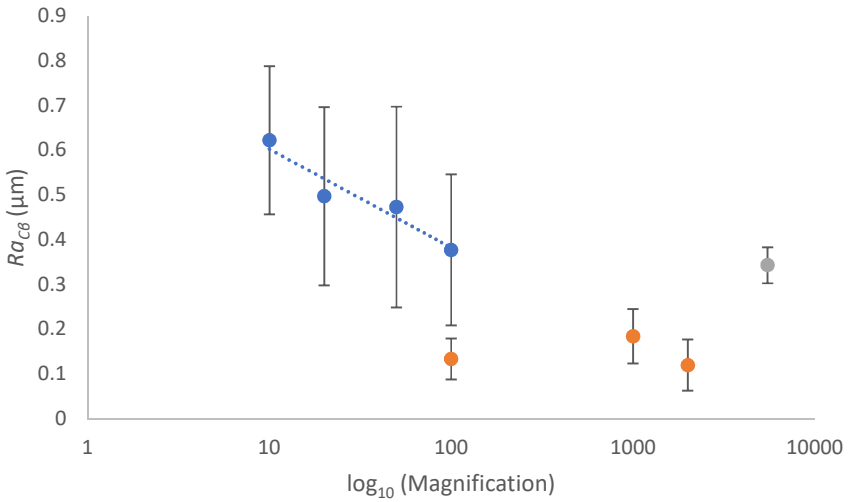


*Figure 4. 17 - Logarithm of magnification levels to base 10 for mean data of $Ra_{CB}$, where error bars are standard deviation (blue = optical, orange = SEM, grey = AFM). Logarithmic relationship shown for optical microscopy.*

Mean and standard deviation for $Ra_L$ across all magnifications measured with all microscopy types are presented in figure 4. 18. $Ra_L$ was calculated with a mean value of 0.26 ± 0.06 µm, with no trend noted.

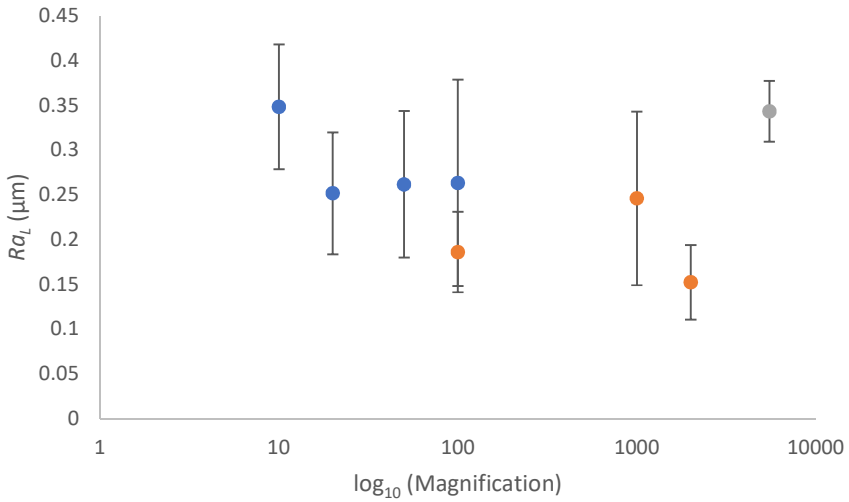


*Figure 4. 18 – Logarithm of magnifications levels to base 10 for mean data of $Ra_L$, where error bars are standard deviation (blue = optical, orange = SEM, grey = AFM). No trend noted.*

## 4.4 DISCUSSION

This study, for the first time, analyses the multiscale surface roughness of LAD coronary artery. Increasing magnification of optical microscopy caused a trend decrease in the circumferential roughness but magnification of all microscopy techniques did not have a significant effect on roughness in the longitudinal direction, with an average value of 0.26 ± 0.06 µm. It highlights the effects both microscopy type and magnification have on surface roughness, and determines that surface roughness of LAD coronary arteries is more sensitive to magnification than microscopy type. Thus, a multiscale characterisation of coronary arteries is essential to understanding the surface roughness at both the micro- and nano-scale.

Despite no significant difference in surface roughness at various magnification levels with optical microscopy, a trend can be seen (figure 4. 15) that $Ra_C$ decreases as

magnification increases. A larger sample size could have been chosen to identify if a significant difference was noted, however, the general trend found in this study would still be valid. The dehydrated specimen surface roughness at 10× optical microscopy presented in chapter 3.5 is greater than that presented in this chapter ($Ra_C$ and $Ra_L$: 1.98 ± 0.26 and 1.07 ± 0.18 μm; 0.91 ± 0.27 and 0.35 ± 0.08 μm), likely due to the change in calibration of microscopy system between chapters (G4 and G5 Alicona Infinite Focus). Within this chapter, at 10× magnification smaller profile lengths of 1.62 mm were assessed, whereas in chapter 3 profile lengths were 2.63 mm. However, the lengths used in both studies are greater than the recommended length (0.8 mm) for the range of *Ra* (0.1 – 2 μm) measured as stated within ISO 4288 (1996). Nonetheless, the underlying trends found in each chapter are not affected by this: $Ra_C$ is significantly greater than $Ra_L$ (noted in both chapter 3 and chapter 4); dehydration increases $Ra_C$ surface roughness (concluded in chapter 3); increase in magnification decreases $Ra_C$ (concluded in chapter 4).

Further investigation into the multi-scale characteristics of the surface roughness of coronary arteries would be beneficial, as *Ra* is dependent on the measurement method used (Ghosh et al., 2013). A correction factor could be determined for scanning electron microscopy, to correct the changes caused by processing to surface roughness at a nano-scale. Processing of tissue resulted in minor residue on the surfaces of samples (Parekh et al., 2014), visible in the 2D and 3D reconstructions of optical microscopy, SEM and AFM images in section 4.3. Environmental scanning electron microscopy (ESEM) would be useful in aiding this, as it would be possible to measure the surface roughness at the various stages of processing, including in a hydrated form, at higher magnifications than possible with an optical microscope (Alhede et al., 2012). Due to lack of conductivity with hydrated samples

when using ESEM, it is not possible to study biological material at high magnification as damage is caused to the surface. Additionally, as shown in this study and elsewhere (Ghosh et al., 2013), using a different microscopy technique can provide varying surface roughness measurements and therefore a comparison between SEM and ESEM may not be appropriate, unless similar magnifications can be achieved.

In this study, no difference was seen in $Ra_L$ across microscopy types. However, optical microscopy consistently provided higher $Ra_C$ results than both SEM and AFM, and even at like-for-like magnification (100×), a significant difference was seen between optical and SEM measurements of $Ra_C$. Although no significant difference was seen in *Ra* for change in magnification of SEM results in this study, Ghosh et al. noted an increase in surface roughness for articular cartilage with increase of magnification of SEM (Ghosh et al., 2013). Ghosh et al. also noted that *Ra* SEM results were higher than those taken with AFM. While Ghosh et al. state that measurements taken with stereoscopic microscopy techniques (SEM) are greater than those measured through contact methods (AFM), they do not assess the surface using other stereoscopic techniques, such as the optical microscopy presented in this study. Although this study did not find a difference in results taken with AFM and SEM, the calculated magnification of AFM, 5500×, was an estimated equivalent. For the purpose of this study it provides an estimate of the multiscale nature of surface roughness measurements investigated. Further, there is no reason that the surface of articular cartilage should present the same multi-scale properties as coronary arteries. Despite not being consistent with the findings within this study, one should note that both studies highlight the importance of using a consistent measurement technique when making comparisons of surface roughness of biological tissue and measuring over multiple scales.

The results of this study are essential for increasing our understanding of coronary artery disease. It is possible to identify disease of biological tissue from surface roughness (Antonio et al., 2012; Girasole et al., 2007; Buys et al., 2013; Peng and Wang, 2013). Scale has been shown as significant when measuring properties of biological materials (Peng and Wang, 2013; LaTorre and Bhushan, 2006). Recent studies have highlighted the capability of using multiscale biological and physiological properties of the heart for computer modelling the circulatory system, emphasising the potential for studying healthy and diseased cardiac systems (Wang et al., 2017). The new generation of biological materials already use multiscale properties to influence cell growth and mechanical properties, creating micro- and nano-porosity within materials (Perez and Mestres, 2016). The results in this study could, therefore, enable the surface of cardiovascular devices to mimic the properties of natural arteries more closely.

Other studies have qualitatively assessed the dehydrated surface of coronary arteries using SEM (Reichlin et al., 2005; Yuan et al., 2016), and they have also investigated the hydrated sample using scanning force microscopy (Reichlin et al., 2005). Further, in diseased arteries, atherosclerotic lesions spiral through the coronary arteries (Wong et al., 2006). Endothelial cells were noted to be aligned longitudinally, as they were within this study, causing ridges along the sample surface (Uchida et al., 2011). However, none of these studies quantified the surface roughness of arteries, or noted a helical arrangement of ridges. However, as these studies did not compare the higher magnifications to lower, as in this study, the helical arrangement may not have been seen due to the sample area assessed. For example, with AFM at 5500× it was not possible to identify this helical arrangement, only when assessing the ridges at a macro- and micro-scale.

Many microscopy techniques allow 3D reconstruction of images as part of software provided by the microscope manufacture. For example, Alicona IF-Laboratory Measurement Module (version 6.1, Alicona UK, Kent, UK), 3D-VIEW software (Hitachi Ltd., Tokyo, Japan), and JPK Data Processing software (JPK Instruments AG, Berlin, Germany), with figures 4. 8, 4. 9, and 4. 12 showing the reconstructed outputs for each, respectively. Figures 4. 13 and 4. 14 present data point clouds that are reconstructed using MATLAB. This demonstrates that a surface can be exported as compatible output file type for computational modelling, and there is the ability to apply the surfaces to CFD models to develop more predictable fluid structure interaction models. The reconstructions presented are for 10× and 100× magnification, validating the feasibility of multi-scale analysis of the effect of surface topography on blood flow. Additionally, it can help to create a standard to which new biomaterials or cell seeded structures can be compared to, with the MATLAB reconstructions allowing a greater flexibility to perform further analyses on the surfaces.

Similar to work presented in chapter 3, a significant difference was seen in surface roughness measured circumferentially and longitudinally with optical microscopy. However, this trend was not noted when measuring surfaces with SEM or AFM, even at identical magnifications across techniques. As magnification is increased, more detail is observed on the surface of LAD coronary arteries (figures 4. 7 and 4. 10 show surface detail with increased magnification for optical microscopy and SEM respectively).

The method described in chapter 3 which described how a correction factor was calculated for the processing of biological tissue to its dehydrated form could be replicated for other microscopy techniques, assessing different fixation chemicals, dehydration

techniques, and the effect of sputter coating on surface roughness. This present study again highlights the significance of using a correction factor when calculating surface roughness of biological tissues that have been processed.

## 4.5 CONCLUSION

A multiscale analysis was performed on the surface roughness of LAD coronary artery. Surface roughness values have been shown to vary when measured at different magnification levels, and *Ra* is also affected by microscopy type. Further, the importance of using a correction factor when assessing surface roughness values of processed biological soft tissue has been reiterated. The following conclusions were made:

- $Ra_C$ was significantly greater when calculated from optical microscopy compared to SEM (0.72 ± 0.31 µm and 0.21 ± 0.09 µm, respectively);
- $Ra_C$ measured by AFM (0.50 ± 0.07 µm) did not significantly differ to results of optical microscopy and SEM;
- $Ra_L$ did not vary with microscopy type or magnification, with an average value of 0.26 ± 0.06 µm;
- For non-contact microscopy methods, *Ra* was significantly greater at lower (10×) compared to higher (2000×) magnification in both the circumferential and longitudinal direction (0.91 ± 0.27 compared to 0.17 ± 0.09, and 0.35 ± 0.08 µm compared to 0.15 ± 0.05 µm, respectively).

# 5 MECHANICAL TESTING

## 5.1 OVERVIEW

Previous studies have investigated the mechanical properties of coronary arteries, as described in chapter 2, table 2. 3. Unlike the conventional testing methods that have characterised the viscoelastic mechanical properties of coronary arteries employed by these studies, dynamic mechanical analysis (DMA) is a dynamic testing method which characterises the viscoelastic properties of a material under physiological parameters. Coronary arteries should be characterised dynamically, as it more closely replicates the dynamic environment that the arteries are found. As the heart beats within the human body, blood flows through the cardiovascular system, causing contraction and expansion in the cardiovascular tissues. This chapter uses DMA to characterise porcine left anterior descending (LAD) coronary arteries.

DMA enables a material's viscoelastic properties to be determined at physiologically relevant frequencies. The viscoelastic properties are characterised by storage and loss moduli (Hukins, Leahy, and Mathias, 1999) which describe the material's ability to store and dissipate energy, respectively. DMA has been applied to soft connective tissues, including articular cartilage (Fulcher, Hukins, and Shepherd, 2009; Sadeghi, Espino, and Shepherd, 2015), intervertebral discs (Gadd and Shepherd, 2011), chordae tendineae (Wilcox, Buchan, and Espino, 2014) and the bladder tumours (Barnes et al., 2016). An advantage of quantifying viscoelastic properties by a dynamic method, over conventional stress relaxation and creep methods, is that the physiological loading conditions can be more closely

replicated (Lawless et al., 2016). For example, it enables frequency-dependent viscoelastic properties to be characterised. The frequency-dependent relationship of dynamic elastic modulus has been investigated through a pressurised model of mice pulmonary arteries (Wang et al., 2013). However, characterisation of frequency-dependency has not been performed for coronary arteries, let alone for their dynamic viscoelasticity.

Mechanical properties of coronary arteries have been shown to alter with disease (Taniguchi et al., 2015). Disease has also been identified in biological tissue through a change in surface roughness, for example in blood cells (Nabel and Braunwald, 2012) and articular cartilage (Bertazzo et al., 2013). In this chapter, to replicate diseased/unhealthy coronary artery, mechanical damage was caused to LAD coronary arteries with extreme physiological loading, imitating mechanical rupture of the artery. The resultant surface roughness was compared to that of healthy tissue, before and after processing of tissue as described in chapter 3. The results presented can aid the development of new biomaterials for cardiovascular applications, and improve our understanding of the effects of coronary artery disease on blood flow.

The aim of this chapter was to measure the relationship between mechanical behaviour and surface roughness of LAD coronary artery. This was achieved by quantitatively measuring the dynamic viscoelasticity of LAD coronary arteries at physiological relevant frequencies. Additionally, a comparison between healthy and damaged coronary artery has been described through the cause of mechanical damage to LAD arteries, and the study of their surface roughness.

The experimental DMA testing within this chapter was delegated to a Masters student who was supervised by the author, with the results provided in data form for this study (Burton, Freij, and Espino, 2017). Design of experiments and all data analysis, determined outcomes, discussion and conclusions are the work of the author. Further, the mechanical damage through uniaxial displacement of tissue was performed by the author.

## 5.2 METHODS

### 5.2.1 Outline

A Bose ElectroForce 3200 testing machine, as seen in figure 5. 1, operated with WinTest DMA software (Bose Corporation, ElectroForce Systems Group, Minnesota, USA) was used to perform mechanical testing on specimens. Specimens either underwent testing for DMA (sections 5.2.3, 5.2.4 and 5.2.5), or for uniaxial overloading (section 5.2.6). For DMA, 3 specimens were used from each sample (proximal, middle and distal); when performing uniaxial overloading to specimens only proximal and distal samples were mechanically tested, with the middle samples kept as control specimens.

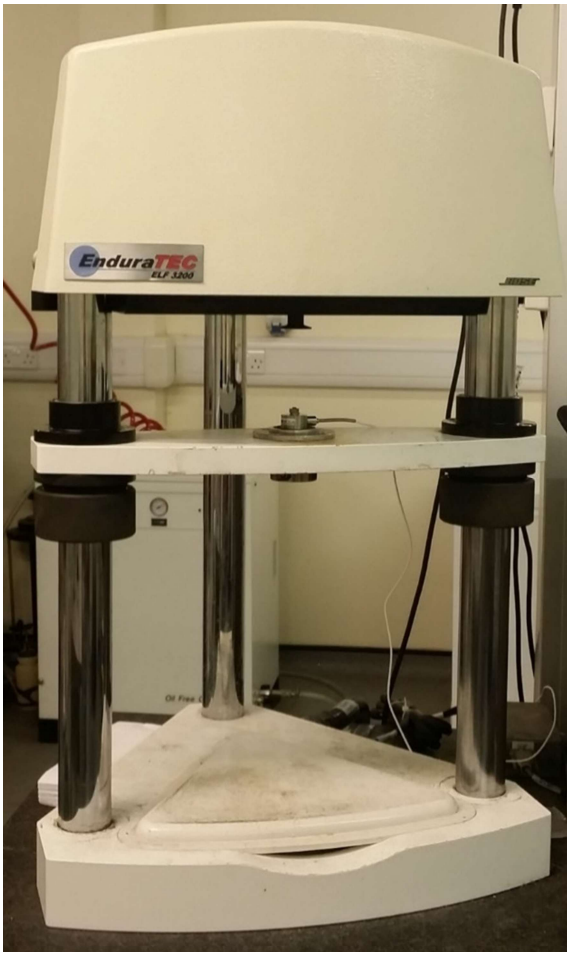


*Figure 5. 1 – Bose ElectroForce 3200 testing machine.*

### 5.2.2 Preparation for mechanical testing

Specimens, dissected as described in chapter 3.2.2, were held in place for testing using grips lined with emery paper (P400 and P60) leaving an un-stretched gauge length (*x*) of 4.57 ± 0.75 mm (figure 5. 2). The gripping method, using emery paper and a compressive force to fix the top and bottom of specimens (seen in figure 5. 3.), is used in other studies for mechanical testing of soft, biological tissue (Millard et al., 2011; Wilcox, Buchan, and Espino, 2014; Barnes et al., 2015).

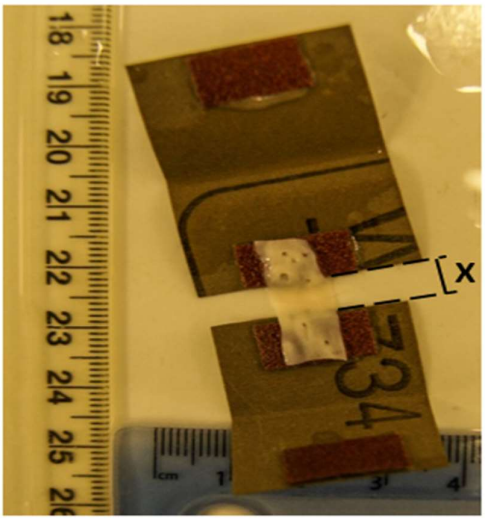


*Figure 5. 2 – Specimen positioned in emery paper, with unstretched gauge length (x).*

Samples were preloaded to a stretched gauge length of 16.63 ± 2.24 mm, measured with a rule between the grippers, removing the slack seen by the specimen due to dissection from surrounding tissue, as the full length of samples before dissection (gauge plus gripping length) was 20 mm. To prevent the specimen from dehydrating, tissue soaked in Ringer's solution was wrapped around the specimen so as not to interfere with the gripping of samples (figure 5. 3).

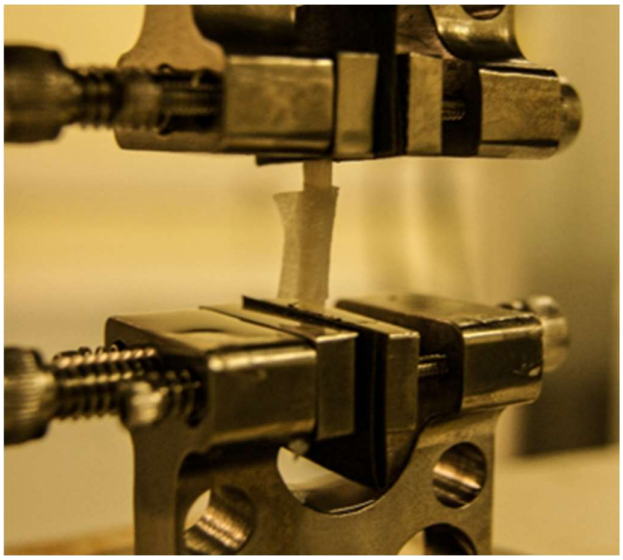

*Figure 5. 3 – Coronary artery specimen gripped in Bose ElectroForce 3200 testing machine, wrapped in tissue paper soaked in Ringer's solution, with preload applied.*

### 5.2.3 Pre-conditioning

Biological tissue requires pre-conditioning to provide repeatable results when performing mechanical testing (Konta, Hugh, and Bett, 2003; Arbab-Zadeh et al., 1999). Before DMA testing, samples were pre-conditioned, consistent with testing of other soft tissues (Kakisis et al., 2005). Pre-conditioning was applied for 10 cycles, as after this the hysteresis loops had converged (figure 5. 4). A longitudinal displacement of 3 mm at a rate of 0.5 mm/s was applied to specimens – the loading rate was associated with the dynamic amplitude (0.5 mm) used in DMA, at a physiological frequency of resting heart rate (1 Hz). 3 mm displacement was found as a common extension length that did not fail proximal, middle or distal samples during preliminary testing, therefore this extension displacement was chosen to not cause damage to specimens during the preconditioning stage.

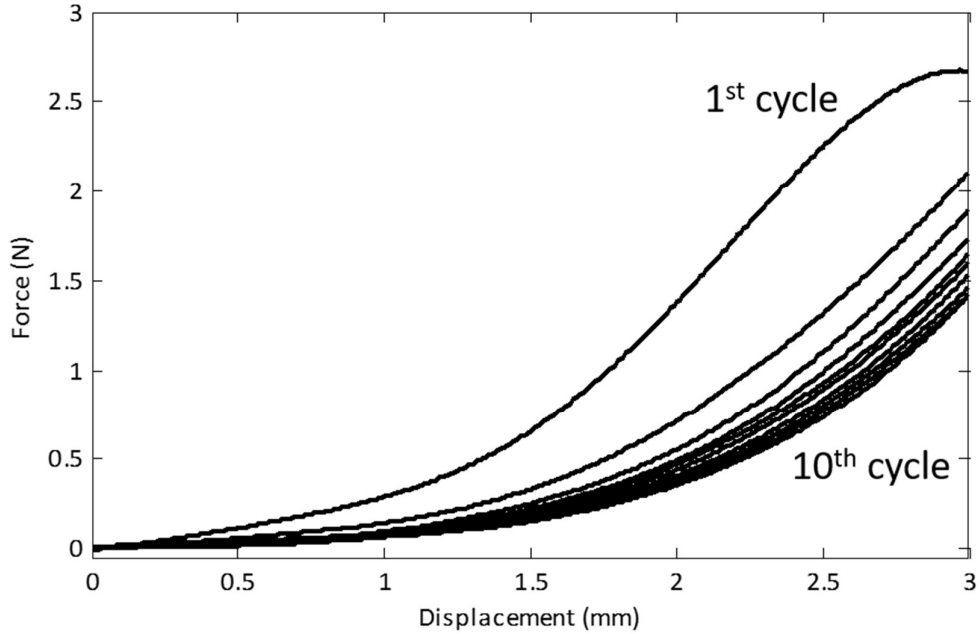


*Figure 5. 4 – Regression lines from first to tenth cycle of testing, converging by the 10th cycle.*

### 5.2.4 Dynamic mechanical analysis protocol

For testing, two sinusoidal displacement loading protocols were used due to the non-linear relationship displayed by coronary arteries, evident by the *J* shaped curve (figure 5. 4). One displacement protocol was between 1-1.5 mm and the other between 1.5-2 mm, i.e. mean displacement of 1.25 mm and 1.75 mm, respectively, covering the linear sections before and after the transition point on the *J* curve. The transition point is estimated as the point on the *J* curve between the linear regions of pre- and post- transitional moduli, noted as the elbow point by Claes et al. (2010). Both loading protocols used a dynamic amplitude of 0.50 mm (i.e. peak to trough). Previous studies measured the median longitudinal displacement of the LAD artery to be 1.36 mm (Arbab-Zadeh et al., 1999). Therefore, tests between 1-1.5 mm correspond to the median longitudinal displacement. The 1.5-2 mm

range, instead, corresponded to coronary arteries undergoing deformation above median values, also reported in literature (Arbab-Zadeh et al., 1999).

Samples were loaded over frequencies ranging from 0.5 Hz up to 10 Hz. Between 0.5-5 Hz, testing frequencies increased at 0.5 Hz intervals; whereas, from 6-10 Hz testing frequencies increased in 1 Hz increments. The frequency range covered bradycardia (<60 beats per minute, bpm; i.e. less than 1 Hz), physiological heart rates (from 1 Hz up to 3 Hz for exercise), and tachycardia (>250 bpm, i.e. 4 Hz) (Hall, 2010). The frequencies up to 10 Hz were calculated from maximum results presented by Kuznetsova *et al*. for the left ventricle, with maximum radial and longitudinal strain rates (3.1 to 4.1 $s^{-1}$ and 1.0 to 1.4 $s^{-1}$) and strain ranges (50 to 70% and 15 to 25%) respectively (Kuznetsova et al., 2008). As the coronary artery is connected to the myocardium which moves in three dimensions, a vector assumption was made for the maximum and minimum strain in longitudinal and radial directions, represented by equations 5. 1 and 5. 2 respectively. Subscript *r* and *l* represent the radial and longitudinal directions respectively.

*Equation 5. 1*

$$\varepsilon = \begin{bmatrix} \varepsilon_r \\ \varepsilon_l \end{bmatrix}$$

*Equation 5. 2*

$$SR = \begin{bmatrix} SR_r \\ SR_l \end{bmatrix}$$

Engineering strain, ε (equation 5. 3) was used to derive strain rate, *SR*, in equation 5. 4. The frequencies, *f*, were calculated as 4.3, 5.8, 6.3 and 8.4 Hz from equation 5. 5, by conversion of units.

*Equation 5. 3*

$$\varepsilon = \frac{L(t) - L_o}{L_o} = \frac{\Delta L}{L_o}$$

*Equation 5. 4*

$$SR = \frac{d\varepsilon}{dt} = \frac{d\,[L(t) - L_o]}{L_o\,dt} = \frac{v(t)}{L_o}$$

*Equation 5. 5*

$$f = \frac{v(t)}{\Delta L}$$

Where $L_o$ is the initial length of specimen, $v(t)$ the instantaneous velocity, and $\Delta L$ is change in length.

### 5.2.5 Viscoelasticity

This method has been used to determine viscoelastic properties of other natural tissue (Barnes et al., 2016; Barnes et al., 2015; Sadeghi, Espino, and Shepherd, 2015). The specimens' displacement and resulting force were measured, and using the WinTest software the complex dynamic stiffness, $k^*$(ratio of force to displacement wave amplitude, following Fourier analysis), and phase angle, $\delta$ (phase lag between force and displacement), were determined. The WinTest software calculates $k^*$ using Fourier analysis to determine the peak load to peak displacement ratio, and $\delta$ by using Fourier analysis to determine the phase difference between load and displacement (Barnes et al., 2015). Using the shape factor for a rectangular test specimen, $S$ (equation 5. 6) (Menard, 2008), the storage ($E'$) and loss ($E''$) moduli were calculated using equations 5. 7 and 5. 8, respectively.

*Equation 5. 6*

$$S = \frac{wt}{l}$$

*Equation 5. 7*

$$E' = \frac{k^* cos(\delta)}{S}$$

*Equation 5. 8*

$$E'' = \frac{k^* sin(\delta)}{S}$$

Here, *w* is width, *t* is thickness and *l* is gauge length of the specimen sample. The width measurement, *w*, was the mean average of $W_1$ and $W_2$ for each sample.

### 5.2.6 Damage

To replicate diseased coronary arteries, damage was inflicted on specimens through uniaxial over-loading of specimens using the Bose ElectroForce 3200 in their longitudinal orientation. 6 porcine hearts (*N* = 6) were dissected as described in chapter 3.2.2. Proximal and distal samples (*n* = 12) were gripped for testing as described in section 5.2.2. Longitudinal movement of the left coronary artery was confirmed in the range of 0.5-6.5 mm (Arbab-Zadeh et al., 1999; Konta, Hugh, and Bett, 2003). Therefore, to ensure damage of the coronary artery, a displacement of 10 mm was chosen, which is was identified during preliminary testing as a displacement where some specimens tore into two pieces. Due to the displacement limitation of the Bose 3200 machine a pre-displacement of 4 mm was required. A ramp rate of 1 mm/s (10% of final displacement per second) was chosen for damage of the artery, maintaining a rate within the resting physiological heart frequency range but at an elevated rate to the preconditioning. The ramp rate was applied to the

specimen until a displacement of 6 mm was reached (therefore a total specimen displacement, including pre-displacement, of 10 mm).

Specimens were imaged with an optical focus variation microscope (G4 Infinite Focus, Alicona UK, Kent, UK) at 10× magnification before and after damage, as described in chapter 3.2.3. Scan area was selected at maximum and minimum *x* and *y* positions on the specimen surface, whilst avoiding the areas that had been gripped during testing. Briefly, from the 3D reconstructed images, *Ra* was measured and the mean of 5 values in the longitudinal ($Ra_L$) and circumferential ($Ra_C$) directions were calculated. Further, specimens were imaged and *Ra* measured after processing involving fixation and dehydration (described in chapter 3.2.4). A correction factor was applied to dehydrated surface roughness values ($Ra_\theta$), calculated by the method explained in chapter 3.2.5. Middle specimens were used as a control for this study, with no damage inflicted.

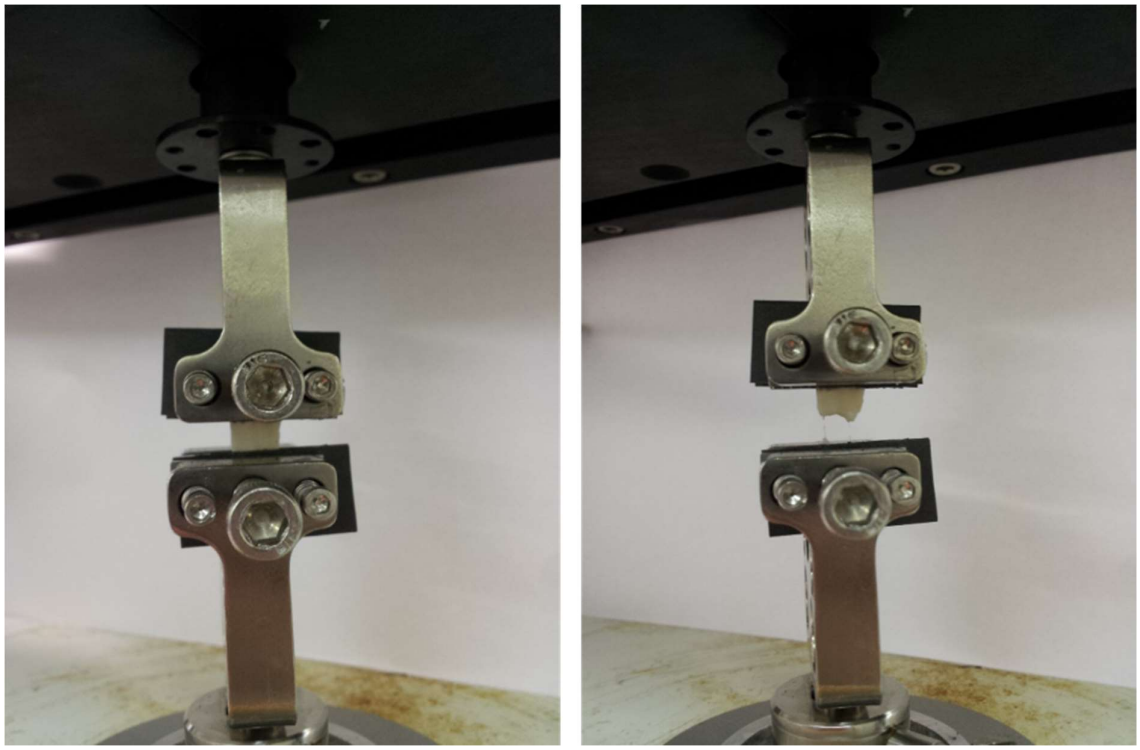

*Figure 5. 5 – LAD coronary artery specimen under uniaxial overloading – (left) before failure and (right) after failure due to tearing of specimen.*

### 5.2.7 Data analysis

In total, *n* = 720 frequency data points were analysed for DMA results (i.e. 8 LAD arteries × 3 specimens per artery × 2 displacements × 15 frequencies). Of these data points, *n* = 35 points were not recorded by the WinTest software due to machine error during testing.

Pierce's criterion was applied across the frequencies to highlight possible outlier data. For the *n* = 84 points highlighted, data was re-analysed manually. Of these points, *n* = 15 data points saw irregular noise across the sample wave. Where possible the wave was 'smoothed' to remove noise, but for *n* = 4 data points the noise to signal ratio remained large and prevented analysis, i.e. these four data points were deleted. Although the remaining *n* = 69 data points had high levels of background noise, manual analysis

demonstrated that a sample wave suitable for analysis was available. The larger than normal disparity was treated as being due to natural variation seen in biological tissues. Therefore, a total of $n$ = 681 (out of 720) data points were used for data analysis.

Data analysis was performed using SigmaPlot 12.0 (Systat Software Inc., London, UK). All data sets were assessed for normal distribution using a Shapiro-Wilk normality test. If data sets were normally distributed (i.e. $p > 0.05$), significance was assessed ($p < 0.05$) for the null hypothesis using a paired $t$-test. If data was not normally distributed, a Wilcoxon Signed Rank test was used (i.e. a paired non-parametric test; $p < 0.05$ for significance) (Bland, 2000; Reilly, 2015).

Unless otherwise stated, the paired comparisons used moduli results at 1 Hz, with an extension range of 1-1.5 mm. Paired comparisons included the following:

- moduli frequency-dependency, i.e. 1 Hz vs 10 Hz (1 Hz chosen as physiological comparison to resting heart rate, and 10 Hz, the upper limit of testing range, chosen as extreme loading condition of heart);
- variation of moduli between proximal and distal sections;
- extension range influence on moduli, i.e. 1-1.5 mm vs 1.5-2 mm;

The surface roughness ($Ra$) of LAD coronary arteries has been discussed in chapter 3. Regression analysis was performed for both the $Ra_C$ and $Ra_L$ against storage and loss moduli. Circumferential surface roughness values were evaluated for both $Ra_C$ and $Ra_{C6}$. Regression analysis was also performed for moduli against frequency.

The final analysis of data was performed using Minitab Statistical Software (Minitab 17.0, Minitab Inc, State College, PA, USA) on the surface roughness results of the damaged specimens. A student's *t-test* was performed to assess the significance ($p < 0.05$) under the null hypothesis of healthy (middle specimens) and damaged (proximal and distal specimens) coronary arteries. Additionally, a paired *t-test* was used to analyse *Ra* of proximal and distal specimens before and after damage to assess significance ($p < 0.05$), and to compare *Ra* of damaged specimens before and after processing, similar to chapter 4 (i.e. in their hydrated and dehydrated forms).

## 5.3 RESULTS

### 5.3.1 Storage and loss general results

The range of storage moduli varied from 14.47 MPa to 25.82 MPa, whereas loss varied from 1.57 MPa to 2.71 MPa (table 5. 1). The storage modulus was an order of magnitude greater than the loss modulus.

Between 1 Hz and 10 Hz, there was a statistically significant difference in the storage modulus ($p < 0.05$). The modulus at 1 Hz was consistently higher than at 10 Hz, on average by 4.37 MPa (figure 5. 6). This was the case at all positions along the LAD artery (i.e. proximal, middle and distal). Figures 5. 7 - 5. 9 show results for individual specimens, demonstrating that the trend was consistent across samples and that it was not skewed by any given individual outlier sample. A linear relationship was found (figure 5. 10), defined by equation 5. 9.

*Table 5. 1 - Storage and loss moduli of LAD coronary arteries at 1-1.5 mm extension. Note, SD: Standard deviation. Where E' is storage, and E'' loss, moduli.*

| | Proximal | | | | Middle | | | | Distal | | | |
|---|---|---|---|---|---|---|---|---|---|---|---|---|
| Frequency (Hz) | *E'* (MPa) | | *E"* (MPa) | | *E'* (MPa) | | *E"* (MPa) | | *E'* (MPa) | | *E"* (MPa) | |
| | Mean | SD | Mean | SD | Mean | SD | Mean | SD | Mean | SD | Mean | SD |
| 0.5 | 17.27 | 11.00 | 1.80 | 0.99 | 22.83 | 6.13 | 2.23 | 0.49 | 25.67 | 8.85 | 2.28 | 0.82 |
| 1 | 16.99 | 9.74 | 1.76 | 0.83 | 22.78 | 5.74 | 2.16 | 0.51 | 25.25 | 8.55 | 2.26 | 0.78 |
| 1.5 | 16.78 | 9.66 | 1.69 | 0.80 | 22.64 | 5.74 | 2.14 | 0.52 | 25.03 | 8.37 | 2.27 | 0.80 |
| 2 | 16.64 | 9.66 | 1.68 | 0.72 | 22.52 | 5.67 | 2.16 | 0.52 | 24.81 | 8.29 | 2.26 | 0.86 |
| 2.5 | 16.49 | 9.55 | 1.62 | 0.79 | 22.53 | 5.74 | 2.14 | 0.48 | 24.70 | 8.46 | 2.40 | 0.91 |
| 3 | 16.35 | 9.48 | 1.64 | 0.76 | 22.13 | 5.88 | 2.11 | 0.46 | 25.82 | 8.51 | 2.38 | 0.87 |
| 3.5 | 16.25 | 9.46 | 1.62 | 0.76 | 22.01 | 5.71 | 2.15 | 0.50 | 25.56 | 8.55 | 2.33 | 0.82 |
| 4 | 16.14 | 9.41 | 1.59 | 0.65 | 21.79 | 5.84 | 2.15 | 0.57 | 25.26 | 8.35 | 2.41 | 0.93 |
| 4.5 | 16.03 | 9.37 | 1.66 | 0.74 | 21.69 | 5.67 | 2.12 | 0.50 | 25.01 | 8.36 | 2.34 | 0.84 |
| 5 | 15.89 | 9.37 | 1.57 | 0.71 | 21.43 | 5.69 | 2.22 | 0.58 | 24.58 | 8.30 | 2.41 | 0.93 |
| 6 | 15.65 | 9.40 | 1.68 | 0.77 | 20.96 | 5.66 | 2.31 | 0.52 | 22.76 | 7.85 | 2.56 | 0.93 |
| 7 | 15.43 | 9.38 | 1.70 | 0.76 | 20.59 | 5.64 | 2.32 | 0.59 | 23.23 | 7.98 | 2.71 | 1.07 |
| 8 | 15.09 | 9.43 | 1.76 | 0.85 | 19.74 | 5.77 | 2.34 | 0.57 | 22.19 | 7.77 | 2.60 | 0.93 |
| 9 | 14.84 | 9.36 | 1.78 | 0.80 | 19.35 | 5.50 | 2.34 | 0.54 | 21.29 | 7.67 | 2.61 | 0.90 |
| 10 | 14.47 | 9.35 | 1.73 | 0.76 | 18.47 | 5.57 | 2.23 | 0.49 | 19.99 | 7.31 | 2.28 | 0.82 |

*Equation 5. 9*

$$E' = mf + c$$

Here, *E'* is the storage modulus, *f* is frequency, and *m* and *c* are constants (table 5. 2).

*Table 5. 2 - Regression constants, m and c, for the dependency of the storage modulus with frequency for average mean of all samples at different positions along LAD artery ($p < 0.05$ for all trends).*

| **Position** | ***m* (MPa.s)** | ***c* (MPa)** | $R^2$ |
|---|---|---|---|
| Proximal | -0.27 | 17.24 | 0.99 |
| Middle | -0.45 | 23.45 | 0.97 |
| Distal | -0.54 | 26.52 | 0.82 |

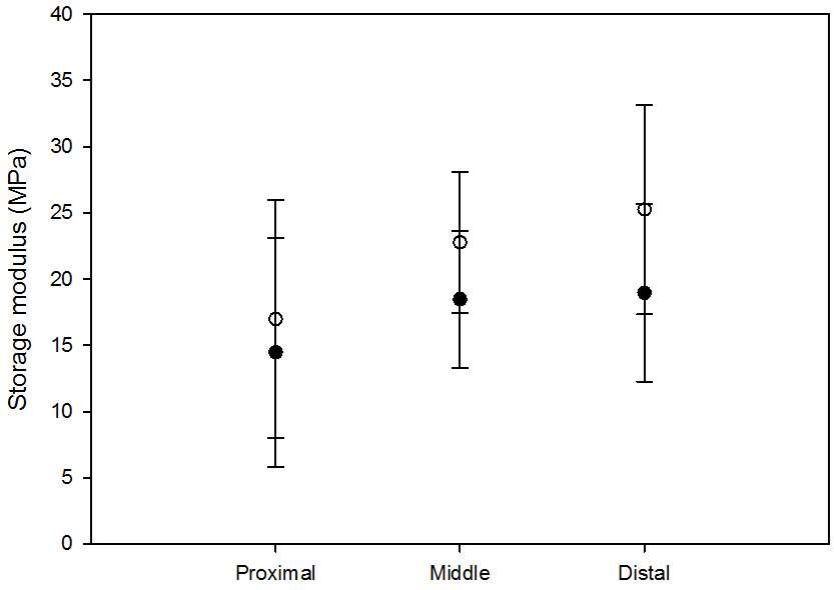


*Figure 5. 6 - Storage modulus comparison at 1 (white dots) and 10 Hz (black dots) for averaged values of proximal, middle and distal specimens. Error bars represent 95% confidence intervals where n = 7.*

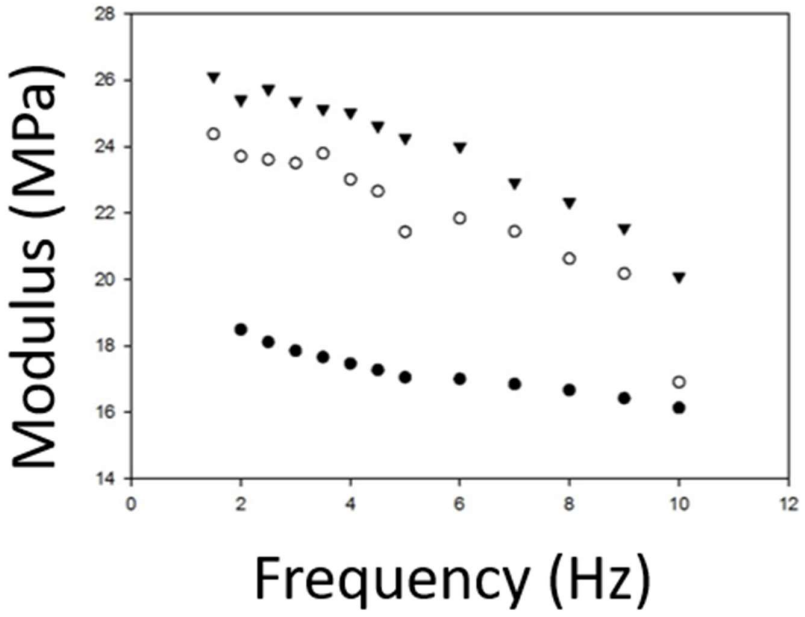


*Figure 5. 7 - Frequency dependency of storage moduli for individual samples; for a total of three specimens (n = 3). (Black dots for proximal, white dots for middle, black triangles for distal samples).*

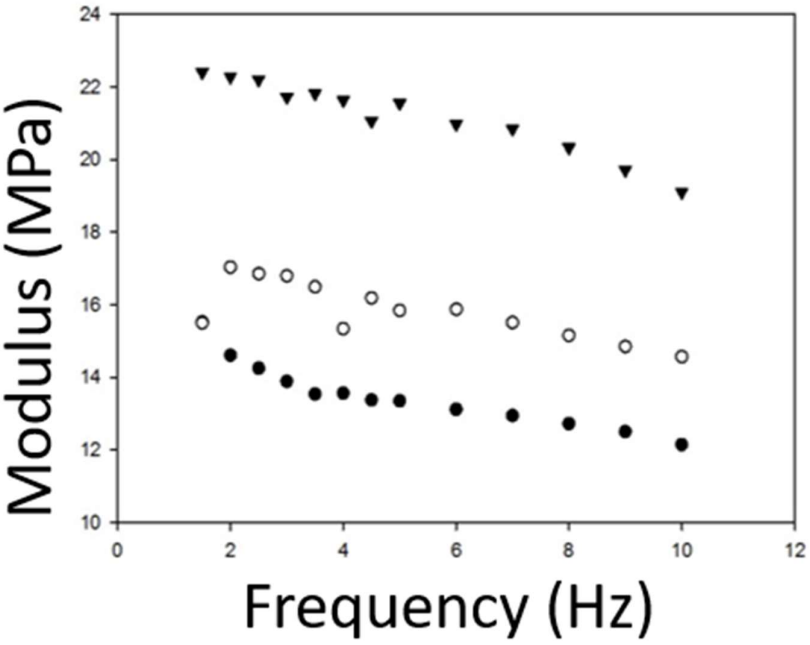


*Figure 5. 8 - Frequency dependency of storage moduli for individual samples; for a total of three specimens (n = 3). (Black dots for proximal, white dots for middle, black triangles for distal samples).*

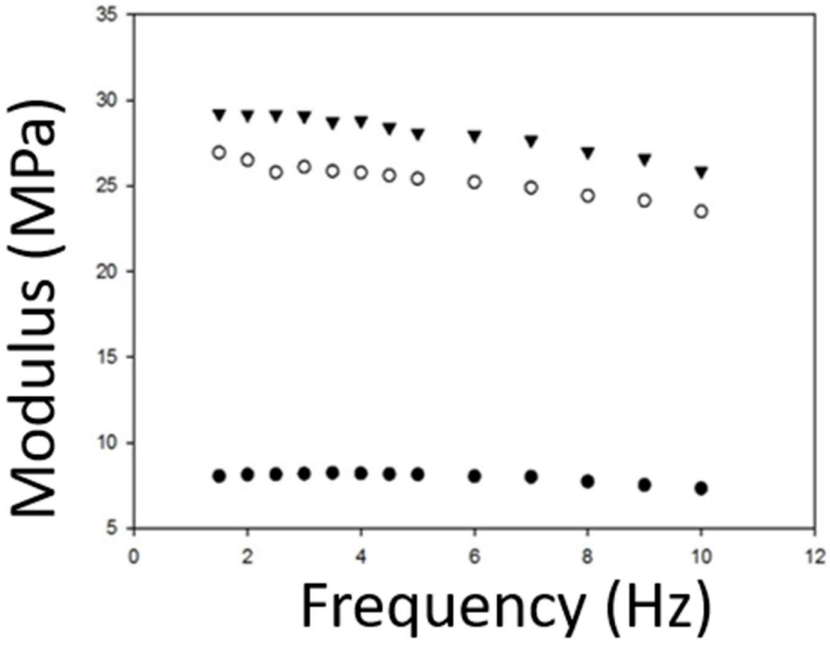


*Figure 5. 9 - Frequency dependency of storage moduli for individual samples; for a total of three specimens (n = 3). (Black dots for proximal, white dots for middle, black triangles for distal samples).*

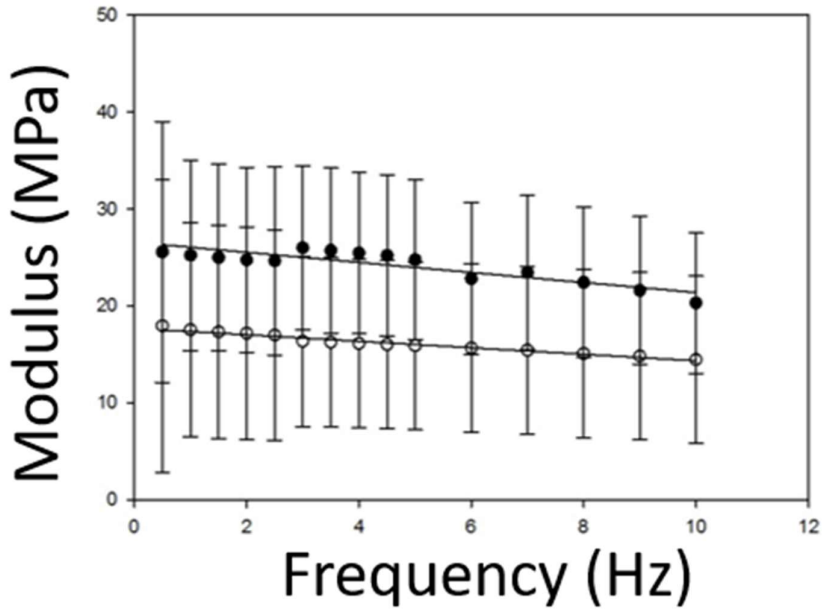


*Figure 5. 10 - Frequency-dependency of proximal (white dots) and distal (black dots) positions along LAD artery – Mean storage moduli. Linear regression lines showing frequency dependent relationship. Error bars represent 95% confidence intervals, where at: 1 Hz, n = 5; 1-2.5 Hz, n = 6; 3-10 Hz, n = 7.*

The loss modulus was found to be frequency-independent. No significant differences were found for the loss modulus at 1 Hz and 10 Hz ($p > 0.05$). The loss modulus was found to have a mean (± standard deviation) of 1.68 ± 0.07 MPa, 2.21 ± 0.09 MPa and 2.41 ± 0.14 MPa for the proximal, middle and distal samples respectively. Individual loss specimen results are provided in figures 5. 11 - 5. 13; average proximal and distal values shown in figure 5. 14.

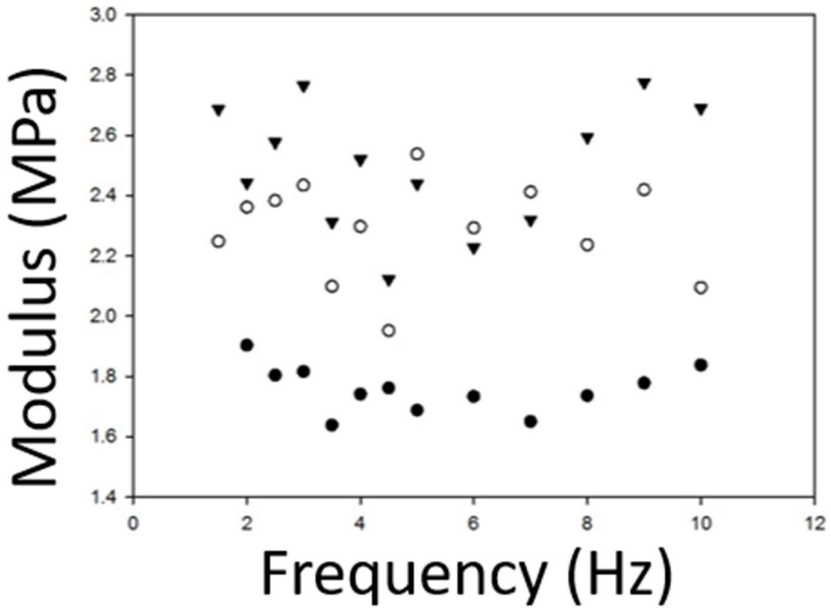


*Figure 5. 11 - Frequency dependency of loss moduli for individual samples; for a total of three specimens (n = 3). (Black dots for proximal, white dots for middle, black triangles for distal samples).*

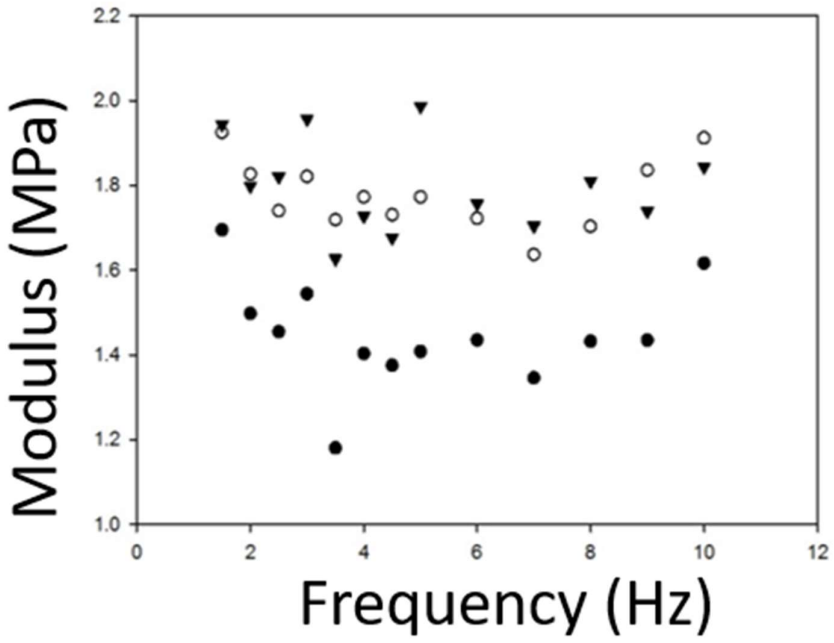


*Figure 5. 12 - Frequency dependency of loss moduli for individual samples; for a total of three specimens (n = 3). (Black dots for proximal, white dots for middle, black triangles for distal samples).*

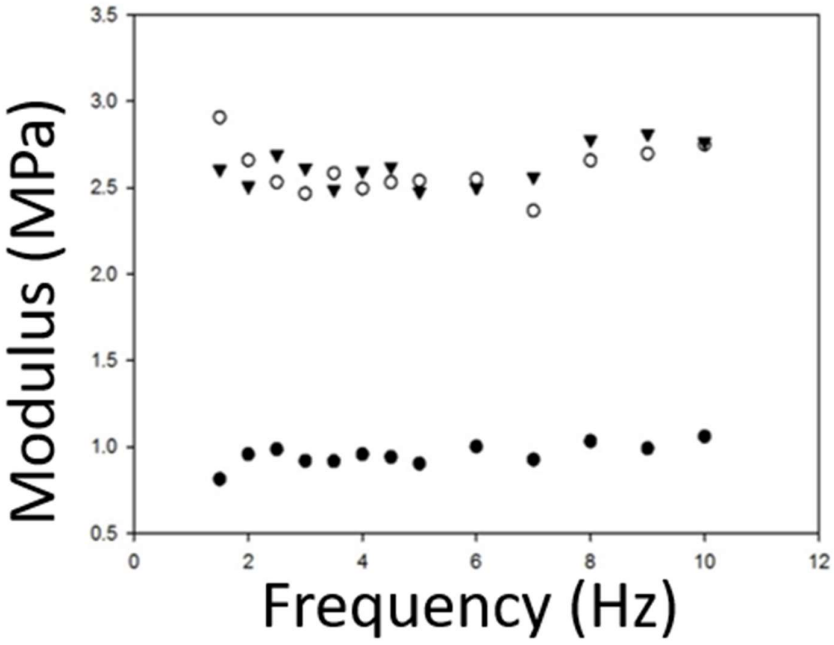


*Figure 5. 13 - Frequency dependency of loss moduli for individual samples; for a total of three specimens (n = 3). (Black dots for proximal, white dots for middle, black triangles for distal samples).*

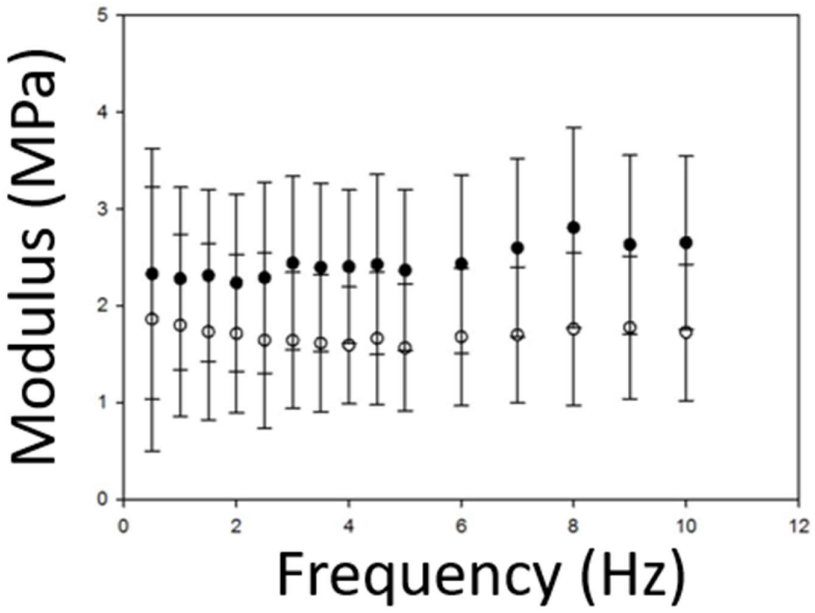


*Figure 5. 14 - Frequency-dependency of proximal (white dots) and distal (black dots) positions along LAD artery – Mean loss moduli. Linear regression lines showing frequency dependent relationship. Error bars represent 95% confidence intervals, where at: 1 Hz, n = 5; 1-2.5 Hz, n = 6; 3-10 Hz, n = 7.*

### 5.3.2 Proximal vs Distal

Storage modulus did not vary along the LAD artery. Although the proximal mean storage modulus was lower than the distal modulus on average by 8 MPa, no significant difference was found between the storage modulus of proximal and distal samples; mean ± standard deviation: 16.99 ± 9.74 MPa (proximal), 25.25 ± 8.55 MPa (distal) ($p > 0.05$). This can be interpreted in figure 5. 6 as a difference in the means but with overlap of confidence intervals (due to natural variability).

The loss modulus did not vary along the LAD artery. No significant difference was found between the loss modulus of proximal and distal samples ($p > 0.05$). However, the

proximal mean loss modulus was lower than the distal modulus on average by 0.74 MPa, with extensive overlap of 95% confidence intervals (figure 5. 14).

### 5.3.3 Extension Ranges

Overall results for 1.5-2 mm extension are displayed in table 5. 3. No statistical significance was seen for the storage and loss moduli between extensions of 1-1.5 mm and 1.5-2 mm. At 1 Hz, testing samples between 1.5-2 mm led to an average storage modulus of 19.71 MPa, 25.46 MPa and 25.87 MPa for proximal, middle and distal samples, respectively (figure 5. 15). These storage moduli were not significantly different to the storage moduli when measured at 1-1.5 mm of extension (16.99 MPa, 22.78 MPa and 25.25 MPa, respectively; $p > 0.05$, figure 5. 15).

At 1 Hz, testing samples between 1.5-2 mm led to an average loss modulus of 2.01 MPa, 2.50 MPa and 2.35 MPa for proximal, middle and distal samples, respectively (figure 5. 16). These loss moduli were not significantly different to the loss moduli when measured at 1-1.5 mm of extension (1.76 MPa, 2.23 MPa and 2.28 MPa, respectively; $p > 0.05$, figure 5. 16).

*Table 5. 3 - Storage and loss moduli of LAD coronary arteries at 1.5-2 mm extension. Note, SD: Standard deviation. Where E' is storage, and E'' loss, moduli.*

| | Proximal | | | | Middle | | | | Distal | | | |
|---|---|---|---|---|---|---|---|---|---|---|---|---|
| Frequency (Hz) | *E'* (MPa) | | *E"* (MPa) | | *E'* (MPa) | | *E"* (MPa) | | *E'* (MPa) | | *E"* (MPa) | |
| | Mean | SD | Mean | SD | Mean | SD | Mean | SD | Mean | SD | Mean | SD |
| 0.5 | 20.28 | 11.80 | 2.15 | 1.10 | 25.88 | 7.34 | 2.51 | 0.69 | 26.47 | 9.37 | 2.53 | 0.89 |
| 1 | 19.71 | 10.46 | 2.01 | 0.96 | 25.46 | 7.22 | 2.50 | 0.70 | 25.87 | 8.97 | 2.35 | 0.81 |
| 1.5 | 19.35 | 10.26 | 1.92 | 0.86 | 25.35 | 7.18 | 2.38 | 0.66 | 25.74 | 8.88 | 2.32 | 0.85 |
| 2 | 19.20 | 10.31 | 1.86 | 0.87 | 25.26 | 7.16 | 2.26 | 0.73 | 25.45 | 8.82 | 2.24 | 0.85 |
| 2.5 | 19.10 | 10.23 | 1.87 | 0.89 | 25.09 | 7.11 | 2.43 | 0.66 | 25.10 | 8.78 | 2.25 | 0.73 |
| 3 | 19.72 | 10.91 | 1.92 | 0.87 | 24.98 | 7.05 | 2.33 | 0.59 | 26.58 | 9.28 | 2.50 | 0.93 |
| 3.5 | 20.13 | 10.41 | 1.95 | 0.82 | 24.85 | 7.05 | 2.35 | 0.65 | 26.36 | 9.18 | 2.42 | 0.92 |
| 4 | 19.52 | 10.87 | 1.96 | 0.80 | 24.44 | 6.89 | 2.31 | 0.53 | 26.18 | 9.24 | 2.70 | 1.30 |
| 4.5 | 18.58 | 10.14 | 1.88 | 0.80 | 24.37 | 6.93 | 2.36 | 0.60 | 25.76 | 9.06 | 2.43 | 0.92 |
| 5 | 18.45 | 10.12 | 1.79 | 0.77 | 24.13 | 6.89 | 2.29 | 0.57 | 25.45 | 9.05 | 2.41 | 0.90 |
| 6 | 18.24 | 10.12 | 1.91 | 0.83 | 23.71 | 6.85 | 2.49 | 0.64 | 24.66 | 8.87 | 2.49 | 0.91 |
| 7 | 17.96 | 10.09 | 1.92 | 0.80 | 23.21 | 6.87 | 2.54 | 0.63 | 23.93 | 8.75 | 2.58 | 0.97 |
| 8 | 17.62 | 10.18 | 1.97 | 0.86 | 22.68 | 6.75 | 2.64 | 0.79 | 23.03 | 8.70 | 2.57 | 1.07 |
| 9 | 17.45 | 10.06 | 2.03 | 0.83 | 22.11 | 6.68 | 2.56 | 0.68 | 22.07 | 8.36 | 2.67 | 0.95 |
| 10 | 17.02 | 10.05 | 2.01 | 0.78 | 21.17 | 6.54 | 2.53 | 0.61 | 20.82 | 8.13 | 2.72 | 1.00 |

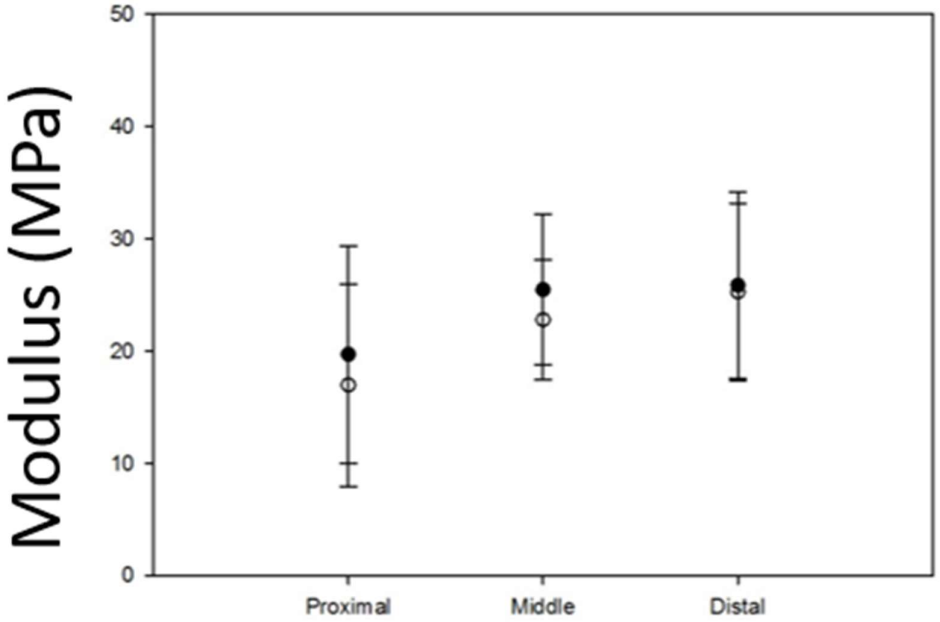


*Figure 5. 15 - Comparison of viscoelastic properties at 1 Hz for different extension ranges for averaged values of proximal, middle and distal samples – Storage modulus. (White dots for 1-1.5 mm, black dots for 1.5-2 mm). Error bars represent 95% confidence intervals where n = 7.*

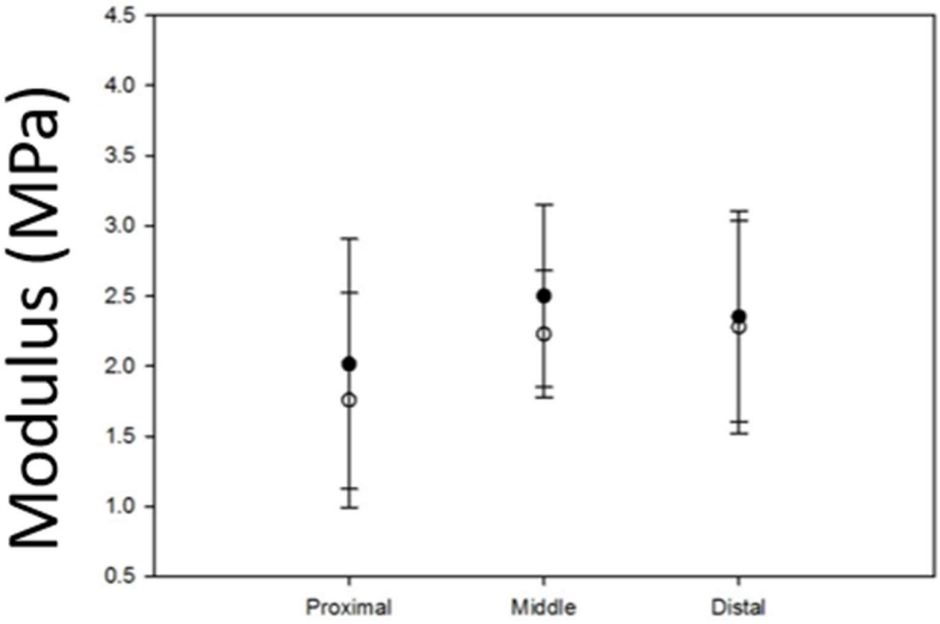


*Figure 5. 16 - Comparison of viscoelastic properties at 1 Hz for different extension ranges for averaged values of proximal, middle and distal samples – Loss modulus. (White dots for 1-1.5 mm, black dots for 1.5-2 mm). Error bars represent 95% confidence intervals where n = 7.*

### 5.3.4 Regression analysis between surface roughness and viscoelastic properties

Viscoelastic properties and surface roughness were not correlated to each other. For example, at 1 Hz, no correlation was found between $Ra_C$ and either the storage or the loss moduli. This was the case for both $Ra_C$ and $Ra_{C\beta}$ (figures 5. 17 and 5. 18). Likewise, $Ra_L$ was not correlated to either storage or loss moduli (figure 5. 19).

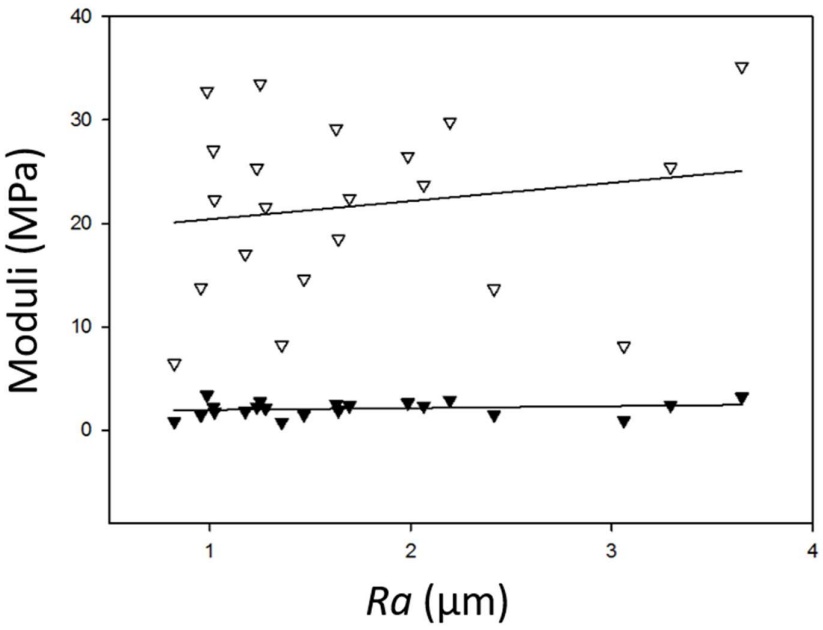


*Figure 5. 17 - Regression analysis between $Ra_C$ data against moduli for 1 Hz and 1-1.5 mm extension range (White triangles for storage, black triangles for loss moduli; $R^2 < 0.05$, $p > 0.05$).*

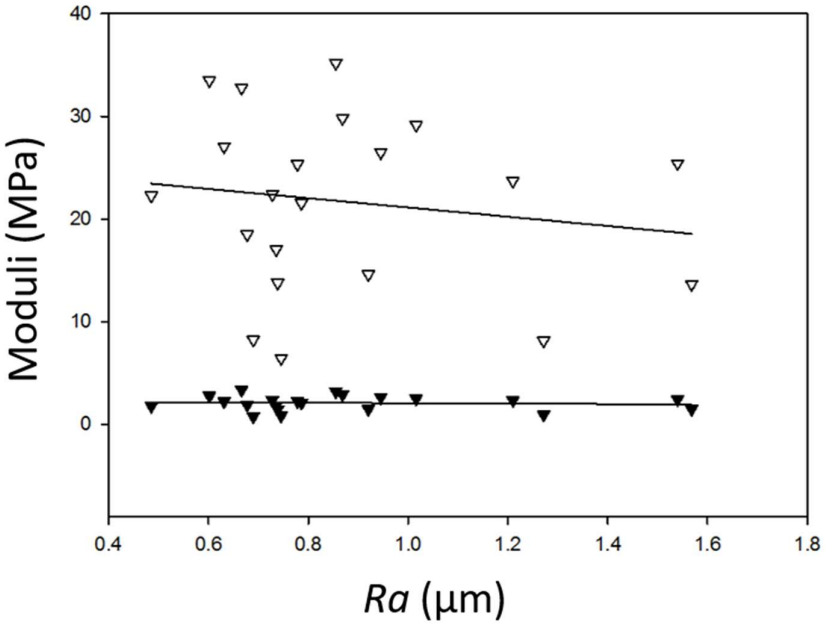


*Figure 5. 18 - Regression analysis between $Ra_{C6}$ data against moduli for 1 Hz and 1-1.5 mm extension range (White triangles for storage, black triangles for loss moduli; $R^2 < 0.05$, $p > 0.05$).*

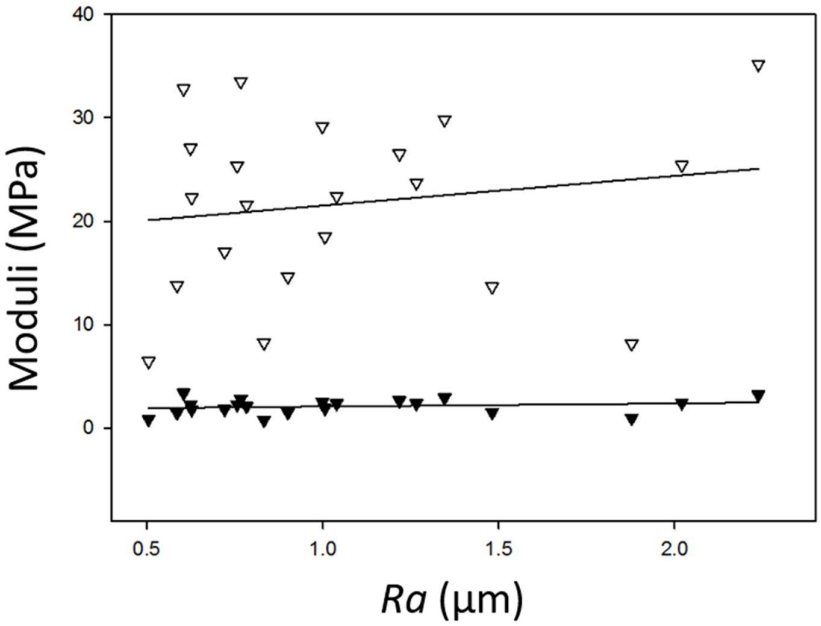


*Figure 5. 19 - Regression analysis between $Ra_L$ data against moduli for 1 Hz and 1-1.5 mm extension range (White triangles for storage, black triangles for loss moduli; $R^2 < 0.05$, $p > 0.05$).*

### 5.3.5 Damaged vs healthy LAD coronary arteries

A significant difference was seen between $Ra_C$ and $Ra_L$ ($p < 0.05$), with surface roughness in the circumferential direction found to be greater than in the longitudinal direction (table 5. 4). No significant difference ($p > 0.05$) was seen for surface roughness between the hydrated healthy control specimens ($Ra_C$ and $Ra_L$; 1.28 ± 0.37 and 1.00 ± 0.41 µm respectively) and hydrated damaged proximal and distal LAD coronary arteries (table 5. 4). Additionally, a paired comparison of surface roughness for hydrated (proximal and distal) samples, before and after damage, revealed no significant difference ($p > 0.05$; table 5. 4). Individual specimen results are shown for the $Ra_L$ in figure 5. 20, and although $Ra_L$ tends to be greater after damage (figure 5. 23), no significant difference was noted for hydrated specimens, even when the anomalous first result is removed (figure 5. 20). Images of the surface in hydrated and dehydrated form of both the damaged and undamaged specimens are shown in figure 5. 21, with no visible difference between each surface.

*Table 5. 4 – Mean average result ± standard deviation of proximal and distal samples (N = 6; n = 12) for surface roughness of healthy and damaged LAD coronary arteries, in hydrated and dehydrated state. † indicates result is significantly greater than both their hydrated damaged and healthy values.*

| | $Ra_C$ (µm) | $Ra_L$ (µm) |
|---|---|---|
| Hydrated healthy | 1.46 ± 0.38 | 0.91 ± 0.26 |
| Hydrated damaged | 1.47 ± 0.39 | 1.05 ± 0.25 |
| Dehydrated damaged | 1.95 ± 0.56† | 1.28 ± 0.33† |

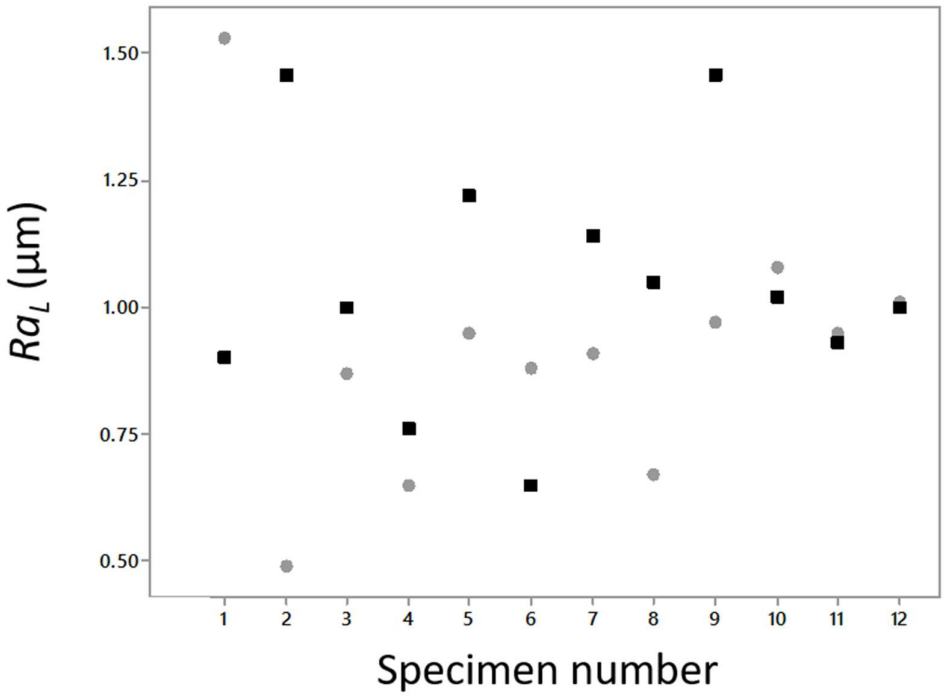


*Figure 5. 20 – $Ra_L$ for individual proximal (n = 6) and distal (n = 6) specimens. Grey circles – before damage (healthy); black squares – after damage. All samples in hydrated form.*

The control undamaged specimens had a significantly greater $Ra_C$ after processing ($p < 0.05$; 1.91 ± 0.33 µm compared to 1.28 ± 0.37 µm), however $Ra_L$ was not significantly different ($p > 0.05$; 1.07 ± 0.20 µm and 1.00 ± 0.41 µm), consistent with previous findings that dehydration significantly alters the surface roughness in the circumferential but not longitudinal direction (chapter 3). However, in both the circumferential and longitudinal direction of dehydrated damaged specimens, the surface roughness was significantly greater ($p < 0.05$; table 5. 4) than the hydrated damaged specimens (figures 5. 22 and 5. 23).

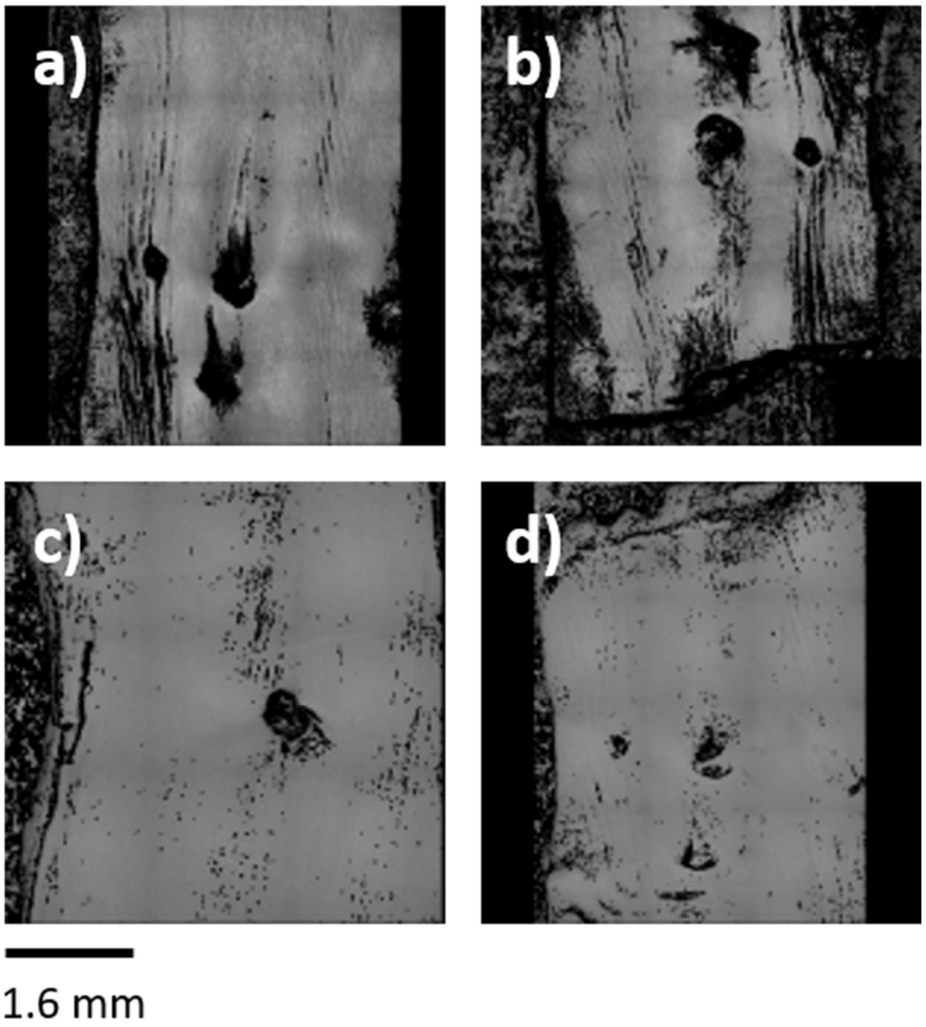


*Figure 5. 21 – 2D optical images of surfaces: a) undamaged hydrated; b) damaged hydrated; c) undamaged dehydrated; d) damaged dehydrated.*

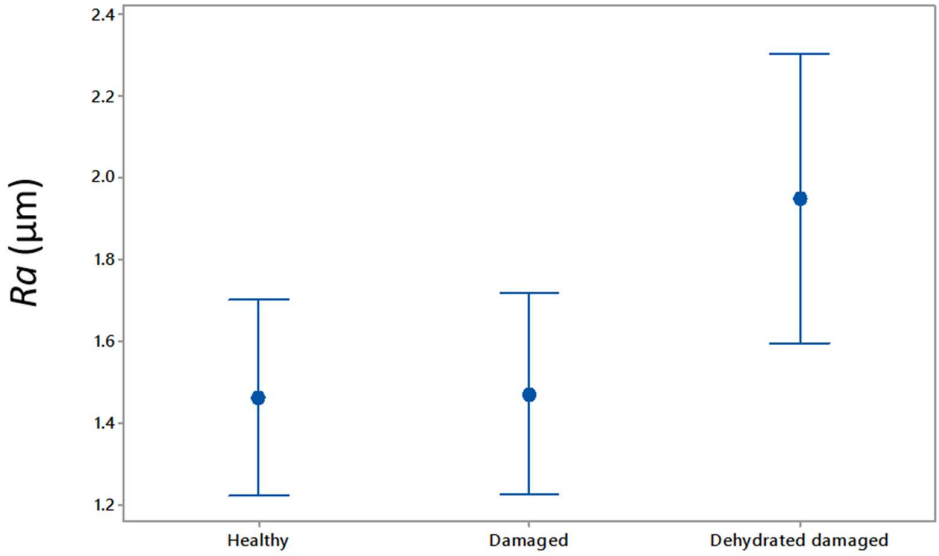


*Figure 5. 22 – Circumferential surface roughness ($Ra_C$) of healthy, damaged, and dehydrated damaged specimens. Error bars represent 95% confidence intervals where n = 12.*

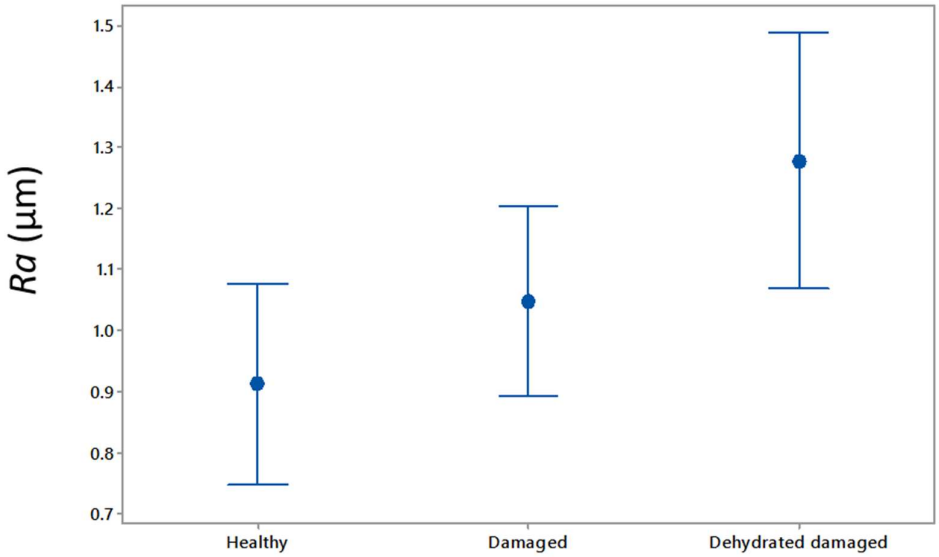


*Figure 5. 23 – Longitudinal surface roughness ($Ra_L$)of healthy, damaged, and dehydrated damaged specimens. Error bars represent 95% confidence intervals where n = 12.*

## 5.4 DISCUSSION

The frequency-dependent viscoelastic properties have been characterised for the first time (Burton, Freij, and Espino, 2017). The storage modulus was frequency-dependent, whereas the loss modulus was frequency-independent. Storage modulus was found to be much greater than loss modulus. Viscoelastic properties did not vary along the length of the LAD artery. After longitudinal damage was inflicted on the coronary artery, no change in *Ra* was noted, however with processing of the damaged tissue both $Ra_C$ and $Ra_L$ were significantly increased.

Frequency-dependent viscoelastic properties of porcine coronary arteries have not previously been quantified. However, viscoelastic properties have been measured in studies of other arteries. The results from this study show that the storage modulus is significantly greater than the loss modulus (approximately 10×) which is consistent with previous results on human arteries, where storage moduli were approximately 5× larger than loss moduli. The former was approximately 1 MPa as compared to 0.2 MPa for the loss modulus of carotid arteries. Further, the storage modulus varied from 3-7 MPa as compared to 0.4-1.6 MPa for femoral arteries (Learoyd and Taylor, 1966). Similarly, for canine femoral artery the storage was greater than loss modulus (1.20 MPa compared to 0.14 MPa respectively) (Bergel, 1961). The experimental techniques used by both differ to that used in this study, and involved pressurising the arterial specimens and measuring the oscillatory stress-strain relationship at various frequencies. Further differences in viscoelastic properties, as compared to this present study, are expected as different types of arteries are analysed. The results of the femoral artery storage and loss moduli better match the coronary arteries

measured during our study. Moreover, studies by Fischer and Llaurado (1966) have shown the collagen content of coronary arteries are similar to that of femoral arteries (percentage composition of collagen in dry defatted tissue; 47.9 ± 2.6% compared to 44.5 ± 1.4%, respectively). It was noted, though, that coronary arteries had the highest collagen to elastin ratio (Fischer and Llaurado, 1966).

In this study a frequency-dependent trend for the storage modulus was noted but not for the loss modulus. *Ergo*, as the heart rate increases, the LAD arterial wall is less able to store energy which is used for elastic recoil. This implies a change in the collagen-gel interaction leading to the storage of deformation energy within the tissue matrix with loading frequency. These deformations can involve elastic and plastic gel deformation and shearing on collagen fibrils (Goh, Aspden, and Hukins, 2004; Goh et al., 2007). A previous study by Wang *et al.*, observed that above 10 Hz the elastic modulus of murine pulmonary arteries increased with frequency (Wang et al., 2013). In this study there was no increase in moduli with frequency. The comparison is caveated, though, because there is no expectancy for the dynamic mechanical behaviour of a murine pulmonary and porcine coronary arteries to be parallel to each other. Further, Wang *et al.* characterised the frequency-dependent elastic modulus, as opposed to the dynamic viscoelasticity characterised in this current study. However, it is worth noting that between 1 and 10 Hz there was a decrease in elastic modulus in the study by Wang *et al.* demonstrating some consistency with findings from this current study.

Computational models are useful to study coronary arteries. For example, they can be used to create patient specific models, allow multiscale analysis of cells within the blood

(Friedman, Krams, and Chandran, 2010), or to supplement experimental investigations (Henninger et al., 2010). Viscoelastic properties of arteries have been found to be altered in patients with vascular diseases (Taniguchi et al., 2015). Hence, finite element models could be created which incorporate these viscoelastic properties. Coupled with surface reconstructions of coronary artery endothelium as presented in chapter 4 (figures 4. 13 and 4. 14), more predictable computational fluid dynamic models could be developed, whereby variation of the mechanical properties and surface roughness would improve the study of fluid structure interaction of coronary artery disease.

Given the absence of disease, the fact that there was no correlation between surface roughness and viscoelasticity was not unexpected. However, there may be benefits in assessing a correlation between the two during disease and this study demonstrates that both can be quantitatively measured. The results of this study found a significant difference in $Ra_L$ of damaged LAD coronary artery when comparing unprocessed and processed tissue, which differs from the results of healthy tissue studied in previous work (chapter 3). The cumulative processing effect has been shown in previous chapters to increase surface roughness in the circumferential direction, however, this is not noted in the longitudinal direction. Therefore, this study showed that causing longitudinal damage to LAD coronary arteries resulted in an increase in surface roughness along the same axis of processed tissue, which demonstrates the potential of using surface roughness to assess damage and disease in coronary arteries.

The damage inflicted on the coronary artery may have caused damage to the internal constituents of the artery. Collagen fibre orientation is reactive to load, irrespective of

loading direction. (Karimi et al., 2017). For example, in coronary adventitia, it was shown that the longitudinal stiffness was a direct result of initial fibre alignment, with collagen fibres uniformly stretching in the loading direction (Chen, Slipchenko, et al., 2013). This would support the increase in surface roughness in the longitudinal direction, where collagen may have stretched and deformed under the uniaxial loading condition. The multi-layer composition of coronary arteries is like that found in other biological tissue (Carniel, Gramigna, Fontanella, Frigo, et al., 2014). A constitutive analysis of colonic tissue concluded that the distribution and orientation of fibres within the layers of tissue was responsible for the anisotropic properties associated with the function of biological tissue (Carniel, Gramigna, Fontanella, Stefanini, et al., 2014). Thus, although mechanical loading damage to coronary arteries may not significantly alter the endothelial surface, it could affect the internal constituents of the coronary artery causing a resultant change in surface roughness. Although not significant, a notable increase was seen in $Ra_L$ due to uniaxial longitudinal damage (figure 5. 23). However, processing of tissue caused a greater change in surface roughness of LAD artery.

Consistent with previous findings (chapter 3), a significant difference was seen between $Ra_C$ and $Ra_L$ ($p < 0.05$), with surface roughness in the circumferential direction found to be greater than in the longitudinal direction (table 5. 4). Results were similar of undamaged dehydrated specimens in chapter 3 ($Ra_C$ and $Ra_L$: 1.98 ± 0.26 and 1.07 ± 0.18 µm) to the results of undamaged dehydrated control specimens in this chapter ($Ra_C$ and $Ra_L$: 1.91 ± 0.33 and 1.07 ± 0.20 µm). This again proves the repeatability of the process described in chapter 3 as a method to quantitatively measure the surface roughness of biological tissue, and validates the control results within this chapter.

## 5.5 CONCLUSION

This chapter describes the process and results of DMA of LAD coronary arteries, tested at physiological displacement and frequency ranges. It also presents the effect of mechanical damage on surface roughness. The following conclusions were made:

- a frequency-dependent trend was observed for the storage modulus where, as the frequency was increased, the storage modulus decreased from (mean ± standard deviation) 22.16 ± 8.75 MPa at 0.5 Hz to 17.75 ± 7.40 MPa at 10Hz; whereas the mean loss modulus was significantly lower at 2.10 ± 0.33 MPa, independent of frequency;
- storage and loss moduli did not vary along the length of the LAD artery;
- no significant difference was seen between the moduli results when measured at different extension ranges of 1-1.5 and 1.5-2 mm;
- no relationship was found between the viscoelastic properties and surface roughness
- damaging specimens through mechanical overloading had no significant effect on hydrated surface roughness measurements (1.46 ± 0.38 to 1.47 ± 0.39 µm and 0.91 ± 0.26 to 1.05 ± 0.25 µm: healthy and damaged $Ra_C$ and $Ra_L$);
- dehydrated damaged specimens were significantly rougher than their hydrated counterparts (1.95 ± 0.56 to 1.47 ± 0.39 µm and 1.28 ± 0.33 to 1.05 ± 0.25 µm: dehydrated and hydrated $Ra_C$ and $Ra_L$);
- the effect of chemical processing had a greater effect on *Ra* than mechanical damage.

Critically, though, this study demonstrates the feasibility of quantifying viscoelastic properties, and the potential of using mechanical and surface roughness properties in analysing disease of coronary arteries.

# 6 OVERALL DISCUSSION AND CONCLUSIONS

## 6.1 DISCUSSION

This aim of this thesis was to characterise properties of coronary arteries that could be used to aid in the development of medical treatments for coronary artery disease. This aim was met by, for the first time, quantitatively measuring the viscoelastic and surface roughness properties of porcine left anterior descending (LAD) coronary arteries; as presented in this thesis. The objectives of this thesis were met as follows:

- The surface roughness of coronary arteries was quantitatively characterised. Further, surface roughness was investigated at increased magnification in a multi-scale study. A correction factor was presented for changes in surface roughness due to chemical processing of tissue.
- The dynamic viscoelastic properties of coronary arteries were measured at physiological relevant frequencies.
- The effect of damage inflicted on coronary artery specimens through chemical fixation and dehydration, and mechanical overloading, was assessed through the change in surface roughness.

Chapter 3 used optical microscopy to study the surface roughness of LAD coronary arteries. The surface roughness (*Ra*) was measured in the circumferential ($Ra_C$) and longitudinal ($Ra_L$) directions of the artery, with $Ra_C$ found to be significantly greater than $Ra_L$. No variation was seen in surface roughness along the length of the coronary artery. Ridges were seen running parallel to the length of the artery, which previous studies have noted

due to the endothelial cell orientation (Uchida et al., 2011). The ridges had a helical orientation, which could explain the helical blood flow noted by others (Chiastra et al., 2017; Morbiducci et al., 2009). Studies investigating articular cartilage (Peng and Wang, 2013; Ghosh et al., 2013) noted multiscale variance in surface characterisation. Thus, LAD coronary artery was prepared to measure surface roughness through multiscale imaging at higher magnifications. Specimens were processed through chemical fixation and dehydration, a traditional procedure when performing scanning electron microscopy (SEM) of biological tissue. The effect of processing on surface roughness was evaluated. A significant increase was seen in $Ra_C$ due to processing and a correction factor was presented to calculate the surface roughness before processing from the dehydrated results, providing the outer limits of *Ra* values.

The multiscale investigation was performed in chapter 4. Higher magnifications were analysed (from 10× to an equivalent 5500×), with the use of optical microscopy, SEM, and atomic force microscopy. A trend was seen due to the scale of magnification where the magnification increased and $Ra_C$ decreased. This was similar to measurements of friction of human hair, with an increased friction found at a macro-scale compared to a micro- and nano-scale (LaTorre and Bhushan, 2006). The results presented in this chapter noted that surface roughness was more sensitive to the magnification rather than microscopy type.

The dynamic viscoelastic properties of coronary arteries were evaluated under physiological frequencies in chapter 5. The storage modulus was frequency dependent, decreasing while the frequency increased, whereas the loss modulus was frequency independent. The viscoelastic properties did not vary along the length of the coronary

arteries. Arteries were found to be stiffer in patients with vascular disease (Taniguchi et al., 2015), thus evaluating dynamic mechanical analysis of unhealthy coronary arteries would provide a better understanding of blood flow in diseased arteries.

Chapter 5 also analysed *Ra* after uniaxial mechanical damage was caused to specimens to replicate disease in the artery. Despite other studies noting a change in surface roughness of diseased biological tissue (Nabel and Braunwald, 2012; Bertazzo et al., 2013), no significant difference was noted in surface roughness of mechanically damaged specimens. However, after damaged specimens were processed through fixation and dehydration, a significant increase was seen both longitudinally and circumferentially. This differed from the results of healthy coronary arteries imaged in chapter 3, where only a difference was noted in $Ra_C$ due to processing. Mechanical damage did not affect the endothelial layer of the arteries as no difference was seen in the hydrated *Ra* measurements. However, it was hypothesised that the damage was caused to the constituents of the coronary artery, which agrees with studies by others whereby the collagen fibres are reactive to the loading of arteries (Karimi et al., 2017), with collagen fibres uniformly stretching in the loading direction (Chen, Slipchenko, et al., 2013). This is likely, as a significant increase was seen in $Ra_L$ after processing, along the loading direction of the uniaxial testing.

The surface roughness measurements of LAD coronary artery found in this study can help to inform the development of biomaterials. With the potential to nano-texture materials (Nazneen et al., 2012), it is possible to create biomaterials with multiscale roughness characteristics, similar to the micro- and nano-porosities created in other studies

(Perez and Mestres, 2016). The results can also be used as a standard for new biomaterials to be compared to, allowing biomaterials to be matched characteristically to mimic the biological tissue it is replacing. This could be through a comparison of mechanical properties, assessing the surface roughness of a new material, or even comparing the coverage of cell growth over an engineered surface. Further, the methods presented in this thesis can be replicated to characterise other biological materials, and to create correction factors for other chemical processing methods.

## 6.2 FURTHER WORK

The work presented in this thesis discusses that changes have been noted in the surface roughness of various biological tissues due to disease. In chapter 5, mechanical overloading of specimens caused an increase in surface roughness. Therefore, a valid assumption is that disease of coronary arteries, which can cause damage to the surface of the endothelium through the formation of atherosclerotic lesions, for example, would also result in changes to surface roughness. It is of value to investigate and quantify: firstly, the changes in surface roughness of diseased coronary artery compared to healthy; and secondly, the multi-scale properties of diseased coronary arteries.

By replicating the multi-scale surface roughness characteristics of coronary arteries through methods such as soft lithography, experimental physical models could simulate blood flow through the healthy and diseased arteries, including stenosed, atherosclerotic and calcified arteries. This would allow investigation of the relatively unknown helical flow phenomenon, and provide a method to validate computational fluid dynamic predictive models. Further, the mechanical and surface roughness properties characterised in this

thesis could be applied to a fluid structure interaction model. This model could be used to better predict disease of arteries or performance of medical interventions, for example to assess damage to the endothelial surface due to stent insertion or study elastic recoil complications associated with angioplasty. It would also influence the design and manufacture of biomaterials. Bulk materials designed with similar properties to those found in this study could be nano-textured to replicate the natural surface of coronary arteries to reduce the chance of neointimal hyperplasia or thrombosis.

## 6.3 CONCLUSIONS

For the first time, the dynamic viscoelasticity and surface roughness of LAD coronary arteries have been quantitatively characterised. It is important to consider the physiological loading conditions of biomaterials that are designed to replicate coronary arteries, as storage modulus was noted as frequency-dependent. Damage can be caused by uniaxial mechanical overloading that can be noticed as a change in surface roughness along the axis of loading. However chemical processing, specifically dehydration, results in a significant increase in surface roughness in the circumferential direction. A correction factor was offered for change in surface roughness due to processing coronary artery for SEM, although the methods presented can be replicated for further processing protocols pertinent to other microscopy techniques. When measuring surface roughness of biological tissue, microscopy technique should be kept consistent to allow comparable results. Critically, this study has demonstrated the feasibility of quantitatively measuring physical properties of coronary arteries which may have potential future applications to device design, disease assessment and their computational modelling.

# APPENDIX

The code presented below was compiled by Dr David G. Eckold (Eckold, 2016). Alicona software outputs a plain text format, with the 3D point cloud presented as a 3 × *n* array. This code interpolates the point cloud to fill in voids of missing data, and creates a reconstructed surface of the scan data.

```
function [ output, struct] = genAliconaImport(filename, varargin)

  % Import alicona data to matlab from a text file. It takes the form of
  % [primary, struct] = genAliconaImport('path/to/file.txt', 'option1',
  % value1, ..., 'optionN', valueN);

  %  This program will assume a single line header and footer on text files
  %  unless otherwise specified with the options:
  %  'startRow' & 'endRow'.

  %  To find the volume between the surface and the z plane, set
  %  'findVolume' to true.

  %  To plot the data, set 'plot' to one of the following:
  %  'contour', 'contourf', 'contour3', 'mesh', or 'surf'.

  %  To crop data, use 'crop' followed by [xmin,xmax,ymin,ymax]. N.B. these
  %  must be scaled to the new size!

  % Author Dr David G. Eckold

  % input argument parser
  defaultStartRow = 2;
  defaultEndRow = (numel(textread(filename,'%1c%*[^\n]')))-1;
  defaultScale = 1;
  defaultInterp = 'natural';
  defaultFindVol = false;
  defaultPlot = false;
  defaultContourLayers = 20;
  defaultCrop = false;
  expectedInterp = {'nearest','linear','natural'};
  expectedPlot = { 'contour', 'contourf', 'contour3', 'mesh', 'surf'};
  err = 'Value must be a positive number.';
  validationFunc = @(x) assert(isnumeric(x) && isscalar(x) && (x > 0), err);

  p = inputParser;
```

```
addRequired(p,'filename',@ischar);
addParamValue(p,'startRow',defaultStartRow,validationFunc);
addParamValue(p,'endRow',defaultEndRow,validationFunc);
addParamValue(p,'scale',defaultScale,validationFunc);
addParamValue(p,'interpolant',defaultInterp,@(x) any(validatestring(x,expectedInterp)));
addParamValue(p,'findVolume',defaultFindVol,@islogical);
addParamValue(p,'plot',defaultPlot,@(x) any(validatestring(x,expectedPlot)));
addParamValue(p,'contourLayers', defaultContourLayers, validationFunc);
addParamValue(p,'crop', defaultCrop)

parse(p,filename,varargin{:});

% Import data from Alicona file to tuplets.
startRow = p.Results.startRow;
endRow = p.Results.endRow;

formatSpec = '%13f%13f%f%[^\n\r]';

% Open the text file.
fileID = fopen(filename,'r');

dataArray = textscan(fileID, formatSpec, endRow(1)-startRow(1)+1, 'Delimiter', '', 'WhiteSpace', '',
'HeaderLines', startRow(1)-1, 'ReturnOnError', false);

% Close the text file.
fclose(fileID);

% Create output variable
xyz = [dataArray{1:end-1}];

% Convert Alicona tuplets to nxmx3 Mesh.
scale = p.Results.scale;

x = xyz(:,1); y = xyz(:,2); z = xyz(:,3);
x = x*scale; y = y*scale; z = z*scale;
dx = abs(x(find(diff(x),1)+1)-x(1));
dy = abs(y(find(diff(y),1)+1)-y(1));

if p.Results.crop == 0
        xvg = min(x):dx:max(x);
        yvg = min(y):dy:max(y);
elseif length(p.Results.crop) == 4;
        xvg = p.Results.crop(1):dx:p.Results.crop(2);
        yvg = p.Results.crop(3):dy:p.Results.crop(4);
else
        error('Incorrect number of inputs')
end
```

```
    F = scatteredInterpolant(x,y,z,p.Results.interpolant,'none');
    [vx,vy] = ndgrid(xvg,yvg);
    vz = F(vx,vy);

    % Write outputs and plot graphs if called for

    if p.Results.findVolume == 1
            output = dx*dy*sum(vz(:));
            struct.xyz(:,:,1) = vx;
            struct.xyz(:,:,2) = vy;
            struct.xyz(:,:,3) = vz;
    else
            output(:,:,1) = vx;
            output(:,:,2) = vy;
            output(:,:,3) = vz;
    end

    struct.d = [dx dy];
    struct.F = F;

    if p.Results.plot ~= 0
            figure
            if any(strcmp(p.Results.plot,{'contour','contourf','contour3'})) == 1;
                    feval(p.Results.plot, vx,vy,vz, p.Results.contourLayers)
                    c = colorbar;
                    ylabel(c, 'z, m')
            else
                    feval(p.Results.plot, vx,vy,vz);
                    zlabel('z, m')
            end
            ylabel('y, m')
            xlabel('x, m')
    end
end
```

# REFERENCES


Ahmed, M. 2015. 'The widow maker heart attack'. https://myheart.net/articles/the-widowmaker/.

Aidulis, D., Pegg, D.E., Hunt, C.J., Goffin, Y.A., Vanderkelen, A., Van Hoeck, B., Santiago, T., Ramos, T., Gruys, E., and Voorhout, W. 2002. 'Processing of ovine cardiac valve allografts: 1. Effects of preservation method on structure and mechanical properties', *Cell and Tissue Banking*, 3: 79-89.

Alhede, M., Qvortrup, K., Liebrechts, R., Høiby, N., Givskov, M., and Bjarnsholt, T. 2012. 'Combination of microscopic techniques reveals a comprehensive visual impression of biofilm structure and composition', *FEMS Immunology & Medical Microbiology*, 65: 335-42.

Alicona. 2014. 'Infinite focus technical specification', Accessed September 2014. http://www.alicona.com/home/fileadmin/alicona/pdfs/InfiniteFocusG5_System_and_technical_specification_E.pdf.

Alla, R.K., Ginjupalli, K., Upadhya, N., Shammas, M., Ravi, R.K., and Sekhar, R. 2011. 'Surface roughness of implants: a review', *Trends in Biomaterials and Artificial Organs*, 25: 112-18.

Angiero, F., Parma, L., Crippa, R., and Benedicenti, S. 2012. 'Diode laser (808 nm) applied to oral soft tissue lesions: a retrospective study to assess histopathological diagnosis and evaluate physical damage', *Lasers in Medical Science*, 27: 383-88.

Antonio, P.D., Lasalvia, M., Perna, G., and Capozzi, V. 2012. 'Scale-independent roughness value of cell membranes studied by means of AFM technique', *Biochimica et Biophysica Acta (BBA) - Biomembranes*, 1818: 3141-48.

Arbab-Zadeh, A., DeMaria, A.N., Penny, W.F., Russo, R.J., Kimura, B.J., and Bhargava, V. 1999. 'Axial movement of the intravascular ultrasound probe during the cardiac cycle: implications for three-dimensional reconstruction and measurements of coronary dimensions', *American heart journal*, 138: 865-72.

Ayyappan, J.P., Paul, A., and Goo, Y-H. 2016. 'Lipid droplet-associated proteins in atherosclerosis (review)', *Molecular Medicine Reports*, 13: 4527-34.

Azevedo, E.P., Retarekar, R., Raghavan, M.L., and Kumar, V. 2013. 'Mechanical properties of cellulose: chitosan blends for potential use as a coronary artery bypass graft', *Journal of Biomaterials Science, Polymer Edition*, 24: 239-52.

Barnes, S.C., Lawless, B.M., Shepherd, D.E.T., Espino, D.M., Bicknell, G.R., and Bryan, R.T. 2016. 'Viscoelastic properties of human bladder tumours', *Journal of the Mechanical Behavior of Biomedical Materials*, 61: 250-57.

Barnes, S.C., Shepherd, D.E.T., Espino, D.M., and Bryan, R.T. 2015. 'Frequency dependent viscoelastic properties of porcine bladder', *Journal of the Mechanical Behavior of Biomedical Materials*, 42: 168-76.

Beck, S.F. 1998. *Electrón microscopy: a handbook of techniques for the biologist* (Nassau Community College).

Bentzon, J.F., Otsuka, F., Virmani, R., and Falk, E. 2014. 'Mechanisms of plaque formation and rupture', *Circulation research*, 114: 1852-66.

Bergel, D.H. 1961. 'The dynamic elastic properties of the arterial wall', *The Journal of physiology*, 156: 458-69.

Berglund, J.D., Nerem, R.M., and Sambanis, A. 2005. 'Viscoelastic testing methodologies for tissue engineered blood vessels', *Journal of biomechanical engineering*, 127: 1176-84.

Bertazzo, S., Gentleman, E., Cloyd, K.L., Chester, A.H., Yacoub, M.H., and Stevens, M.M. 2013. 'Nano-analytical electron microscopy reveals fundamental insights into human cardiovascular tissue calcification', *Nature Materials*, 12: 576-83.

Betts, J.G., College, OpenStax, Desaix, P., Johnson, J.E., Johnson, E.W., Korol, O., Kruse, D., Poe, B., Wise, J., and Womble, M.D. 2013. *Anatomy and physiology* (OpenStax College).

BiologyGuide. 2012. 'Human biology', Accessed June 2017. http://www.biologyguide.net/human/heart.htm.

Bland, M. 2000. *An introduction to medical statistics* (Oxford University Press).

Bock, R.D. 1975. *Multivariate statistical methods in behavioral research* (Scientific Software International).

Boland, E.L., Grogan, J.A., and McHugh, P.E. 2017. 'Computational modeling of the mechanical performance of a magnesium stent undergoing uniform and pitting Corrosion in a remodeling artery', *Journal of Medical Devices, Transactions of the ASME*, 11.

British Heart Foundation. 2017. 'Cardiovascular disease statistcs compedum 2017'.

Bruinink, A., Bitar, M., Pleskova, M., Wick, P., Krug, H.F., and Maniura-Weber, K. 2014. 'Addition of nanoscaled bioinspired surface features: a revolution for bone related implants and scaffolds?', *Journal of Biomedical Materials Research Part A*, 102: 275-94.

Bucher, D., Scholz, M., Stetter, M., Obermayer, K., and Pflüger, H-J. 2000. 'Correction methods for three-dimensional reconstructions from confocal images: I. Tissue shrinking and axial scaling', *Journal of neuroscience methods*, 100: 135-43.

Burton, H.E., Freij, J.M., and Espino, D.M. 2017. 'Dynamic viscoelasticity and surface properties of porcine left anterior descending coronary arteries', *Cardiovascular Engineering & Technology*, 8: 41-56.

Burton, H.E., Williams, R.L., and Espino, D.M. 2017. 'Effects of freezing, fixation and dehydration on surface roughness properties of porcine left anterior descending coronary arteries', *Micron*, 101: 78-86.

Buys, A.V., Van Rooy, M-J., Soma, P., Van Papendorp, D., Lipinski, B., and Pretorius, E. 2013. 'Changes in red blood cell membrane structure in type 2 diabetes: a scanning electron and atomic force microscopy study', *Cardiovascular diabetology*, 12: 25.

Canale, C., Torre, B., Ricci, D., and Braga, P.C. 2011. 'Recognizing and avoiding artifacts in atomic force microscopy imaging', *Atomic Force Microscopy in Biomedical Research: Methods and Protocols*: 31-43.

Carniel, E.L., Gramigna, V., Fontanella, C.G., Frigo, A., Stefanini, C., Rubini, A., and Natali, A.N. 2014. 'Characterization of the anisotropic mechanical behaviour of colonic tissues: experimental activity and constitutive formulation', *Experimental Physiology*, 99: 759-71.

Carniel, E.L., Gramigna, V., Fontanella, C.G., Stefanini, C., and Natali, A.N. 2014. 'Constitutive formulations for the mechanical investigation of colonic tissues', *Journal of Biomedical Materials Research Part A*, 102: 1243-54.

Centre for Economic and Business Research. 2014. 'The economic cost of cardiovascular disease from 2014-2020 in six European economies'.

Chen, H., Cornwell, J., Zhang, H., Lim, T., Resurreccion, R., Port, T., Rosengarten, G., and Nordon, R.E. 2013. 'Cardiac-like flow generator for long-term imaging of endothelial cell responses to circulatory pulsatile flow at microscale', *Lab on a Chip*, 13: 2999-3007.

Chen, H., Slipchenko, M.N., Liu, Y., Zhao, X., Cheng, J-X., Lanir, Y., and Kassab, G.S. 2013. 'Biaxial deformation of collagen and elastin fibers in coronary adventitia', *Journal of Applied Physiology*, 115: 1683-93.

Chen, H., Zhao, X., Berwick, Z.C., Krieger, J.F., Chambers, S., and Kassab, G.S. 2016. 'Microstructure and mechanical property of glutaraldehyde-treated porcine pulmonary ligament', *Journal of biomechanical engineering*, 138: 061003.

Chen, L., Han, D., and Jiang, L. 2011. 'On improving blood compatibility: from bioinspired to synthetic design and fabrication of biointerfacial topography at micro/nano scales', *Colloids and Surfaces B: Biointerfaces*, 85: 2-7.

Cheng, T.O. 2012. 'History of coronary artery bypass surgery - half of a century of progress', *International Journal of Cardiology*, 157: 1-2.
Chiastra, C., Gallo, D., Tasso, P., Iannaccone, F., Migliavacca, F., Wentzel, J.J., and Morbiducci, U. 2017. 'Healthy and diseased coronary bifurcation geometries influence near-wall and intravascular flow: a computational exploration of the hemodynamic risk', *Journal of Biomechanics*.
Chow, M.J., and Zhang, Y. 2011. 'Changes in the mechanical and biochemical properties of aortic tissue due to cold storage', *Journal of Surgical Research*, 171: 434-42.
Claes, E., Atienza, J.M., Guinea, G.V., Rojo, F.J., Bernal, J.M., Revuelta, J.M., and Elices, M. 2010. "Mechanical properties of human coronary arteries." In *Engineering in Medicine and Biology Society (EMBC), 2010 Annual International Conference of the IEEE*, 3792-95. IEEE.
Clark, R.E. 1973. 'Stress strain characteristics of fresh and frozen human aortic and mitral leaflets and chordae tendineae: implications for clinical use', *Journal of Thoracic and Cardiovascular Surgery*, 66: 202-08.
Coolong, A., and Mauri, L. 2006. 'Clopidogrel treatment surrounding percutaneous coronary intervention: when should it be started and stopped?', *Current cardiology reports*, 8: 267-71.
Craiem, D., and Armentano, R.L. 2006. 'A fractional derivative model to describe arterial viscoelasticity', *Biorheology*, 44: 251-63.
Dahl, S.L.M., Koh, J., Prabhakar, V., and Niklason, L.E. 2003. 'Decellularized native and engineered arterial scaffolds for transplantation', *Cell transplantation*, 12: 659-66.
Damink, L.H.H.O., Dijkstra, P.J., Van Luyn, M.J.A., Van Wachem, P.B., Nieuwenhuis, P., and Feijen, J. 1995. 'Glutaraldehyde as a crosslinking agent for collagen-based biomaterials', *Journal of Materials Science: Materials in Medicine*, 6: 460-72.
Das Murtey, M., and Ramasamy, P. 2016. *Sample preparations for scanning electron microscopy – life sciences* (InTech).
DePalma, V.A., Baier, R.E., Ford, J.W., Gott, V.L., and Furuse, A. 1972. 'Investigation of three-surface properties of several metals and their relation to blood compatibility', *Journal of Biomedical Materials Research Part A*, 6: 37-75.
Desai, M., Seifalian, A.M., and Hamilton, G. 2011. 'Role of prosthetic conduits in coronary artery bypass grafting', *European Journal of Cardio-Thoracic Surgery*, 40: 394-98.
Doughty, M.J. 1995. 'Correcting cell density measurements for tissue hydration changes in scanning electron microscopy - application to the rabbit corneal endothelium', *Tissue and Cell*, 27: 207-20.
Eckold, D.G. 2016. 'Spinal implants - the problems of debris', University of Birmingham.
Eckold, D.G., Dearn, K.D., and Shepherd, D.E.T. 2015. 'The evolution of polymer wear debris from total disc arthroplasty', *Biotribology*, 1: 42-50.
EDinformatics. 1999. 'What are the components of blood?', Accessed June 2017. http://www.edinformatics.com/math_science/what-is-blood-made-of.html.
Endo, M. 2000. 'The history and evolution of coronary artery bypass grafting', *Nippon Geka Gakkai zasshi*, 101: 827-32.
Eskin, S.G., Ives, C.L., McIntire, L.V., and Navarro, L.T. 1984. 'Response of cultured endothelial cells to steady flow', *Microvascular Research*, 28: 87-94.
Espino, D.M., Hukins, D.W.L., Shepherd, D.E.T., Watson, M.A., and Buchan, K.G. 2006. 'Determination of the pressure required to cause mitral valve failure', *Medical Engineering & Physics*, 28: 36-41.
Espino, D.M., Shepherd, D.E.T., and Buchan, K.G. 2007. 'Effect of mitral valve geometry on valve competence', *Heart and Vessels*, 22: 109-15.
Espino, D.M., Shepherd, D.E.T., Hukins, D.W.L., and Buchan, K.G. 2005. 'The role of chordae tendineae in mitral valve competence', *The Journal of heart valve disease*, 14: 603-09.

Fan, H., Chen, P., Qi, R., Zhai, J., Wang, J., Chen, L., Chen, L., Sun, Q., Song, Y., and Han, D. 2009. 'Greatly improved blood compatibility by microscopic multiscale design of surface architectures', *Small*, 5: 2144-48.

Fioretta, E.S., Fledderus, J.O., Burakowska-Meise, E.A., Baaijens, F., Verhaar, M.C., and Bouten, C.V.C. 2012. 'Polymer-based scaffold designs for in situ vascular tissue engineering: controlling recruitment and differentiation behavior of endothelial colony forming cells', *Macromolecular bioscience*, 12: 577-90.

Fischer, G.M., and Llaurado, J.G. 1966. 'Collagen and elastin content in canine arteries selected from functionally different vascular beds', *Circulation research*, 19: 394-99.

Fitzgibbon, G.M., Burton, J.R., and Leach, A.J. 1978. 'Coronary bypass graft fate: angiographic grading of 1400 consecutive grafts early after operation and of 1132 after one year', *Circulation*, 57: 1070-74.

Flemming, R.G., Murphy, C.J., Abrams, G.A., Goodman, S.L., and Nealey, P.F. 1999. 'Effects of synthetic micro-and nano-structured surfaces on cell behavior', *Biomaterials*, 20: 573-88.

Forster, H., and Fisher, J. 1999. 'The influence of continuous sliding and subsequent surface wear on the friction of articular cartilage', *Proceedings of the Institution of Mechanical Engineers, Part H: Journal of Engineering in Medicine*, 213: 329-45.

Fowkes, G., and Gillespie, I.N. 1998. 'Angioplasty (versus non surgical management) for intermittent claudication', *The Cochrane Library*.

Friedman, M.H., Krams, R., and Chandran, K.B. 2010. 'Flow interactions with cells and tissues: cardiovascular flows and fluid–structure interactions', *Annals of Biomedical Engineering*, 38: 1178-87.

Fulcher, G.R., Hukins, D.W.L., and Shepherd, D.E.T. 2009. 'Viscoelastic properties of bovine articular cartilage attached to subchondral bone at high frequencies', *BMC Musculoskeletal Disorders*, 10: 61.

Fung, Y.C. 1993. *Biomechanics: mechanical properties of living tissues* (Springer: New York).

Fung, Y.C., and Sobin, S.S. 1981. 'The retained elasticity of elastin under fixation agents', *Journal of biomechanical engineering*, 103: 121-22.

Gadd, M.J., and Shepherd, D.E.T. 2011. 'Viscoelastic properties of the intervertebral disc and the effect of nucleus pulposus removal', *Proceedings of the Institution of Mechanical Engineers, Part H: Journal of Engineering in Medicine*, 225: 335-41.

García, A., Martínez, M. A., and Peña, E. 2012. 'Viscoelastic properties of the passive mechanical behavior of the porcine carotid artery: Influence of proximal and distal positions', *Biorheology*, 49: 271-88.

Ghosh, S., Bowen, J., Jiang, K., Espino, D.M., and Shepherd, D.E.T. 2013. 'Investigation of techniques for the measurement of articular cartilage surface roughness', *Micron*, 44: 179-84.

Girasole, M., Pompeo, G., Cricenti, A., Congiu-Castellano, A., Andreola, F., Serafino, A., Frazer, B.H., Boumis, G., and Amiconi, G. 2007. 'Roughness of the plasma membrane as an independent morphological parameter to study RBCs: a quantitative atomic force microscopy investigation', *Biochimica et Biophysica Acta (BBA)-Biomembranes*, 1768: 1268-76.

Gittens, R.A., McLachlan, T., Cai, Y., Berner, S., Tannenbaum, R., Schwartz, Z., Sandhage, K.H., and Boyan, B.D. 2011. 'The effects of combined micron-/submicron-scale surface roughness and nanoscale features on cell proliferation and differentiation', *Biomaterials*, 32: 3395-403.

Glagov, S. 1979. 'Relation of structure to function in arterial walls', *Artery*, 5: 295.

Goh, K.L., Chen, Y., Chou, S.M., Listrat, A., Bechet, D., and Wess, T.J. 2010. 'Effects of frozen storage temperature on the elasticity of tendons from a small murine model', *Animal*, 4: 1613-17.

Goh, K.L., Meakin, J.R., Aspden, R.M., and Hukins, D.W.L. 2007. 'Stress transfer in collagen fibrils reinforcing connective tissues: effects of collagen fibril slenderness and relative stiffness', *Journal of theoretical biology*, 245: 305-11.

Govindarajan, T., and Shandas, R. 2014. 'A survey of surface modification techniques for next-generation shape memory polymer stent devices', *Polymers*, 6: 2309-31.
Gow, B.S., and Taylor, M.G. 1968. 'Measurement of viscoelastic properties of arteries in the living dog', *Circulation research*, 23: 111-22.
Grassl, E.D., Barocas, V.H., and Bischof, J.C. 2004. "Effects of freezing on the mechanical properties of blood vessels." In *ASME 2004 International Mechanical Engineering Congress and Exposition*, 699-703. American Society of Mechanical Engineers.
Grishina, O.A., Kirillova, I.V., and Glukhova, O.E. 2016. 'Biomechanical rationale of coronary artery bypass grafting of multivessel disease', *Computer methods in biomechanics and biomedical engineering*, 19: 297-305.
Hall, J.E. 2010. *Guyton and Hall textbook of medical physiology* (Elsevier Health Sciences).
Hamid, H., and Coltart, J. 2007. ''‘Miracle stents’-a future without restenosis', *McGill Journal of Medicine: MJM*, 10: 105.
Hansson, G.K., Libby, P., and Tabas, I. 2015. 'Inflammation and plaque vulnerability', *Journal of internal medicine*, 278: 483-93.
Hayat, M.A. 1981. *Principles and techniques of electron microscopy* (Edward Arnold: London, United Kingdom).
Hayat, M.A. 2012. *Fixation for electron microscopy* (Elsevier Science).
He, W., Ma, Z., Yong, T., Teo, W.E., and Ramakrishna, S. 2005. 'Fabrication of collagen-coated biodegradable polymer nanofiber mesh and its potential for endothelial cells growth', *Biomaterials*, 26: 7606-15.
Head, S.J., Kieser, T.M., Falk, V., Huysmans, H.A., and Kappetein, A.P. 2013. 'Coronary artery bypass grafting: part 1 - the evolution over the first 50 years', *European heart journal*, 34: 2862-72.
HealthUnlocked. 2015. 'Coronary angioplasty and stent insertion - risks', Accessed September 2017. http://www.nhs.uk/Conditions/Coronary-angioplasty/Pages/risks.aspx.
Henninger, H.B., Reese, S.P., Anderson, A.E., and Weiss, J.A. 2010. 'Validation of computational models in biomechanics', *Proceedings of the Institution of Mechanical Engineers, Part H: Journal of Engineering in Medicine*, 224: 801-12.
Hickey, D.S., and Hukins, D.W.L. 1979. 'Effect of methods of preservation on the arrangement of collagen fibrils in connective tissue matrices: an X-ray diffraction study of annulus fibrosus', *Connective Tissue Research*, 6: 223-28.
Hiersemenzel, F., Petzing, J.N., Leach, R.K., Helmli, F., and Singh, J. 2012. "Areal texture and angle measurements of tilted surfaces using focus variation methods." In *3rd International Conference on Surface Metrology*. France.
Hitachi High-Technologies Corporation. 2013. 'Hitachi tabletop microscope TM3030'
Hołda, M.K., Klimek-Piotrowska, W., Koziej, M., Piątek, K., and Hołda, J. 2016. 'Influence of different fixation protocols on the preservation and dimensions of cardiac tissue', *Journal of anatomy*.
Holman, B.F., Cuplov, V., Millner, L., Hutton, B.F., Maher, T.M., Groves, A.M., and Thielemans, K. 2015. 'Improved correction for the tissue fraction effect in lung PET/CT imaging', *Physics in Medicine Biology*, 60: 7387-402.
Holzapfel, G.A., Gasser, T.C., and Stadler, M. 2002. 'A structural model for the viscoelastic behavior of arterial walls: continuum formulation and finite element analysis', *European Journal of Mechanics A - Solids*, 21: 441-63.
Holzapfel, G.A., Sommer, G., Gasser, C.T., and Regitnig, P. 2005. 'Determination of layer-specific mechanical properties of human coronary arteries with nonatherosclerotic intimal thickening and related constitutive modeling', *American Journal of Physiology - Heart and Circulatory Physiology*, 289: H2048-H58.

Howlett, J.G. 2016. 'Overview of coronary artery disease (CAD)', Accessed August 2017. http://www.msdmanuals.com/home/heart-and-blood-vessel-disorders/coronary-artery-disease/overview-of-coronary-artery-disease-cad.

Huang, B.Q., and Yeung, E.C. 2015. 'Chemical and physical fixation of cells and tissues: an overview.' in, *Plant Microtechniques and Protocols*.

Hukins, D.W.L., Leahy, J.C., and Mathias, K.J. 1999. 'Biomaterials: defining the mechanical properties of natural tissues and selection of replacement materials', *Journal of Materials Chemistry*, 9: 629-36.

ISO 4288. 1996. 'Geometrical product specifications (GPS) -surface texture: profile method - rules and procedures for the assessment of surface texture'

ISO 4287. 2009. 'Geometrical product specifications (GPS)-surface texture: profile method–terms, definitions and surface texture parameters (ISO 4287: 1997+ Cor 1: 1998+ Cor 2: 2005+ Amd 1: 2009)(includes Corrigendum AC: 2008 and Amendment A1: 2009)'

ISO 25178. 2012. 'Geometrical product specifications (GPS) - surface texture: Areal - part 2: terms, definitions and surface texture parameters'

Jung, H.J., Vangipuram, G., Fisher, M.B., Yang, G., Hsu, S., Bianchi, J., Ronholdt, C., and Woo, S.L.Y. 2011. 'The effects of multiple freeze-thaw cycles on the biomechanical properties of the human bone-patellar tendon-bone allograft', *Journal of Orthopaedic Research*, 29: 1193-98.

Kakisis, J.D., Liapis, C.D., Breuer, C., and Sumpio, B.E. 2005. 'Artificial blood vessel: the Holy Grail of peripheral vascular surgery', *Journal of vascular surgery*, 41: 349-54.

Karagkiozaki, V., Karagiannidis, P.G., Kalfagiannis, N., Kavatzikidou, P., Patsalas, P., Georgiou, D., and Logothetidis, S. 2012. 'Novel nanostructured biomaterials: implications for coronary stent thrombosis', *International journal of nanomedicine*, 7: 6063.

Karimi, A., Navidbakhsh, M., Shojaei, A., and Faghihi, S. 2013. 'Measurement of the uniaxial mechanical properties of healthy and atherosclerotic human coronary arteries', *Materials Science and Engineering: C*, 33: 2550-54.

Karimi, A., Rahmati, S.M., Sera, T., Kudo, S., and Navidbakhsh, M. 2017. 'A combination of constitutive damage model and artificial neural networks to characterize the mechanical properties of the healthy and atherosclerotic human coronary arteries', *Artificial Organs*.

Karimi, A., Sera, T., Kudo, S., and Navidbakhsh, M. 2016. 'Experimental verification of the healthy and atherosclerotic coronary arteries incompressibility via digital image correlation', *Artery Research*, 16: 1-7.

Karpuschewski, B., Schmidt, K., Beňo, J., Maňková, I., Frohmüller, R., and Prilukova, J. 2015. 'An approach to the microscopic study of wear mechanisms during hard turning with coated ceramics', *Wear*, 342-343: 222-33.

Kashi, A.M., Tahemanesh, K., Chaichian, S., Joghataei, M.T., Moradi, F., Tavangar, S.M., Najafabadi, A.S.M., Lotfibakhshaiesh, N., Beyranvand, S.P., and Anvari-Yazdi, A.F. 2014. 'How to prepare biological samples and live tissues for scanning electron microscopy (SEM)', *Galen Medical Journal*, 3: 63-80.

Kirsanov, R.I., and Kulikov, V.P. 2012. 'Helical (spiral or swirling) blood flow in cardiovascular system', *Uspekhi Fiziologicheskikh Nauk*, 44: 62-78.

Kiyan, Y., Kurselis, K., Kiyan, R., Haller, H., Chichkov, B.N., and Dumler, I. 2013. 'Urokinase receptor counteracts vascular smooth muscle cell functional changes induced by surface topography', *Theranostics*, 3: 516.

Konta, T., Hugh, J., and Bett, N. 2003. 'Patterns of coronary artery movement and the development of coronary atherosclerosis', *Circulation Journal*, 67: 846-50.

Krucoff, M.W., Kereiakes, D.J., Petersen, J.L., Mehran, R., Hasselblad, V., Lansky, A.J., Fitzgerald, P.J., Garg, J., Turco, M.A., and Simonton, C.A. 2008. 'A novel bioresorbable polymer paclitaxel-eluting stent for the treatment of single and multivessel coronary disease: primary results of

the COSTAR (cobalt chromium stent with antiproliferative for restenosis) II study', *Journal of the American College of Cardiology*, 51: 1543-52.
Kural, M.H., Cai, M., Tang, D., Gwyther, T., Zheng, J., and Billiar, K.L. 2012. 'Planar biaxial characterization of diseased human coronary and carotid arteries for computational modeling', *Journal of Biomechanics*, 45: 790-98.
Kurella, A., and Dahotre, N.B. 2005. 'Review paper: surface modification for bioimplants: the role of laser surface engineering', *Journal of biomaterials applications*, 20: 5-50.
Kuznetsova, T., Herbots, L., Richart, T., D'hooge, J., Thijs, L., Fagard, R.H., Herregods, M-C., and Staessen, J.A. 2008. 'Left ventricular strain and strain rate in a general population', *European heart journal*, 29: 2014-23.
Laki, K. 1972. 'Our ancient heritage in blood clotting and some of its consequences', *Annals of the New York Academy of Sciences*, 202: 297-307.
Lally, C., Reid, A.J., and Prendergast, P.J. 2004. 'Elastic behavior of porcine coronary artery tissue under uniaxial and equibiaxial tension', *Annals of Biomedical Engineering*, 32: 1355-64.
LaTorre, C., and Bhushan, B. 2006. 'Investigation of scale effects and directionality dependence on friction and adhesion of human hair using AFM and macroscale friction test apparatus', *Ultramicroscopy*, 106: 720-34.
Lawless, B.M., Barnes, S.C., Espino, D.M., and Shepherd, D.E.T. 2016. 'Viscoelastic properties of a spinal posterior dynamic stabilisation device', *Journal of the Mechanical Behavior of Biomedical Materials*, 59: 519-26.
Le, X., Poinern, G.E.J., Ali, N., Berry, C.M., and Fawcett, D. 2013. 'Engineering a biocompatible scaffold with either micrometre or nanometre scale surface topography for promoting protein adsorption and cellular response', *International journal of biomaterials*, 2013.
Learoyd, B.M., and Taylor, M.G. 1966. 'Alterations with age in the viscoelastic properties of human arterial walls', *Circulation research*, 18: 278-92.
Lee, J., and Smith, N.P. 2012. 'The multi-scale modelling of coronary blood flow', *Annals of Biomedical Engineering*, 40: 2399-413.
Leszczak, V., and Popat, K.C. 2014. 'Improved in vitro blood compatibility of polycaprolactone nanowire surfaces', *ACS applied materials & interfaces*, 6: 15913-24.
Li, L., Mirhosseini, N., Michael, A., Liu, Z., and Wang, T. 2013. 'Enhancement of endothelialisation of coronary stents by laser surface engineering', *Lasers in Surgery and Medicine*, 45: 608-16.
Linneweber, J., Dohmen, P.M., Kertzscher, U., Affeld, K., Nose, Y., and Konertz, W. 2007. 'The effect of surface roughness on activation of the coagulation system and platelet adhesion in rotary blood pumps', *Artificial Organs*, 31: 345-51.
Liu, X., Chu, P., and Ding, C. 2004. 'Surface modification of titanium, titanium alloys, and related materials for biomedical applications', *Materials Science and Engineering: R: Reports*, 47: 49-121.
Liu, X., Sun, A., Fan, Y., and Deng, X. 2014. 'Physiological significance of helical flow in the arterial system and its potential clinical applications', *Annals of Biomedical Engineering*, 43: 3-15.
Lorenzetti, M., Dogša, I., Stošicki, T., Stopar, D., Kalin, M., Kobe, S., and Novak, S. 2015. 'The influence of surface modification on bacterial adhesion to titanium-based substrates', *ACS applied materials & interfaces*, 7: 1644-51.
Lu, Z., Jiang, X., Zuo, X., and Feng, L. 2016. 'Improvement of cytocompatibility of 3D-printing resins for endothelial cell adhesion', *RSC Advances*, 6: 102381-88.
Mate, C.M., McClelland, G.M., Erlandsson, R., and Chiang, S. 1987. 'Atomic-scale friction of a tungsten tip on a graphite surface', *Physical review letters*, 59: 1942.
Maton, A., Hopkins, J., McLaughlin, C.W., Johnson, S., Warner, M.Q., LaHart, D., Wright, J.D., and Deep, V.K. 1997. *Human biology and health.* (Prentice Hall: Englewood Cliffs, New Jersey, US).

Mazur, W., Siegel, M.J., Miszalski-Jamka, T., and Pelberg, R. 2013. *CT atlas of adult congenital heart disease* (Springer London).
Menard, K.P. 2008. *Dynamic mechanical analysis: a practical introduction* (CRC press).
Migneault, I., Dartiguenave, C., Bertrand, M.J., and Waldron, K.C. 2004. 'Glutaraldehyde: behavior in aqueous solution, reaction with proteins, and application to enzyme crosslinking', *Biotechniques*, 37: 790-806.
Millard, L., Espino, D.M., Shepherd, D.E.T., Hukins, D.W.L., and Buchan, K.G. 2011. 'Mechanical properties of chordae tendineae of the mitral heart valve: Young's modulus, structural stiffness, and effects of aging', *Journal of Mechanics in Medicine and Biology*, 11: 221-30.
Mohr, F.W., Rastan, A.J., Serruys, P.W., Kappetein, A.P., Holmes, D.R., Pomar, J.L., Westaby, S., Leadley, K., Dawkins, K.D., and Mack, M.J. 2011. 'Complex coronary anatomy in coronary artery bypass graft surgery: impact of complex coronary anatomy in modern bypass surgery? Lessons learned from the SYNTAX trial after two years', *The Journal of Thoracic and Cardiovascular Surgery*, 141: 130-40.
Molina, J.E., Carr, M., and Yarnoz, M.D. 1978. 'Coronary bypass with Gore-Tex graft', *The Journal of Thoracic and Cardiovascular Surgery*, 75: 769-71.
Moran, P., and Coats, B. 2012. 'Biological sample preparation for SEM imaging of porcine retina', *Microscopy Today*, 20: 28-31.
Morbiducci, U., Ponzini, R., Rizzo, G., Cadioli, M., Esposito, A., De Cobelli, F., Del Maschio, A., Montevecchi, F.M., and Redaelli, A. 2009. 'In vivo quantification of helical blood flow in human aorta by time-resolved three-dimensional cine phase contrast magnetic resonance imaging', *Annals of Biomedical Engineering*, 37: 516-31.
Mozaffarian, D., Benjamin, E.J., Go, A.S., Arnett, D.K., Blaha, M.J., Cushman, M., de Ferranti, S., Després, J-P., Fullerton, H..J., Howard, V.J., Huffman, M.D., Judd, S.E., Kissela, B.M., Lackland, D.T., Lichtman, J.H., Lisabeth, L.D., Liu, S., Mackey, R.H., Matchar, D.B., McGuire, D.K., Mohler, E.R. 3rd, Moy, C.S., Muntner, P., Mussolino, M.E., Nasir, K., Neumar, R.W., Nichol, G., Palaniappan, L., Pandey, D.K., Reeves, M.J., Rodriguez, C.J., Sorlie, P.D., Stein, J., Towfighi, A., Turan, T.N., Virani, S.S., Willey, J.Z., Woo, D., Yeh, R.W., and Turner, M.B. 2015. 'Heart disease and stroke statistics - 2015 update: a report from the American Heart Association', *Circulation*, 131: 29-322.
Mueller, R.L., and Sanborn, T.A. 1995. 'The history of interventional cardiology: cardiac catheterization, angioplasty, and related interventions', *American heart journal*, 129: 146-72.
Mukherjee, S., Reddy, V.J., Ravichandran, R., Mathapati, S., Guhathakurta, S., Raghunath, M., and Ramakrishna, S. 2012. "Practical considerations for medical applications using biological grafts and their derivatives." In *MRS*, mrsf11-1418-mm10-18. Cambridge Univ Press.
Müller-Schweinitzer, E. 1994. 'Applications for cryopreserved blood vessels in pharmacological research', *Cryobiology*, 31: 57-62.
Müller-Schweinitzer, E., Mihatsch, M.J., Schilling, M., and Haefeli, W.E. 1997. 'Functional recovery of human mesenteric and coronary arteries after cryopreservation at -196° C in a serum-free medium', *Journal of vascular surgery*, 25: 743-50.
Müller, F.C. 2008. 'Tauchen nach Herzinfarkt', Accessed January 2017. https://www.tauchen.de/tauchwissen/tauchmedizin/tauchen-nach-herzinfarkt/.
Nabel, E.G., and Braunwald, E. 2012. 'A tale of coronary artery disease and myocardial infarction', *New England Journal of Medicine*, 366: 54-63.
National Heart, Lung and Blood Institute. 2016. 'What is coronary heart diease?'. https://www.nhlbi.nih.gov/health/health-topics/topics/cad#.
Nazneen, F., Galvin, P., Arrigan, D.W.M., Thompson, M., Benvenuto, P., and Herzog, G. 2012. 'Electropolishing of medical-grade stainless steel in preparation for surface nano-texturing', *Journal of Solid State Electrochemistry*, 16: 1389-97.

Newsome, L.T., Kutcher, M.A., and Royster, R.L. 2008. 'Coronary artery stents: part I. Evolution of percutaneous coronary intervention', *Anesthesia & Analgesia*, 107: 552-69.
Niu, L., Qian, M., Yang, W., Meng, L., Xiao, Y., Wong, K.K.L., Abbott, D., Liu, X., and Zheng, H. 2013. 'Surface roughness detection of arteries via texture analysis of ultrasound images for early diagnosis of atherosclerosis', *PloS one*, 8.
O'Brien, B., and Carroll, W. 2009. 'The evolution of cardiovascular stent materials and surfaces in response to clinical drivers: a review', *Acta biomaterialia*, 5: 945-58.
O'Brien, B., Zafar, H., Ibrahim, A., Zafar, J., and Sharif, F. 2016. 'Coronary stent materials and coatings: a technology and performance update', *Annals of Biomedical Engineering*, 44: 523-35.
O'Leary, S.A., Doyle, B.J., and McGloughlin, T.M. 2014. 'The impact of long term freezing on the mechanical properties of porcine aortic tissue', *Journal of the Mechanical Behavior of Biomedical Materials*, 37: 165-73.
Oliveira, R.R.L.De., Albuquerque, D.A.C., Cruz, T.G.S., Yamaji, F.M., and Leite, F.L. 2012. 'Measurement of the nanoscale roughness by atomic force microscopy: basic principles and applications.' in, *Atomic Force Microscopy-Imaging, Measuring and Manipulating Surfaces at the Atomic Scale* (InTech).
Ozolanta, I., Tetere, G., Purinya, B., and Kasyanov, V. 1998. 'Changes in the mechanical properties, biochemical contents and wall structure of the human coronary arteries with age and sex', *Medical Engineering & Physics*, 20: 523-33.
Parekh, M., Ruzza, A., Salvalaio, G., Ferrari, S., Camposampiero, D., Busin, M., and Ponzin, D. 2014. 'Descemet membrane endothelial keratoplasty tissue preparation from donor corneas using a standardized submerged hydro-separation method', *American Journal of Ophthalmology*, 158: 277-85.e1.
Park, S.W., Intaglietta, M., and Tartakovsky, D.M. 2012. 'Impact of endothelium roughness on blood flow', *Journal of theoretical biology*, 300: 152-60.
Pearson, B., and Espino, D.M. 2013. 'Effect of hydration on the frequency-dependent viscoelastic properties of articular cartilage', *Proceedings of the Institution of Mechanical Engineers, Part H: Journal of Engineering in Medicine*, 227: 1246-52.
Peng, Z., and Wang, M. 2013. 'Three dimensional surface characterization of human cartilages at a micron and nanometre scale', *Wear*, 301: 210-17.
Perez, R.A., and Mestres, G. 2016. 'Role of pore size and morphology in musculo-skeletal tissue regeneration', *Materials Science and Engineering: C*, 61: 922-39.
Pescador, D. 2014. 'Las grasas no son el problema, la comunidad médica reconoce el error', Accessed August 2017. http://transformer.blogs.quo.es/2014/11/04/las-grasas-no-son-el-problema-la-comunidad-medica-reconoce-el-error/.
Peters, A.E., Comerford, E.J., Macaulay, S., Bates, K.T., and Akhtar, R. 2017. 'Micromechanical properties of canine femoral articular cartilage following multiple freeze-thaw cycles', *Journal of the Mechanical Behavior of Biomedical Materials*, 71: 114-21.
Purslow, P.P., Wess, T.J., and Hukins, D.W.L. 1998. 'Collagen orientation and molecular spacing during creep and stress-relaxation in soft connective tissues', *Journal of Experimental Biology*, 201: 135-42.
Radjeman, A., and Lim, K.O. 1986. 'The effect of temperature and glutaraldehyde fixation on the mechanical properties of bovine pericardial tissues', *The Japanese journal of physiology*, 36: 1093-100.
Reichlin, T., Wild, A., Dürrenberger, M., Daniels, A.U., Aebi, U., Hunziker, P.R., and Stolz, M. 2005. 'Investigating native coronary artery endothelium in situ and in cell culture by scanning force microscopy', *Journal of structural biology*, 152: 52-63.
Reilly, J. 2015. "Applied statistics." In.: Statistical Solutions.

Ross, A.M., and Lahann, J. 2013. 'Surface engineering the cellular microenvironment via patterning and gradients', *Journal of Polymer Science Part B: Polymer Physics*, 51: 775-94.
Ross, R. 1999. 'Atherosclerosis - an inflammatory disease', *New England Journal of Medicine*, 340: 115-26.
Sadeghi, H., Espino, D.M., and Shepherd, D.E.T. 2015. 'Variation in viscoelastic properties of bovine articular cartilage below, up to and above healthy gait-relevant loading frequencies', *Proceedings of the Institution of Mechanical Engineers, Part H: Journal of Engineering in Medicine*, 229: 115-23.
Sandau, K., and Kurz, H. 1997. 'Measuring fractal dimension and complexity - An alternative approach with an application', *Journal of Microscopy*, 186: 164-76.
Schmidler, C. 2017. 'Angioplasty – coronary (heart) stent implants PTCA', Accessed August 2017. https://www.healthpages.org/surgical-care/angioplasty-coronary-heart-stents/.
Schmidt, M., Nazneen, F., Georgiev, Y., Herzog, G., Galvin, P., and Petkov, N. 2012. 'FIB patterning of stainless steel for the development of nano-structured stent surfaces for cardiovascular applications', *Journal of Physics: Conference Series*, 371: 012065.
Schned, A.R., Wheeler, K.J., Hodorowski, C.A., Heaney, J.A., Ernstoff, M.S., Amdur, R. J., and Harris, R.D. 1996. 'Tissue-shrinkage correction factor in the calculation of prostate cancer volume', *The American journal of surgical pathology*, 20: 1501-06.
Schroettner, H., Schmied, M., and Scherer, S. 2006. 'Comparison of 3D surface reconstruction data from certified depth standards obtained by SEM and an infinite focus measurement machine (IFM)', *Microchimica Acta*, 155: 279-84.
Sigwart, U., Puel, J., Mirkovitch, V., Joffre, F., and Kappenberger, L. 1987. 'Intravascular stents to prevent occlusion and re-stenosis after transluminal angioplasty', *New England Journal of Medicine*, 316: 701-06.
Song, H.Y., Kim, J.H., and Yoon, C.J. 2013. 'History of self-expandable metal and self-expandable plastic stent development.' in, *Self-Expandable Stents in the Gastrointestinal Tract*.
Starr, C., and Taggart, R. 1989. *Biology: the unity and diversity of life* (Wadsworth).
Stary, H.C., Chandler, A.B., Glagov, S., Guyton, J.R., Insull, W., Rosenfeld, M.E., Schaffer, S.A., Schwartz, C.J., Wagner, W.D., and Wissler, R.W. 1994. 'A definition of initial, fatty streak, and intermediate lesions of atherosclerosis. A report from the committee on vascular lesions of the council on arteriosclerosis, American Heart Association', *Circulation*, 89: 2462-78.
Stonebridge, P.A., and Brophy, C.M. 1991. 'Spiral laminar flow in arteries?', *The Lancet*, 338: 1360-61.
Sung, H-W., Chang, Y., Chiu, C-T., Chen, C-N., and Liang, H-C. 1999. 'Crosslinking characteristics and mechanical properties of a bovine pericardium fixed with a naturally occurring crosslinking agent', *Journal of Biomedical Materials Research Part A*, 47: 116-26.
Tada, N., Virmani, R., Grant, G., Bartlett, L., Black, A., Clavijo, C., Christians, U., Betts, R., Savage, D., and Su, S-H. 2010. 'Polymer-free biolimus a9-coated stent demonstrates more sustained intimal inhibition, improved healing, and reduced inflammation compared with a polymer-coated sirolimus-eluting cypher stent in a porcine model', *Circulation: Cardiovascular Interventions*, 3: 174-83.
Taniguchi, R., Hosaka, A., Miyahara, T., Hoshina, K., Okamoto, H., Shigematsu, K., Miyata, T., Sugiura, R., Yokobori, A.T. Jr. , and Watanabe, T. 2015. 'Viscoelastic deterioration of the carotid artery vascular wall is a possible predictor of coronary artery disease', *Journal of Atherosclerosis and Thrombosis*, 22: 415-23.
Tholt, B., Miranda-Júnior, W.G., Prioli, R., Thompson, J., and Oda, M. 2006. 'Surface roughness in ceramics with different finishing techniques using atomic force microscope and profilometer', *Operative Dentistry*, 31: 442-49.

Timashev, P.S., Kotova, S.L., Belkova, G.V., Gubar'kova, E.V., Timofeeva, L.B., Gladkova, N.D., and Solovieva, A.B. 2016. 'Atomic force microscopy study of atherosclerosis progression in arterial walls', *Microscopy and Microanalysis*, 22: 311-25.

Timmins, L.H., Wu, Q., Yeh, A.T., Moore, J.E., and Greenwald, S.E. 2010. 'Structural inhomogeneity and fiber orientation in the inner arterial media', *American Journal of Physiology - Heart and Circulatory Physiology*, 298: H1537-H45.

Townsend, N., Bhatnagar, P., Wilkins, E., Wickramasinghe, K., and Rayner, M. 2014. 'Cardiovascular disease statistics, 2014'

Townsend, N., Bhatnagar, P., Wilkins, E., Wickramasinghe, K., and Rayner, M. 2015. 'Cardiovascular disease statistics, 2015'

Turgeon, M.L. 2005. *Clinical hematology: theory and procedures* (Lippincott Williams & Wilkins).

Uchida, Y., Uchida, Y., Matsuyama, A., Koga, A., Maezawa, Y., Maezawa, Y., and Hiruta, N. 2011. 'Functional medial thickening and folding of the internal elastic lamina in coronary spasm', *American Journal of Physiology - Heart and Circulatory Physiology*, 300: H423-H30.

University of Rochester Medical Center. 2017. 'What is plasma?'. https://www.urmc.rochester.edu/encyclopedia/content.aspx?ContentTypeID=160&ContentID=37.

Valdez-Jasso, D., Haider, M., Banks, H.T., Santana, D.B., Germán, Y.Z., Armentano, R.L., and Olufsen, M.S. 2009. 'Analysis of viscoelastic wall properties in ovine arteries', *IEEE Transactions on Biomedical Engineering*, 56: 210-19.

Van Andel, C.J., Pistecky, P.V., and Borst, C. 2003. 'Mechanical properties of porcine and human arteries: Implications for coronary anastomotic connectors', *Annals of Thoracic Surgery*, 76: 58-64.

Vanderbilt University. 2007. 'Fractals and the fractal dimension', Accessed September 2017. http://www.vanderbilt.edu/AnS/psychology/cogsci/chaos/workshop/Fractals.html.

Van Vré, E.A., Bosmans, J.M., Van Brussel, I., Maris, M., De Meyer, G.R.Y., Van Schil, P.E., Vrints, C.J., and Bult, H. 2011. 'Immunohistochemical characterisation of dendritic cells in human atherosclerotic lesions: possible pitfalls', *Pathology - Journal of the RCPA*, 43: 239-47.

Vartanian, K.B., Kirkpatrick, S.J., Hanson, S.R., and Hinds, M.T. 2008. 'Endothelial cell cytoskeletal alignment independent of fluid shear stress on micropatterned surfaces', *Biochemical and Biophysical Research Communications*, 371: 787-92.

Vartanian, K.B., Kirkpatrick, S.J., McCarty, O.J., Vu, T.Q., Hanson, S.R., and Hinds, M.T. 2009. 'Distinct extracellular matrix microenvironments of progenitor and carotid endothelial cells', *Journal of Biomedical Materials Research Part A*, 91: 528-39.

Veress, A.I., Vince, D.G., Anderson, P.M., Cornhill, J.F., Herderick, E.E., Klingensmith, J.D., Kuban, B.D., Greenberg, N.L., and Thomas, J.D. 2000. 'Vascular mechanics of the coronary artery', *Zeitschrift für Kardiologie*, 89: S092-S100.

Vesely, I. 1996. 'A mechanism for the decrease in stiffness of bioprosthetic heart valve tissues after cross-linking', *ASAIO journal*, 42: 993-99.

Vignesh, S.N., Bhuminathan, M., and Santhosh, S. 2015. 'Comparative evaluation of the three different surface treatments – conventional, laser and nano technology methods in enhancing the surface characteristics of commercially pure titanium discs and their effects on cell adhesion: an in vitro study', *Journal of Pharmacy & Bioallied Sciences*, 7: S87-S91.

Vladkova, T.G. 2013. *Surface engineering of polymeric biomaterials* (Smithers Rapra).

Wang, C., Garcia, M., Lu, X., Lanir, Y., and Kassab, G. S. 2006. 'Three-dimensional mechanical properties of porcine coronary arteries: A validated two-layer model', *American Journal of Physiology: Heart and Circulatory Physiology*, 291: H1200-H09.

Wang, V.Y., Hussan, J.R., Yousefi, H., Bradley, C.P., Hunter, P.J., and Nash, M.P. 2017. 'Modelling cardiac tissue growth and remodelling', *Journal of Elasticity*: 1-23.

Wang, Z., Lakes, R.S., Golob, M., Eickhoff, J.C., and Chesler, N.C. 2013. 'Changes in large pulmonary arterial viscoelasticity in chronic pulmonary hypertension', *PloS one*, 8: e78569.
Wex, C., Stoll, A., Fröhlich, M., Arndt, S., and Lippert, H. 2014. 'Mechanics of fresh, frozen-thawed and heated porcine liver tissue', *International Journal of Hyperthermia*, 30: 271-83.
Wilcox, A.G., Buchan, K.G., and Espino, D.M. 2014. 'Frequency and diameter dependent viscoelastic properties of mitral valve chordae tendineae', *Journal of the Mechanical Behavior of Biomedical Materials*, 30: 186-95.
Wong, K., Mazumdar, J., Pincombe, B., Worthley, S.G., Sanders, P., and Abbott, D. 2006. 'Theoretical modeling of micro-scale biological phenomena in human coronary arteries', *Medical and Biological Engineering and Computing*, 44: 971-82.
World Health Organisation. 2017. 'Cardiovascular diseases (CVDs)'. http://www.who.int/mediacentre/factsheets/fs317/en/.
Wright, K.C., Wallace, S., Charnsangavej, C., Carrasco, C.H., and Gianturco, C. 1985. 'Percutaneous endovascular stents: an experimental evaluation', *Radiology*, 156: 69-72.
Xu, J., Zhu, P., Morris, M.D., and Ramamoorthy, A. 2011. 'Solid-state NMR spectroscopy provides atomic-level insights into the dehydration of cartilage', *The Journal of Physical Chemistry B*, 115: 9948.
Yang, C., Bach, R.G., Zheng, J., Naqa, I.E., Woodard, P.K., Teng, Z., Billiar, K.L., and Tang, D. 2009. 'In vivo IVUS-based 3D fluid–structure interaction models with cyclic bending and anisotropic vessel properties for human atherosclerotic coronary plaque mechanical analysis', *IEEE Transactions on Biomedical Engineering*, 56: 2420-28.
Yeh, H-I., Lu, S-K., Tian, T-Y., Hong, R-C., Lee, W-H., and Tsai, C-H. 2006. 'Comparison of endothelial cells grown on different stent materials', *Journal of Biomedical Materials Research Part A*, 76: 835-41.
Ylä-Herttuala, S., Nikkari, T., Hirvonen, J., Laaksonen, H., Möttönen, M., Pesonen, E., Raekallio, J., and Akerblom, H.K. 1986. 'Biochemical composition of coronary arteries in Finnish children', *Arteriosclerosis, Thrombosis, and Vascular Biology*, 6: 230-36.
Yuan, G., Pan, Y., Li, H., and Wang, J. 2016. 'Ultrastructure features of coronary artery endothelium in bactrian camel (camelus bactrianus)', *International Journal of Morphology*, 34: 280-84.
Zhang, G. 2005. 'Evaluating the viscoelastic properties of biological tissues in a new way', *Journal of Musculoskeletal Neuronal Interactions*, 5: 85-90.
Zhao, L., Thambyah, A., and Broom, N.D. 2014. 'A multi-scale structural study of the porcine anterior cruciate ligament tibial enthesis', *Journal of anatomy*, 224: 624-33.
Zhao, T., Li, Y., Xia, Y., Venkatraman, S.S., Xiang, Y., and Zhao, X. 2013. 'Formation of a nano-pattering NiTi surface with Ni-depleted superficial layer to promote corrosion resistance and endothelial cell-material interaction', *Journal of Materials Science: Materials in Medicine*, 24: 105-14.
Zhu, J., Liu, H., Cui, H., Tang, Z., Song, C., and Zhang, R. 2017. 'Safety and efficacy of a novel abluminal groove-filled biodegradable polymer sirolimus-eluting stent', *Journal of Materials Science: Materials in Medicine*, 28.